Spatial and temporal metrology of intense attosecond pulses

Coudert-Alteirac, Helene

2018

Document Version:
Publisher's PDF, also known as Version of record

Spatial and temporal metrology of intense attosecond pulses

by Hélène Coudert-Alteirac

LUND
UNIVERSITY

Thesis for the degree of Doctor of Philosophy in Engineering
Thesis advisors: Prof. Anne L'Huillier, Dr. Per Johnsson, Dr. Cord Arnold
Faculty opponent: Dr. Amelle Zaïr

To be presented, with the permission of the Faculty of Engineering of Lund University, for public criticism in the Rydberg Hall at the Department of Physics on Friday, the 28th of September 2018 at 13:00.

Organization
LUND UNIVERSITY

Department of Physics
Box 118
SE–221 00 LUND
Sweden

Document name
DOCTORAL DISSERTATION

Date of disputation
2018-09-28

Sponsoring organization

Author(s)
Hélène Coudert-Alteirac

Title and subtitle
Spatial and temporal metrology of intense attosecond pulses

Abstract
Attosecond pulses are short enough to capture the electronic dynamics in atoms and molecules. The work presented in this thesis deals with the generation and optimization of attosecond extreme-ultraviolet (XUV) pulses. The goal is to progress towards the realization of time-resolved nonlinear experiments at the intense XUV beamline of the Lund High-Power Laser Facility.

The XUV flux was optimized using a loose focusing geometry. This led to a formalization of scaling laws for high-order harmonic generation (HHG) and more generally for nonlinear optics in gases, e.g., filamentation. A high intensity on target was achieved by focusing the high XUV flux using a pair of toroidal mirrors in a Wolter-like configuration.

Spatial properties of the high-order harmonics were studied in details. Wavefront measurements of the harmonics were performed, both in the far field and after the refocusing optics, as well as spectrally resolved measurements. The origin of XUV aberrations is discussed, and the variation of the harmonic divergence depending on the generation position relative to the fundamental focus is studied.

The intense XUV beamline and its first nonlinear experiments are presented. An interferometer to split-and-delay the beam was developed. Tests were performed, showing the capacity to provide attosecond resolution for time-resolved experiments in the beamline.

The high XUV intensity on target combined with the attosecond interferometer opens the door to perform XUV-pump XUV-probe experiments.

Key words
Ultrafast Optics, High-order Harmonic Generation, Filamentation, Attosecond, Femtosecond, Extreme Ultraviolet, Wavefront Measurement, Optical Metrology, XUV Optics, Interferometry, Pump-probe

Classification system and/or index terms (if any)

Supplementary bibliographical information

Language
English

ISSN and key title

ISBN
978-91-7753-784-7 (print)
978-91-7753-785-4 (pdf)

Recipient's notes

Number of pages
139

Price

Security classification

Spatial and temporal metrology of intense attosecond pulses

by Hélène Coudert-Alteirac

LUND
UNIVERSITY

A doctoral thesis at a university in Sweden takes either the form of a single, cohesive research study (monograph) or a summary of research papers (compilation thesis), which the doctoral student has written alone or together with one or several other author(s).

In the latter case the thesis consists of two parts. An introductory text puts the research work into context and summarizes the main points of the papers. Then, the research publications themselves are reproduced, together with a description of the individual contributions of the authors. The research papers may either have been already published or are manuscripts at various stages (in press, submitted, or in draft).

Cover illustration front: Divergence of high-order harmonics in the far field as a function of the generation position. (Adapted from Paper VI. Credit: Jan Vogelsang).

Cover illustration back: The split-and-delay unit.

Funding information: The thesis work was financially supported by the European Research Council (PALP grant).

Faculty of Engineering, Department of Physics

ISBN: 978-91-7753-784-7 (print)
ISBN: 978-91-7753-785-4 (pdf)
ISSN: 0281-2762

Printed in Sweden by Media-Tryck, Lund University, Lund 2018

Då, när det är värst och inget hjälper,
Brister som i jubel trädets knoppar.
Då, när ingen rädsla längre håller,
faller i ett glitter kvistens droppar
glömmer att de skrämdes av det nya
glömmer att de ängslades för färden -
känner en sekund sin största trygghet,
vilar i den tillit
som skapar världen.

Karin Boye

Abstract

Attosecond pulses are short enough to capture the electronic dynamics in atoms and molecules. The work presented in this thesis deals with the generation and optimization of attosecond extreme-ultraviolet (XUV) pulses. The goal is to progress towards the realization of time-resolved nonlinear experiments at the intense XUV beamline of the Lund High-Power Laser Facility.

The XUV flux was optimized using a loose focusing geometry. This led to a formalization of scaling laws for high-order harmonic generation (HHG) and more generally for nonlinear optics in gases, e.g., filamentation. A high intensity on target was achieved by focusing the high XUV flux using a pair of toroidal mirrors in a Wolter-like configuration.

Spatial properties of the high-order harmonics were studied in details. Wavefront measurements of the harmonics were performed, both in the far field and after the refocusing optics, as well as spectrally resolved measurements. The origin of XUV aberrations is discussed, and the variation of the harmonic divergence depending on the generation position relative to the fundamental focus is studied.

The intense XUV beamline and its first nonlinear experiments are presented. An interferometer to split-and-delay the beam was developed. Tests were performed, showing the capacity to provide attosecond resolution for time-resolved experiments in the beamline.

The high XUV intensity on target combined with the attosecond interferometer opens the door to perform XUV-pump XUV-probe experiments.

Contents

Part I: Summary i
Abstract . . . i
Popular Scientific Summary . . . v
Populärvetenskaplig sammanfattning . . . ix
Résumé de vulgarisation scientifique . . . xiii
List of publications . . . xvii
Abbreviations . . . xix

Introduction 1
1 XUV-pump XUV-probe experiments . . . 2
2 Description of the work and thesis outline . . . 3

1 Generation of intense femtosecond and attosecond pulses 5
1 Femtosecond pulse generation . . . 6
2 High-order Harmonic Generation . . . 15
3 Intense XUV beamline . . . 22

2 Spatial metrology of high-order harmonics 29
1 Theoretical background . . . 29
2 Results . . . 42

3 Focusing high-order harmonics 47
1 Specificities of XUV optics and focusing . . . 47
2 Harmonic focusing with Wolter-like optics . . . 53

4 Temporal metrology of attosecond pulses 61
1 Principle of autocorrelation . . . 62
2 Experimental realization . . . 70

Summary and outlook 85

The author's contributions 89

Acknowledgments 91

References 95

Part II: Publications 109
Paper I: Scale-invariant nonlinear optics in gases 111
Paper II: Two-photon double ionization of neon using an intense attosecond pulse train 111
Paper III: A Versatile Velocity Map Ion-Electron Covariance Imaging Spectrometer for High-Intensity XUV Experiments 111
Paper IV: Micro-Focusing of Broadband High-Order Harmonic Radiation by a Double Toroidal Mirror 111
Paper V: Single-shot XUV wavefront measurements of high harmonics 111
Paper VI: Spatio-temporal coupling of attosecond pulses 113
Paper VII: Design and test of a broadband split-and-delay unit for attosecond XUV-XUV pump-probe experiments 113

Popular Scientific Summary

Have you ever seen a unicorn running in a meadow and been amazed by how gracefully and fast they gallop? You probably would have noticed that when they are galloping their legs are blurry, it is hard to decompose their movement. That is because the human eye cannot see that fast. The smallest time that we can discriminate is called *temporal resolution*. The temporal resolution of the human eye for distinguishing different characters is 40 ms (25 characters per second so 25 Hz) [1]. That explains why TV sets often work at 60 Hz: they project many fixed images quickly enough so that the human eye cannot resolve them independently, creating the illusion of continuous motion. With the development of photography, humans were finally able to resolve faster events than the eye could catch, and realized that a whole new world opened in front of them. Eadward Muybridge, a British photographer, started in 1878 to decompose the motion of different animals using several cameras triggered with a time lag. If he had been studying unicorns, this would be the first unicorn movie ever:

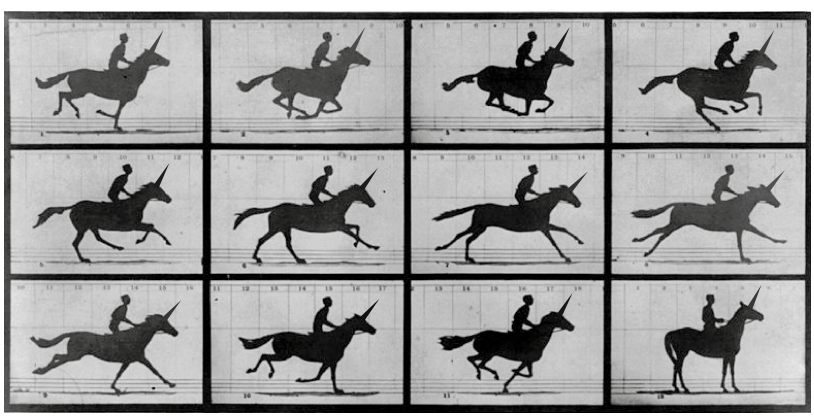

Figure 1: The Unicorn in Motion. Adapted from Eadward Muybridge's experiment, 1878. Each picture is taken by a different camera with short exposure time and triggered by the unicorn itself.

Many chemical, biological or electronic processes happen much faster than the human eye, or even a camera, can resolve. To give a feeling for the orders of these magnitudes, while the unicorn is galloping at the millisecond (10^{-3} s) timescale, operations in your computer happen in the nanosecond (10^{-9} s) timescale. Vibrations in molecules are on the order of the femtosecond (10^{-15} s), and electron dynamics in atoms of the attosecond (10^{-18} s). In comparison, the age of the universe is 0.4×10^{18} s. An attosecond is to a second what the second is to twice the age of the universe! Written in another way, 1 attosecond is 0.000 000 000 000 000 001 s.

Technology has improved dramatically over the years, but curiosity has always been the same: can we resolve faster and faster events? What is happening that we cannot see?

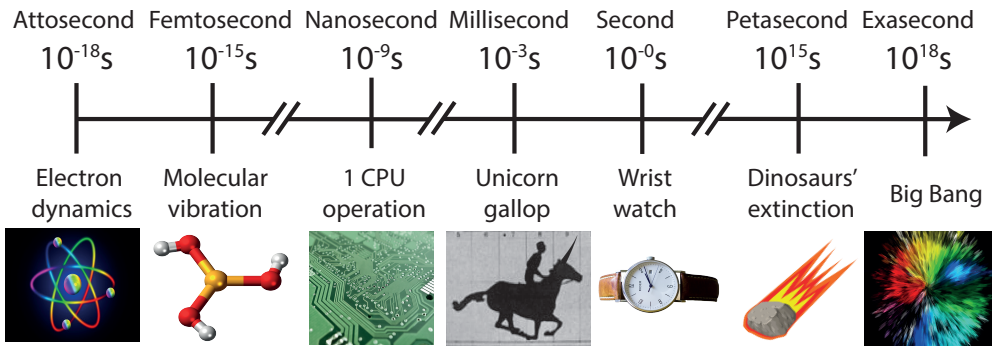

Figure 2: Timescale of diverse processes.

Science is driven both by the noble ideal of extending human knowledge and understanding of the universe and by concrete needs. Both drivers are necessary and reinforce each other. For instance, the development of the laser was not motivated by any specific application at the very beginning but ended up being a key point in the technological progress for the past 60 years. It particularly became the central tool for investigating very short temporal events. One can compare a laser pulse with the flash of a camera. The shorter the flash, the shorter the event one can record on the camera.

Generation of attosecond pulses

Laser light is a wave, and the distance that it takes for the light to oscillate one period is called the *wavelength*, or the "color". The *frequency* is the inverse of the wavelength. The laser beam is made of many waves, which are "synchronized". Their *phase* is their relative delay compared to the others. The surface where all the waves are synchronized (*in phase*) is called a *wavefront*. The property of a beam to be synchronized is called the *coherence*. This is the main difference between a laser and a light bulb: the light coming from the bulb is not coherent, the waves are independent so they propagate in different random directions and cannot interfere.

The femtosecond lasers started to be developed in the 1980s and have improved for the past decades. Now they are reliable and commercialized for many applications, and are at the origin of countless scientific discoveries, some distinguished by the Nobel prize (physics in 2005 and chemistry in 1999). The shorter a pulse the more frequencies it contains, meaning that the broader its *spectrum* is. However there is a limitation, as the pulse cannot be shorter than the light wave cycle. The cycle is 2.7 fs-long for a typical femtosecond laser at 800 nm. By increasing the frequency, so shortening the cycle, it is possible to generate even shorter pulses.

In the late 1980s, a process producing such ultrashort bursts of light was discovered. This process takes place when a short intense laser beam is focused into a gas, leading to an intensity so strong that some electrons leave their atoms. They are accelerated by the driving laser field, which gives them extra kinetic energy. A few of them are driven back to the atom and can recombine. The extra energy accumulated during their travel is transformed into energetic extreme-ultraviolet (XUV) radiation. Many atoms of the gas emit such radiation, and as the process is coherent, the radiation can form very short pulses called attosecond pulses. The spectrum of this radiation is composed of many peaks, odd multiple of the driving laser frequency. The peaks are therefore called high-order harmonics. The process is called high-order harmonic generation (HHG).

Spatial and temporal metrology of attosecond pulses

Metrology is the science of measurement. It is necessary to measure and understand a process before being able to control it. The main focus of my work has been spatial and temporal metrology of these attosecond pulses.

Firstly, I have been working on understanding the spatial properties of the HHG process and measuring the spatial profiles and wavefronts of the created beams. It is important to monitor and control the spatial quality of the beam to make sure behaves as expected and is focused on the smallest area possible in order to increase the intensity when we target atoms or molecules.

Secondly, I have worked on the development of a tool called *interferometer* for measuring ultrafast attosecond events. There are no attosecond cameras, so we have to use the attosecond pulses themselves to measure their properties, as they are the shortest event we can create nowadays. The interferometer splits the beam into two, and delays one pulse compared to the other. The aim of this tool is to target a molecule with pulses coming at different times. The first pulse is called the *pump* and initiates the process (for example, excites or ionizes the atom or molecule). The other one is called the *probe* and interacts with the system after a certain delay, providing information about how the state of the system evolved during that time. The probe pulse can be compared to the flash of a camera. By using many flashes at different times, we can obtain a "molecular movie"

Understanding the dynamics in molecules, how the charges transfer from atom to atom and how molecules break, would have important implications for chemistry and biology. For instance, if we understand how the charge transfer happens in molecules we can harvest the solar energy more efficiently, as plants do through photosynthesis. Better understanding of the processes of molecules breaking or of the charge transfer in DNA would improve medical applications such as cancer therapy. But the most exciting applications are those we cannot think about yet. I really hope that I will read this work again in 50 years and

realize how far we have come, looking back at all the breakthroughs that were triggered by attosecond research.

Populärvetenskaplig sammanfattning

Har du någonsin sett en enhörning galoppera över en äng och förundrats över hur graciöst och fort den rör sig? Du hade antagligen noterat att när de galopperar ser benen suddiga ut; det är svårt att urskilja rörelsen. Det beror på att det mänskliga ögat inte kan se så snabba rörelser. Den kortast urskiljbara tiden kallas den *temporala upplösningen*. Det mänskliga ögats temporala upplösning för att urskilja olika symboler är 40 ms (25 symboler per sekund så 25 Hz) [1]. Detta förklarar varför TV-apparater ofta drivs i 60 Hz: de projicerar många stillbilder tillräckligt snabbt för att det mänskliga ögat inte ska kunna urskilja dem som stillbilder, vilket skapar illusionen av en kontinuerlig rörelse. Tack vare den fotografiska utvecklingen kunde människan slutligen upplösa händelser snabbare än vad ögat kan fånga, varav de insåg att en helt ny värld öppnade sig framför dem. Eadward Muybridge, en brittisk fotograf, började 1878 att bryta ner olika djurs rörelsemönster genom att använda flera kameror som utlöstes med en viss tidsförskjutning. Om han hade studerat enhörningar så hade detta varit historiens första enhörningsvideo:

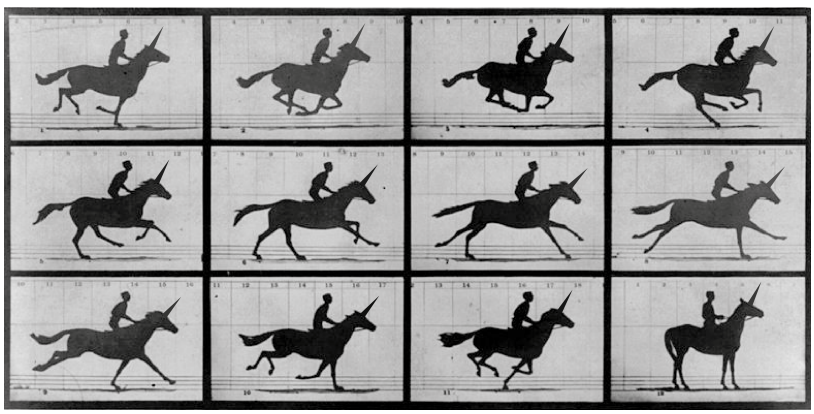

Figur 3: Enhörningen i rörelse. Bearbetning av Eadward Muybridges experiment, 1878. Var och en av bilderna är tagen med en egen, separat kamera med kort exponeringstid och utlöst av enhörningen själv.

Många kemiska, biologiska eller elektroniska processer händer mycket fortare än vad det mänskliga ögat kan uppfatta, eller ens vad en kamera kan upplösa. För att illustrera magnituderna, så är enhörningens rörelser på millisekundstidsskalan (10^{-3} s), medan operationer som sker i din dator utförs på nanosekundstidsskalan (10^{-9} s). Vibrationer i molekyler sker på några femtosekunder (10^{-15} s) och elektrondynamik i atomer är i attosekunder (10^{-18} s). I jämförelse så är universums ålder 0.4×10^{18} s. Jämförelsen av en attosekund i förhållande till en sekund är som att jämföra en sekund med två gånger universums ålder! Skrivet på ett annat sätt är 1 attosekund 0.000 000 000 000 000 001 s.

Den tekniska utvecklingen har varit dramatisk de senaste åren, men nyfikenheten har alltid varit densamma: kan vi upplösa ännu snabbare händelser? Vad pågår som vi inte kan se?

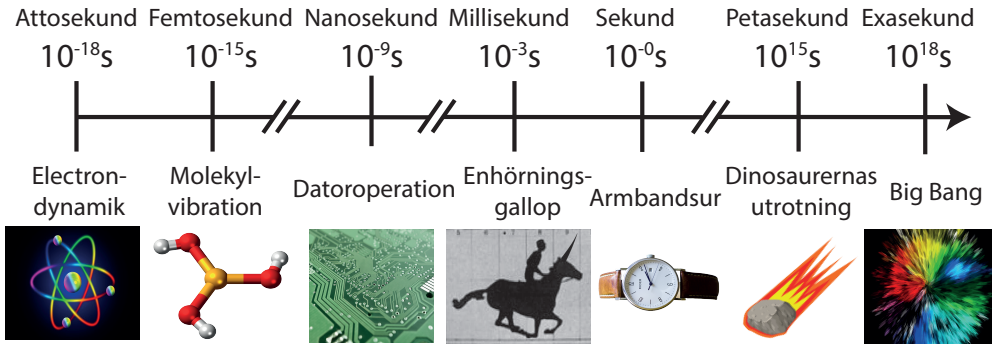

Figur 4: Tidsskalor för olika processer.

Vetenskapen drivs både av ett ädelt ideal att utvidga det mänskliga vetandet och att förstå universum, men även av konkreta behov. Båda dessa faktorer är nödvändiga och de förstärker varandra. Till exempel var utvecklingen av lasern från allra första början inte driven av någon särskild tillämpning, men den har sedan dess spelat en nyckelroll i den tekniska utvecklingen de senaste 60 åren. I synnerhet blev den ett centralt verktyg för att undersöka väldigt korta händelser i tiden. Man kan jämföra en laserpuls med en kamerablixt. Ju kortare blixten är, desto kortare händelse kan man fånga med kameran.

Generationer av attosekundpulser Det avstånd ljuset behöver för att oscillera en period kallas *våglängd*, eller "färgen". *Frekvensen* är inversen av våglängden. Laserstrålen är gjord av många vågor, som är "synkroniserade". Den relativa fördröjningen för en viss våg jämfört med de andra vågorna kallas för *fas*. Ytan där alla vågorna är synkroniserade (*i fas*) heter *vågfront*. Egenskapen hos en stråle som ska synkroniseras kallas *koherens*. Det här är den största skillnaden mellan en laser och en glödlampa: ljuset som kommer från glödlampan är inte sammanhängande, vågorna är oberoende så att de sprids i olika slumpmässiga riktningar och kan inte interferera med varandra.

Femtosekundlasrar började utvecklas på 1980-talet och har ständigt förbättrats under årtionden. Numera är de pålitliga och kommersiellt tillgängliga inom många tillämpningsområden, och de ligger till grund för otaliga vetenskapliga upptäckter, liksom Nobelpriset i fysik 2005 och i kemi 1999. Ju kortare en puls, desto mer frekvenser innehåller den, vilket betyder att ju bredare dess *spektrum* är. Det finns emellertid en begränsning, eftersom pulsen inte kan vara kortare än ljusvågscykeln. Cykeln är 2.7 fs lång för en typisk femtosekundlaser vid 800 nm. Genom att öka frekvensen, så att förkorta cykeln, är det möjligt att generera ännu kortare pulser.

I slutet av 1980-talet upptäcktes en process som producerar sådana ultrakorta pulser av ljus. Denna process kan ske när en kort, intensiv laserstråle fokuseras i en gas, vilket leder

till en så pass stark intensitet att vissa elektroner lämnar sina atomer. De accelereras av det drivande laserfältet, vilket ger dem extra rörelseenergi. Ett par av dem drivs tillbaka till atomen och kan rekombineras. Den extra energi som ackumulerats under deras resa omvandlas till energirik extrem ultraviolett strålning. Många atomer i gasen avger strålning, och eftersom processen är koherent, kan strålningen formera väldigt korta pulser som kallas attosekundpulser. Spektrumet för denna strålning är sammansatt av många toppar vid udda multiplar av drivlaserfrekvensen. Topparna kallas därför höga övertoner. Processen kallas *hög övertonsgenerering* (HHG efter engelskans high-order harmonic generation).

Tid- och rums-upplöst metrologi av attosekundpulser Metrologi, eller mätteknik, är vetenskapen om mätning. Det är nödvändigt att mäta och förstå en process innan man kan kontrollera den. Huvudsfokuset för mitt arbete har varit tid- och rums-upplöst metrologi av dessa ovannämnda attosekundpulser.

Dels har jag arbetat på att förstå HHG-processens rumsliga egenskaper samt att mäta de skapade strålarnas rumsliga profiler och vågfronter. Det är viktigt att övervaka och kontrollera strålens rumsliga kvalitet för att försäkra sig om att den kommer att bete sig som förväntat samt att den är fokuserad på minsta möjliga yta, för att öka intensiteten när vi siktar på atomer eller molekyler.

Parallellt har jag också arbetat med att utveckla ett redskap, kallat en interferometer, för att mäta ultrasnabba händelser på attosekundtidsskalan. Det finns inga attosekundkameror, så vi måste använda attosekundpulserna själva för att mäta deras egenskaper, eftersom de är de kortaste händelserna vi kan skapa där vi befinner oss idag. Interferometern delar på strålen och fördröjer den ena halvan i förhållande till den andra. Syftet med detta redskap är att träffa en molekyl med pulser som kommer på olika tider. Den första pulsen kallas för *pump* och initierar processen (till exempel exciterar eller joniserar atomen eller molekylen). Den andra kallas för *probe* och interagerar med systemet efter en viss fördröjning och därför ger information om hur systemets tillstånd förändrats efter denna tid. Probpulsen kan jämföras med blixten i en kamera. Genom att använda många blixtar vid olika tidpunkter kan vi få fram en "molekylär film".

Att kunna förstå molekylers dynamik, hur laddningar förflyttas från en atom till en annan och hur molekyler går sönder, skulle ha stor påverkan inom kemi och biologi. Om vi till exempel kan förstå hur laddningsförflyttningen sker i molekyler skulle vi kunna utnyttja solenergi mer effektivt, som växter gör genom fotosyntesen. En bättre förståelse av processerna som är involverade då molekyler går sönder, eller vid laddningsförflyttningar i DNA, skulle kunna förbättra medicinska tillämpningar såsom cancerterapi. Men de mest spännande tillämpningarna är de vi ännu inte kan tänka oss. Jag hoppas verkligen att jag kommer att läsa detta arbete igen om 50 år och inse hur långt vi har kommit, på grund av de genombrott som skett till följd av attosekundforskningen.

Résumé de vulgarisation scientifique

Avez-vous déjà vu une licorne galoper dans une prairie, avez-vous déjà été émerveillé.e par la rapidité de leur gracieux galop ? Vous avez alors probablement remarqué que quand elles galopent, leur pattes sont floues, il devient difficile de dinstinguer leur mouvement. L'œil humain n'est pas assez rapide pour cela. Le plus petit laps de temps qu'il peut percevoir s'appelle la *résolution temporelle*. La résolution temporelle de l'œil humain pour différencier des caractères différents est 40 ms (25 caractères par seconde donc 25 Hz) [1]. C'est pour cela que les télévisions fonctionnent à 60 Hz : elles projettent des images fixes assez rapidement pour que l'œil humain ne puisse pas les distinguer, ce qui donne l'illusion d'un mouvement continu. Avec le développement de la photographie, les humains ont enfin pu décomposer des mouvements plus rapides que ce que l'œil peut distinguer. Un monde nouveau s'ouvrait à eux ! Un photographe britannique, Eadward Muybridge, a commencé en 1878 à décomposer le mouvement de différents animaux en utilisant plusieurs appareils photo déclenchés à tour de rôle par l'animal qui court. Si il avait étudié les licornes, voici ce qui aurait été le premier film de licornes de tous les temps :

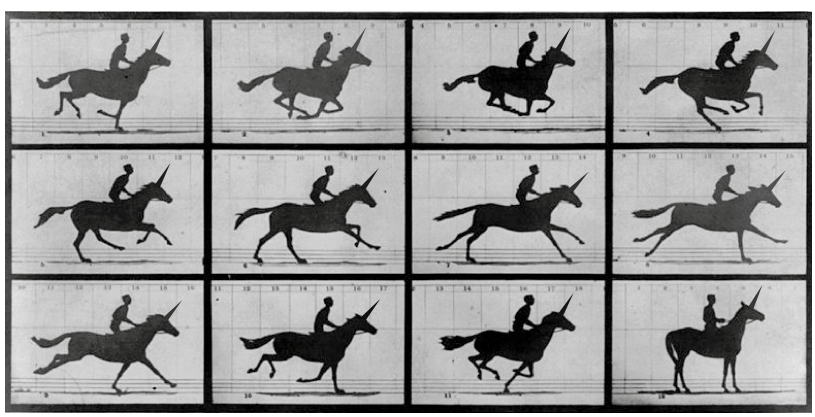

Figure 5 : La Licorne en Mouvement. Adaptation de l'expérience d'Eadward Muybride, 1878. Chaque image est prise par un appareil avec un court temps d'exposition, déclenché par la course de la licorne.

De nombreux processus chimiques, biologiques ou electroniques sont beaucoup plus rapides que ce que l'oeil humain ou une camera peut percevoir. Pour donner un ordre d'idée, alors que le mouvement de la licorne a lieu à l'échelle de la milliseconde (10^{-3} s), les opérations dans votre ordinateur sont de l'ordre de la nanoseconde (10^{-9} s). Les vibrations des molécules se comptent en femtosecondes (10^{-15} s), et les dynamiques des électrons en attosecondes (10^{-18} s). En comparaison, l'âge de l'univers est de 0.4×10^{18} s. Une attoseconde est donc à la seconde ce que la seconde est à l'âge de l'univers. Écrit autrement, 1 attoseconde est 0.000 000 000 000 001 s... vertigineux !

La technologie a énormément évolué au fil des années, mais la curiosité est restée inchan-

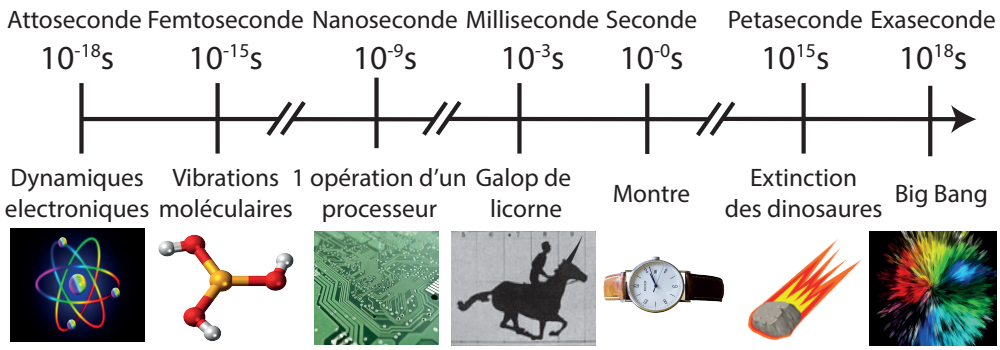

Figure 6 : Différentes échelles de temps.

gée : peut-on résoudre des événements toujours plus rapides ? Y-a-t-il encore des choses que nous ne pouvons pas percevoir ? La science est motivée par le noble idéal d'étendre la connaissance humaine et notre compréhension de l'univers, mais aussi par des besoins concrets. Ces deux motivations se renforcent mutuellement. Par exemple, l'invention du laser n'était pas au départ motivée par une quelconque application mais est devenue une clé du progrès technologique depuis 60 ans. Il est notamment devenu l'outil central pour étudier des événements ultra-rapides. On peut comparer une impulsion laser avec le flash d'une caméra, plus il est court plus l'événement que l'on peut enregistrer est court.

Génération d'impulsions attosecondes

La lumière laser est une onde, et la distance que l'onde met pour osciller d'une période s'appelle la *longueur d'onde*, ou la "couleur". La *fréquence* est l'inverse de la longueur d'onde. Un faisceau laser est constitué de nombreuses ondes, qui sont "synchronisées". Leur *phase* est leur retard relatif par rapport aux autres. La surface où les ondes sont synchronisées (*en phase*) s'appelle le *front d'onde*. La capacité d'un faisceau à être synchronisé s'appelle la *cohérence*. C'est la principale différence entre un laser et une ampoule : la lumière venant de l'ampoule n'est pas cohérente, les ondes sont indépendantes, se propagent dans des directions différentes et ne peuvent pas interférer.

Le développement des lasers femtosecondes a commencé dans les années 80, et ils ont été constamment améliorés depuis. De nos jours, ces lasers sont fiables et disponibles dans le commerce pour de nombreuses applications, et sont à l'origine d'innombrables découvertes scientifiques, certaines même récompensées par un prix Nobel (physique en 2005 et chimie en 1999). Plus une impulsion est courte plus elle contient de fréquences, ce qui veut dire que le *spectre* est plus large. Cependant, la limite est que l'impulsion ne peut pas être plus courte que le cycle de l'onde lumineuse. Ce cycle dure 2.7 fs pour un laser femtoseconde à 800 nm. En augmentant la fréquence, donc en allant vers un cycle plus court, il est possible

de générer des impulsions encore plus courtes.

A la fin des années 80, un processus produisant des impulsions aussi courtes a été découvert. Ce processus peut se déclencher quand un faisceau laser intense est focalisé dans un gaz, ce qui amène une intensité tellement forte que certains électrons quittent leurs atomes. Ils sont accélérés par le champ laser, ce qui leur donne de l'énergie cinétique. Quelques uns sont ramenés vers l'atome et peuvent se recombiner. L'énergie accumulée pendant leur parcours est transformée en radiation extrême-ultraviolette (XUV) énergétique. Beaucoup d'atomes dans le gaz émettent une telle radiation, et comme le processus est cohérent, la radiation peut former des impulsions très courtes appelées impulsions attosecondes. Le spectre de cette radiation se compose de nombreux pics, multiples impairs de la fréquence du laser. Ces pics s'appellent donc des harmoniques d'ordre élevé. Ce processus s'appelle génération d'harmoniques d'ordre élevé (HHG en anglais).

Métrologie spatiale et temporelle des impulsions attosecondes

La métrologie est la science de la mesure. Il est nécessaire de mesurer et de comprendre un processus avant de pouvoir le contrôler. Mon travail a été centré sur la métrologie spatiale et temporelle de ces impulsions attosecondes.

Premièrement, j'ai travaillé sur la compréhension des propriétés spatiales de la HHG, et ai mesuré les profils spatiaux et les fronts d'onde des faisceaux générées. Il est important de surveiller et contrôler la qualité spatiale des faisceaux pour pouvoir les utiliser, et notamment pour qu'ils puissent se focaliser sur la plus petite surface possible, pour augmenter l'intensité quand on cible des atomes et molécules.

Deuxièmement, j'ai travaillé sur le développement d'un outil appelé *interféromètre*, pour mesurer des événements attosecondes ultra-rapides. Il n'y a pas de camera attoseconde, donc on doit utiliser les impulsions attosecondes elles-mêmes vu que c'est la chose la plus rapide que l'on puisse créer de nos jours. L'interféromètre sépare le faisceau en deux, et retarde une impulsion par rapport a l'autre . Le but est de cibler une molécule avec des impulsions à différents instants. La première impulsion s'appelle la *pompe*, elle démarre un processus (par exemple excite ou ionise l'atome ou la molécule). L'autre s'appelle la *sonde*, et interagit avec le système après un certain temps, ce qui donne des informations sur l'évolution de l'état du système pendant ce temps là. L'impulsion sonde peut être comparée au flash d'une camera. En utilisent de nombreux flashs à des instants différents, on peut obtenir un "film moléculaire".

Comprendre les dynamiques dans les molécules, comment les charges transfèrent d'atome en atome et comment les molécules se brisent, pourrait avoir des conséquences importantes pour la chimie ou la biologie. Par exemple, si on pouvait comprendre comment le transfert

de charges se déroule, on pourrait récolter l'énergie solaire plus efficacement, comme les plantes le font par photosynthèse. Une meilleure compréhension de comment les molécules se brisent ou du transfert de charges dans l'ADN améliorerait les applications médicales comme le traitement du cancer. Mais les débouchés les plus intéressants sont ceux auxquels on ne pense pas encore. J'espère pouvoir lire ce travail dans 50 ans et constater le chemin parcouru en voyant toutes les découvertes déclenchées par la recherche attoseconde.

List of publications

This thesis is based on the following publications, referred to by their Roman numerals :

I **Scale-invariant nonlinear optics in gases**

C. M. Heyl, H. Coudert-Alteirac, M. Miranda, M. Louisy, K. Kovacs, V. Tosa, E. Balogh, K. Varjú, A. L'Huillier, A. Couairon, and C. L. Arnold
Optica, 3, 75-81 (2016)

II **Two-photon double ionization of neon using an intense attosecond pulse train**

B. Manschwetus, L. Rading, F. Campi, S. Maclot, H. Coudert-Alteirac, J. Lahl, H. Wikmark, P. Rudawski, C. M. Heyl, B. Farkas, T. Mohamed, A. L'Huillier, and P. Johnsson
Phys. Rev. A, 93, 061402 (2016)

III **A Versatile Velocity Map Ion-Electron Covariance Imaging Spectrometer for High-Intensity XUV Experiments**
L. Rading, J. Lahl, S. Maclot, F. Campi, H. Coudert-Alteirac, B. Oostenrijk, J. Peschel, H. Wikmark, P. Rudawski, M. Gisselbrecht, and P. Johnsson
Appl. Sci., 8, 998 (2018)

IV **Micro-Focusing of Broadband High-Order Harmonic Radiation by a Double Toroidal Mirror**
H. Coudert-Alteirac, H. Dacasa, F. Campi, E. Kueny, B. Farkas, F. Brunner, S. Maclot, B. Manschwetus, H. Wikmark, J. Lahl, L. Rading, J. Peschel, B. Major, K. Varjú, G. Dovillaire, P. Zeitoun, P. Johnsson, A. L'Huillier, and P. Rudawski
Appl. Sci., 7, 1159 (2017)

v **Single-shot XUV wavefront measurements of high harmonics**

H. Dacasa, H. Coudert-Alteirac, C. Guo, E. Kueny, F. Campi, J. Lahl, E.Malm, J. Peschel, H. Wikmark, D. Alj, C. L. Arnold, G. Dovillaire, P. Johnsson, A. L'Huillier, S. Maclot, P. Rudawski, and P. Zeitoun
manuscript

vi **Spatio-temporal coupling of attosecond pulses**

H. Wikmark, C. Guo, J. Vogelsang, H. Coudert-Alteirac, J. Lahl, J. Peschel, P. Rudawski, H. Dacasa , S. Carlström, S. Maclot, P. Johnsson, C. L. Arnold, A. L'Huillier
manuscript

vii **Design and test of a broadband split-and-delay unit for attosecond XUV-XUV pump-probe experiments**
F. Campi*, **H. Coudert-Alteirac***, M. Miranda, L. Rading, B. Manschwetus, P. Rudawski, A. L'Huillier, and P. Johnsson;
(* Authors contributed equally)
Rev. Sci. Instrum., 87, 023106 (2016)

Abbreviations

AC	Autocorrelation
APT	Attosecond Pulse Train
AR	Anti-Reflection
CCD	Charge-Coupled Device
CEA	Commissariat à l'énergie atomique, French Laboratory
CEP	Carrier-Envelope Phase
CPA	Chirped Pulse Amplification
d-scan	Dispersion Scan
DVMIS	Double Velocity Map Imaging Spectrometer
FEL	Free Electron Laser
FORTH	Foundation for Research and Technology, Greek Laboratory
FROG	Frequency Resolved Optical Gating
FROG-CRAB	Frequency Resolved Optical Gating for Complete Reconstruction of Attosecond Bursts
FS	Fused Silica
FT	Fourier Transform
FWHM	Full Width at Half Maximum
HHG	High-order Harmonic Generation
IAC	Interferometric Autocorrelation
IAP	Intense Attosecond Pulse
IR	Infrared Radiation
LOA	Laboratoire d'Optique Appliquée, French Laboratory
LSI	Lateral Shearing Interferometer
MCP	Micro Channel Plate
OPCPA	Optical Parametric Chirped Pulse Amplification
PV	Peak-to-Valley
RABBIT	Reconstruction of Attosecond Beating By Interference of Two-photon transitions
RIKEN	Rikagaku Kenkyusho, Japonese Laboratory
RMS	Root-Mean-Square
SDU	Split-and-Delay Unit
SFA	Strong Field Approximation
SHG	Second Harmonic Generation
SPIDER	Spectral Phase Interference for Direct Electric-field Reconstruction
TDSE	Time-Dependent Schrödinger Equation
TOF	Time-Of-Flight

TPDI	Two-photon double ionization
TW	Terawatt
VUV	Vacuum-Ultraviolet
VMI	Velocity Map Imaging
VMIS	Velocity Map Imaging Spectrometer
XUV	Extreme Ultraviolet

Introduction

Curiosity has always been the main driver of science. The invention of photography and ultrafast cameras opened new perspectives and allowed for studying faster and faster events and processes. But even the most advanced detectors cannot detect events faster than a picosecond (10^{-12} s). Since the birth of the laser in 1960, the technology has improved constantly, and nowadays femtosecond (10^{-15} s) laser pulses are commercially available, triggering many discoveries. New techniques were developed to use these pulses to probe dynamics on ultrafast timescales. These techniques belong to the *pump-probe* category. In that scheme, one *pump* pulse is sent to initiate a process, for instance to excite a system, and another *probe* pulse is sent with a certain delay to record the changes in the state of the system. By reproducing the experiment with a different delay, it is possible to reconstruct the temporal evolution of the system. The 1999 Nobel Prize in chemistry was awarded for the birth of femtochemistry which uses pump-probe techniques at a femtosecond scale to study molecular dynamics, i.e. the motion of nuclei in molecules [2].

From femto-dynamics to atto-dynamics

Electron dynamics often happen on a timescale shorter than a femtosecond: the attosecond regime (10^{-18} s). In the late 1980s, a process generating attosecond pulses through high-order harmonic generation (HHG) was discovered [3, 4]. Their characterization in 2001 opened the field of attosecond science [5, 6]. High-order harmonics are remarkable because of both their temporal and their spectral properties. In the time domain, they form coherent attosecond pulses which can be used to probe ultrafast dynamics. Also, they are generated in the VUV (vacuum-ultraviolet) or XUV (extreme-ultraviolet) ranges, which are between the UV and X-ray spectral regions, and thus have higher photon energies than all other temporally coherent light sources except Free-Electron Lasers (FELs). As their photon energy is on the order of the first atomic ionization energies, absorption of one XUV photon can lead to valence-shell ionization and provides direct insight into light-matter interaction.

However, the efficiency of HHG is very low ($\sim 10^{-6}$), making access to the nonlinear

regime difficult. Additional limitations come from the weak response of the materials in the VUV and XUV spectral ranges. For these reasons, the first experiments with XUV attosecond pulses used IR femtosecond pulses as a probe, making it possible to study shorter timescale dynamics than in IR-pump IR-probe experiments and taking advantage of the high photon energy of XUV attosecond pulses. The energy of the XUV attosecond pulses is high enough to photoionize electrons in the valence shell and in the outmost inner shells. Furthermore, the broad spectrum of attosecond pulses allows for interactions with many different states at once. The IR pulse probes the dynamics that the XUV pulse initiated, or vice versa [7]. Experiments have been carried out, bringing insight into fast molecular dynamics [8–11], with, in some cases, attosecond resolution [7, 12, 13]. Photo-ionization time delays have also been extracted using cross-correlation techniques [14–19].

While the combined effects of IR and XUV pulses present very interesting features, the IR can nonetheless limit the accessible dynamics. First, the temporal resolution is affected. Second, since the IR field is generally more intense than the attosecond pulses, it might drive the dynamics instead of just probing it.

1 XUV-pump XUV-probe experiments

To overcome these limitations, it is important to develop attosecond XUV-pump attosecond XUV-probe experiments. FELs are a source of intense XUV pulses with more flux than what is possible with HHG. For that reason, many XUV-pump XUV-probe experiments were conducted with FEL light [20–22]. The temporal duration of the FEL pulses was in the order of tens of femtoseconds at best in the experiments, but there is a lot of progress presently toward shorter pulses [23, 24] and even sub-femtosecond bursts have been generated [25].

With the development of high flux HHG sources [26–29], nonlinear experiments involving several XUV attosecond pulses became possible [30–32]. The first autocorrelation with attosecond pulses [33] paved the way for XUV-pump XUV-probe experiments with attosecond pulse trains (APTs). A few XUV-pump XUV-probe experiments with APTs have been reported on nitrogen and hydrogen [34–37], yet they remain challenging.

The main goal of this work is to conduct such experiments. They require intense attosecond pulses with controlled delay between them. Three main challenges arise from this requirement.

- Due to the low conversion efficiency of the HHG process, obtaining a good XUV flux is difficult. It is possible to increase it by using a loose focusing configuration. The goal is to obtain high intensity (10^{12} W/cm^2) on target.

- Another factor is the spatial quality of the beam. In order to reach the high intensity on target, the beam has to be focused on a small focal spot. It requires good wavefront quality. There is a need for spatial metrology to study wavefront quality, focal spot size and focusing.
- The last step is to develop an interferometer able to split the attosecond beams and introduce a delay between the pump and probe pulses. Good temporal resolution and stability are essential.

A further development is to generate isolated attosecond pulses (IAPs) [6, 38–41]. The APT structure is generally several tens of femtoseconds long, so the signal is convoluted with this long envelope. Several techniques exist to generate IAPs [42, 43], the goal being to isolate one cycle of the driving field to generate a broad continuum giving rise to a short isolated pulse. In general, the shorter the driving pulse the easier it is to generate isolated pulses. Techniques such as filamentation that can broaden the IR spectrum to obtain a shorter pulse are of interest [44]. The main limitation of IAP generation is low conversion efficiency, as only one cycle is used. Scaling techniques for obtaining high HHG flux need to be combined with efficient gating techniques. Recently, 1 μJ IAPs have been reported [45].

2 Description of the work and thesis outline

The main focus of my work was to advance toward nonlinear, multiphoton, time-resolved experiments at the intense XUV beamline of the Lund High-Power Laser Facility. When I started my thesis, the XUV-XUV interferometer had just been built, but without the required stabilization scheme or software. I developed them along with alignment procedures, and focused on performing test autocorrelations. I also worked on the beamline development and conducted nonlinear experiments with intense XUV pulses. Due to my interest in ultrashort pulses, I also got involved in filamentation scaling experiments. During a wavefront measurement campaign, we gained a lot of insight into the spatial properties of harmonics. It helped us to optimize our focusing optics and the quality of the XUV pulses, as well as triggering a more fundamental discussion about how these XUV pulses acquire their aberrations.

This thesis is based on seven papers. Paper I describes the scaling of nonlinear processes, such as HHG and filamentation. Papers II and III are based on the results obtained at the intense XUV beamline with multiphoton, nonlinear ionization and the detection scheme used. Papers IV, V and VI explore spatial properties of high-harmonics. Paper IV describes optimization of focusing by wavefront metrology. In Paper V we study the impact of generation conditions and the IR beam on XUV wavefront quality. In Paper VI we investigate

the variation of harmonic divergences depending on the generation position relative to the fundamental focus. Paper VII describes the interferometer that we developed for realizing time-resolved nonlinear experiments in the intense XUV beamline.

The first chapter presents how femtosecond and attosecond pulses are generated, and how these processes can be scaled up to higher energies. The intense XUV beamline and its detectors are also described. The second chapter deals with spatial metrology of high-order harmonics, the definition of aberrations, how they are transmitted and how to measure them. The third chapter is about focusing high-order harmonics, the specific challenges of the XUV regime and the experimental realization in the intense XUV beamline. The last chapter deals with temporal metrology of attosecond pulses. The concept of autocorrelation is described as well as the design of our interferometer, and the road towards time-resolved experiments.

Chapter 1

Generation of intense femtosecond and attosecond pulses

This chapter describes the generation of ultrashort pulses, both femtosecond and attosecond, and the intense XUV beamline used in the present work.

First, we present the techniques used to generate most ultrashort laser pulses: chirp-pulsed amplification (CPA) and optical parametric chirped-pulse amplification (OPCPA). The phenomena of filamentation, when an ultrashort intense laser pulse is focused in a gas under certain conditions, is briefly described. Filamentation can be used as a post-compression technique thanks to spectral broadening in the filament, thus allowing for the generation of even shorter pulses. We introduce the scaling laws for nonlinear optical phenomena in gases, with an experimental demonstration on filamentation (Paper I).

The shortest available pulses are not lasers but attosecond pulses generated by high-order harmonic generation (HHG). We introduce the three-step model for HHG, examine the dependence of the dipole phase on intensity, discuss phase matching conditions and then extend the scaling laws to HHG.

Finally, we present the intense XUV beamline, where most of the experiments in this work have been performed. The beamline was developed for intense nonlinear experiments with atoms and molecules, such as two-photon double ionization of neon presented in Paper II. The detector presented in Paper III, which allows for simultaneous detection of ions and electrons, a double Velocity Map Imaging Spectrometer (VMIS), is also described.

1 Femtosecond pulse generation

1.1 Femtosecond lasers

The experiments presented in this work were performed with three different laser systems at the Lund High Power Laser Facility. Two of them are based on chirped-pulse amplification (CPA) from a Titanium-doped Sapphire oscillator. The CPA technique consists of stretching the pulses from the oscillator and amplifying them using the energy stored in a crystal that has been previously pumped, as illustrated in Figure 1.1 a). After amplification, the pulses are compressed again. The technique was developed in the mid 1980s and allows for generation of femtosecond lasers pulses beyond terawatt (TW) peak power. The first laser system, the most powerful one, is used for the intense XUV beamline (see Section 3) and can generate up to 1 J pulses of 40 fs at 800 nm and at 10 Hz repetition rate. The second laser, in the "attosecond laboratory", can deliver 20 fs pulses, 5 mJ at 800 nm and a 1 kHz repetition rate.

Gain narrowing in the crystal limits usable bandwidth and therefore prevents us from obtaining very short pulses. Heat management due to storage of energy in the crystal also limits the repetition rate. To overcome these limitations, a technique called Optical Parametric Chirped-Pulse Amplification (OPCPA) was developed. The concepts of stretching and recompressing the pulse are the same, but amplification is performed instead in a nonlinear crystal, as shown in Figure 1.1 b). This allows for the amplification of a large bandwidth down to single-cycle laser pulses. The energy is not stored in the crystal as in traditional amplification but transferred through the parametric process, allowing for high repetition rates. The third laser used in this work is based on this OPCPA technique. It can deliver 7 μJ, 7 fs pulses at 850 nm with a repetition rate of 200 kHz.

1.2 Nonlinear pulse propagation

Many nonlinear phenomena can arise upon propagation of an ultrashort pulse in a medium. This section introduces theoretically a few nonlinear optical phenomena taking place in the experiments performed in the present work. First we recall the equations for propagation of an electromagnetic wave in a vacuum and then in a medium, taking into account its nonlinear response at high intensity.

Obtained from the Maxwell equations, assuming linear polarization, the scalar homogeneous wave equation describing the propagation in vacuum of an electromagnetic wave described by a spectral amplitude $\hat{E}$ in the frequency domain is written as:

$$\nabla^2 \hat{E} + k^2 \hat{E} = 0 \tag{1.1}$$

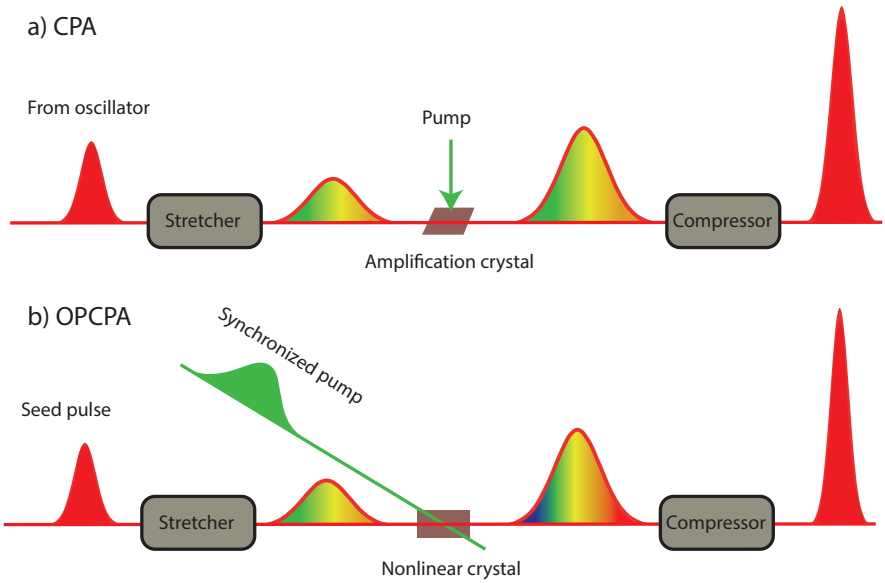

Figure 1.1: a) CPA technique: the pulse is temporally stretched, amplified in a pumped crystal, and recompressed. b) OPCPA technique: amplification takes place through a parametric process, where the energy is transfered directly from a pump pulse.

with k the wave vector equal to ω/c. Upon propagation in a dielectric medium, the field induces polarization P in the medium, which influences propagation. The propagation equation is modified to include the effect of polarization as

$$\nabla^2 \hat{E} + k^2 \hat{E} = -\mu_0 \omega^2 \hat{P} \tag{1.2}$$

with μ_0 the vacuum permeability. In linear optics, polarization $\hat{P}$ is defined as $\hat{P} = \epsilon_0 \chi \hat{E}$ with χ the electric susceptibility. χ is related to the refractive index n by $n^2 = 1+\chi = \epsilon/\epsilon_0$, with ϵ the relative permittivity of the medium and ϵ_0 the vacuum permittivity. μ_0 and ϵ_0 are linked as $c^2 = 1/(\epsilon_0 \mu_0)$. k becomes equal to $n\omega/c$.

At high field intensities, the medium response becomes nonlinear. The polarization becomes a nonlinear function of the electric field $\hat{E}$:

$$\hat{P} = \underbrace{\epsilon_0 \chi^{(1)} \hat{E}}_{\text{linear term}} + \underbrace{\epsilon_0 \chi^{(2)} \hat{E}^2 + \epsilon_0 \chi^{(3)} \hat{E}^3}_{\text{nonlinear terms}} + \ldots \tag{1.3}$$

The term $\chi^{(2)}$ gives rise to second harmonic generation (SHG), sum and difference frequency generation, parametric amplification, etc. Similarly, the $\chi^{(3)}$ term is responsible for third order harmonic generation and four-wave mixing.

In an isotropic medium, $\chi^{(2)} = 0$ so $\chi^{(3)}$ becomes dominant. The index of refraction n becomes intensity-dependent:

$$n = n_0 + n_2 I \tag{1.4}$$

where n_0 is the linear refractive index. The nonlinear refractive index n_2 is related to $\chi^{(3)}$ by the equation $n_2 = 3\chi^{(3)}/4\epsilon_0 c n_0^2$. The intensity dependence of the refractive index is called the Kerr effect and leads to the following:

- Spectrally, the frequency of the pulse can experience an intensity-dependent shift during propagation, known as *self-phase modulation*. New frequencies are created, which broadens the pulse spectrum.
- Spatially, the refractive index becomes higher at the center of the beam than in the edges. This leads to spatial curvature that acts as a focusing lens for the beam, called *Kerr lens* or *self-focusing*.
- For very short and broadband pulses, the phase velocity of the pulse becomes time- and intensity-dependent, leading to a *self-steepening* effect.

Another effect resulting from the interaction of an intense pulse with atoms in a gas medium is ionization. The ionization probability increases strongly with the intensity. Ionization of a medium releases free electrons, which reduces the refractive index of the medium. This change of the refractive index induces a blue-shift of the spectrum. As the ionization is stronger at the center of the beam, the refractive index is smaller at the center than at the edges. This effect creating a defocusing lens is called *plasma defocusing*.

1.3 Filamentation

Post-compression techniques are used to compress laser pulses. They consist of broadening the spectrum through nonlinear effects, in order to be able to compress the pulse to a shorter duration. Post-compression can be achieved in hollow capillaries filled with gas [46] or by filamentation [47, 48], as in Paper I.

When focusing an intense ultrashort laser pulse in a gas, self-focusing occurs when the pulse peak power is higher than the *critical power* at which self-focusing balances diffraction. The self-focusing beam ionizes the medium, creating plasma defocusing. The process that leads to the formation of a long self-guided filament is illustrated in Figure 1.2. During filament formation, several nonlinear phenomena contribute to broadening the spectrum: self-phase modulation, self-steepening, ionization and plasma defocusing.

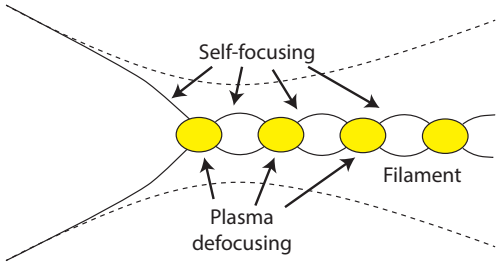

Figure 1.2: Filament formation: upon focusing, if the laser pulse peak power is higher than the critical power, the pulse starts self-focusing and ionizes the medium. When the plasma density is high enough it defocuses the beam, which can self-focus again. This process can repeat many times, forming a filament longer than the Rayleigh length.

1.4 Scaling of nonlinear optical processes in gases

Studying how the propagation of ultrashort pulses scales could ensure similar beam properties at smaller and longer scales, leading for instance to a higher energy throughput without being limited by a change of regime or new phenomena appearing at higher power. The scaling of nonlinear propagation of ultrashort pulses in a gas is presented in Paper I and [49]. We will describe the main equations and principles here.

In the propagation equation (Eq. 1.2), the Laplace operator can be separated into a longitudinal and a transverse component: $\nabla^2 = \Delta_\perp + \partial_z^2$. The equation can then be factorized as:

$$(\partial_z + ik)(\partial_z - ik)\hat{E} = -\Delta_\perp \hat{E} - \mu_0 \omega^2 \hat{P} \tag{1.5}$$

Leaving the right side apart, the left side represents two counter-propagating plane waves. One can neglect the backward propagation solution, which is equivalent to the approximation $[\partial_z + ik] \approx 2ik$ [50]. It leads to the Forward-Maxwell equation:

$$\left[\frac{\partial}{\partial z} - \frac{i}{2k}\Delta_\perp - ik\right]\hat{E} = \frac{i\omega}{2nc\epsilon_0}\hat{P}. \tag{1.6}$$

The first and second terms describe the wave propagation and diffraction, while the third term defines the spatial carrier wave propagating at the speed of light in vacuum c. The absolute location of the spatial carrier phase is not important here so we can perform the transformation $\hat{\mathcal{E}} = \hat{E}\exp[-i\omega z/c]$, which corresponds to a transformation from the laboratory frame to a frame moving at the vacuum speed of light with the wave [49]. The propagation

equation becomes:

$$\left[\underbrace{\frac{\partial}{\partial z}}_{①} - \underbrace{\frac{i}{2k}\Delta_\perp}_{②} - \underbrace{iK}_{③}\right]\hat{\mathcal{E}} = \underbrace{\frac{i\omega}{2nc\epsilon_0}\hat{\mathcal{P}}}_{④} \tag{1.7}$$

with $K = k - \omega/c$ and $\hat{\mathcal{P}} = \hat{P}\exp[-i\omega z/c]$. We are going to show that the wave equation is invariant when the parameters such as spatial dimension, gas pressure and pulse energy are scaled appropriately. Let us consider the nonlinear propagation of a Gaussian beam in a medium. The aim is to show that if $\hat{\mathcal{E}}(r, z, \omega)$ is a solution to the wave equation then $\hat{\mathcal{E}}(\eta r, \eta^2 z, \omega)$ will also be one, if the gas density is scaled as $\rho \to \rho/\eta^2$ and the pulse energy as $\epsilon_{in} \to \eta^2 \epsilon_{in}$. Let us examine the scaling of each term in Eq. 1.7:

① The scaling is clear:

$$\frac{\partial}{\partial z} \to \frac{1}{\eta^2}\frac{\partial}{\partial z}. \tag{1.8}$$

② Two terms need to be taken into account: k and $\Delta_\perp$

(a) k can be written as $k = n\omega/c = (\sqrt{1+\chi})\omega/c$ with χ the susceptibility of the medium, which is directly proportional to the gas density: $\chi \propto \rho$. As $\chi \ll 1$, k does not change with the scaling: $k \to k$. However, this approximation reaches its limit at high gas densities (see supplementary material of Paper I).

(b) it is clear that:

$$\Delta_\perp \to \frac{1}{\eta^2}\Delta_\perp \tag{1.9}$$

③ $K = k - \omega/c = (n-1)\omega/c$. For $\chi \ll 1$, $n \approx 1 + \chi/2$ thus $K \approx \chi\omega/(2)$. Therefore, K varies linearly with pressure and scales as:

$$K \to \frac{1}{\eta^2}K. \tag{1.10}$$

④ $\hat{\mathcal{P}}$ is the only variable here, and under the conditions considered for HHG and filamentation, varies linearly with the pressure. This term therefore scales as:

$$\hat{\mathcal{P}} \to \frac{1}{\eta^2}\hat{\mathcal{P}}. \tag{1.11}$$

Taking all the terms into account, both sides of Eq. 1.7 scale as $1/\eta^2$. This shows the scale invariance of the wave equation and the nonlinear phenomena it describes. However, $\mathcal{P}$

depends on the intensity. This implies that the intensity must be kept constant to conserve the scaling. Since the spatial dimensions of the beam have been scaled, the energy must be scaled accordingly to maintain the same intensity, i.e. as $\epsilon_{in} \rightarrow \eta^2 \epsilon_{in}$. This leads to the same transformation for the output energy: $\epsilon_{out} \rightarrow \eta^2 \epsilon_{out}$. As a summary, Table 1.1 recapitulates the scaling of the different parameters.

Table 1.1: Scaling of the different quantities.

	Parameter	Scaled parameter
Input energy	ϵ_{in}	$\eta^2 \epsilon_{in}$
Output energy	ϵ_{out}	$\eta^2 \epsilon_{out}$
Longitudinal dimension	z	$\eta^2 z$
Transverse dimension	r	ηr
Gas density	ρ	ρ/η^2

1.5 Experimental scaling of filamentation

Different approaches to increase the output energies of post-compression techniques have been suggested [51–58], but the maximum energies obtained by filamentation and hollow capillaries are currently limited to a few millijoules. The challenge is that when the pulse power greatly overcome the critical power, filaments tend to break into multiple filaments [44, 59, 60]. It limits the input pulse energy and thus the output energy accessible. There is a need for upscaling post-compression techniques, as we could use the resulting intense few-cycle pulses for the generation of high-pulse energy isolated attosecond pulses [61–64]. Upscaling filamentation could potentially lead to high output energies, i.e larger than 10 mJ, without multi-filamentation, as the ratio between the pulse peak power and the critical power remains unchanged upon scaling.

First, in order to test the scaling laws, we performed filamentation experiments as described in greater detail in Paper I. The experimental setup is shown in Figure 1.3. The 20 fs 1 kHz laser is focused by a curved mirror in a tube filled with argon. The focal length can be adjusted by changing the focusing mirror, and the laser energy can be tuned. A filament forms inside the gas, and the output is compressed by chirped mirrors, and characterized with the d-scan technique [65].

Focal length and gas pressure were changed according to the scaling laws. The spectrum, output energies and pulse duration were monitored. We adjusted the input energies between 0.12 mJ and 2.7 mJ to obtain filaments with the same spectral and temporal properties. The set of parameters used are displayed in Table 1.2.

The results are presented in Figure 1.4. In Figures 1.4 a) and Figure 1.4 b), the retrieved pulse duration and the spectrum are plotted for each set of parameters. As expected, they are very similar. In Figure 1.4 c), the parameters for each data point, chosen according to

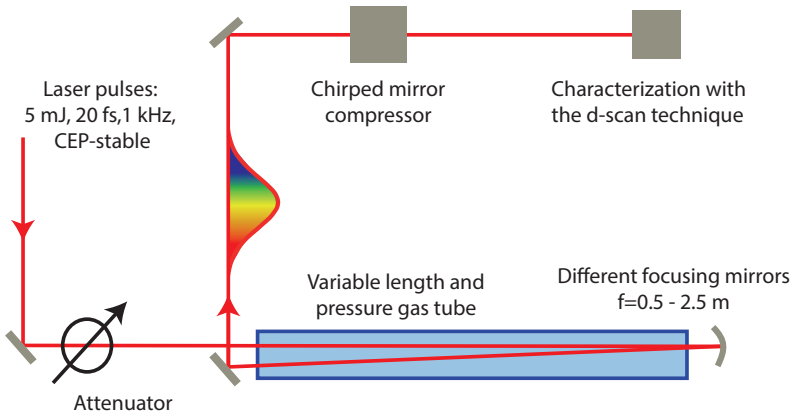

Figure 1.3: Setup used for demonstrating scaling for filamentation. The laser pulses are focused in a gas tube by curved mirrors. The length and pressure of the gas tube, pulse energy and focal length are adjusted according to the scaling laws. The pulses are then compressed and characterized spectrally and temporally.

Table 1.2: Experimental scaling parameters from Paper I, and Figure 1.4, with the corresponding color code.

Scaling parameter η	0.33	0.5	0.75	1	1.3	1.6
Focal length (m) $\propto \eta$	0.5	0.75	1	1.5	2	2.5
Pressure (bar) $\propto 1/\eta^2$	8	3.5	2	0.9	0.5	0.33
Input energy (mJ) $\propto \eta^2$	0.12	0.26	0.43	0.95	1.72	3

the scaling laws and given in Table 1.2, are displayed: the focal length as a function of the pulse energy along the blue line and the pressure along the red line. The fact that the beam properties are invariant for these carefully chosen parameters validates the scaling laws.

1.6 Toward high-energy filaments

We investigated further the typical parameters that filamentation to a larger scale would require. Due to the limit in pulse energy of the 1 kHz laser system and practical space constraints, higher energy necessitating a longer focal length, we built a high-energy filament setup close to the intense XUV beamline described in Section 3, using the 1 J 10 Hz laser system. The setup includes a 12-meter long vacuum tube installed on the side of the laser table, as shown in Figure 1.5 a). Thanks to a detuned telescope, presented in Figure 1.5, the focal length could be adjusted to 7.5 meters. The telescope consists of a focusing (+2 m) and a defocusing (−1 m) mirror approximately 1 m apart.

Since the laser used in this experiment has a different beam diameter than the one used previously in Section 1.4, the scaling of the parameters requires to consider the f-number $f_\# = f/D$. After optimization of the generation conditions, a filament was obtained with 10.3 mJ input energy, 18.2 mm iris opening and 140 mbar of Argon. The $f_\#$ with 18.2 mm

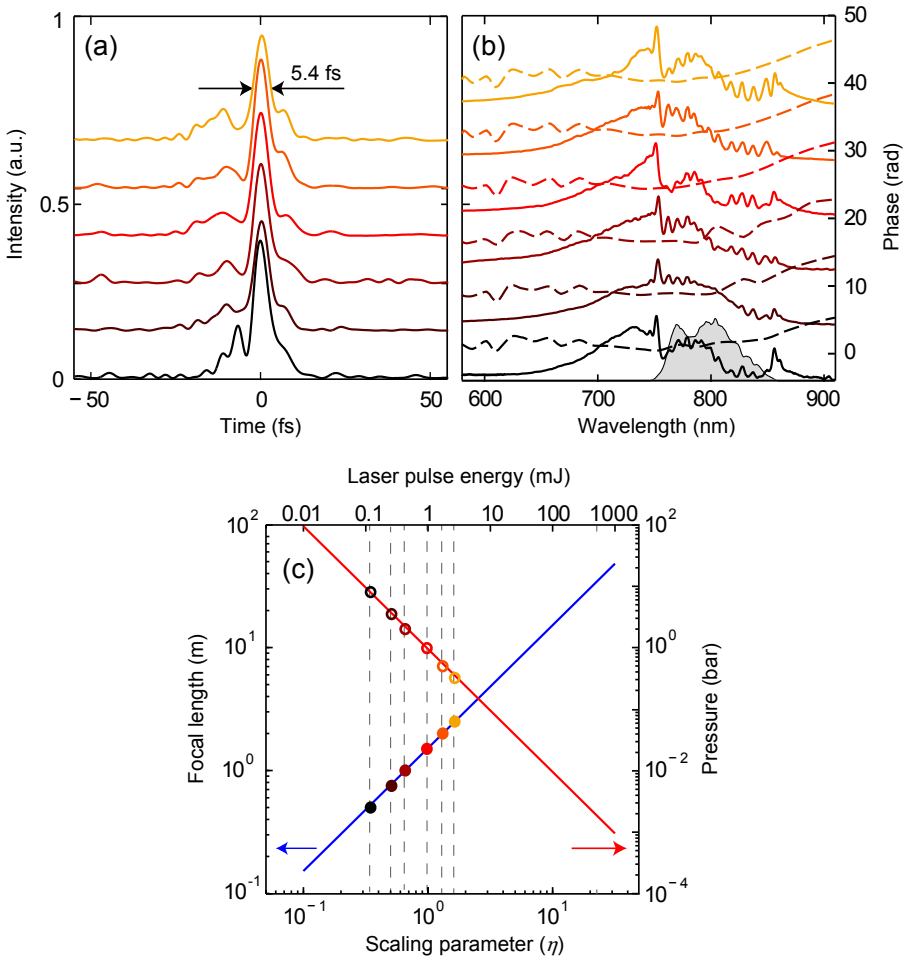

Figure 1.4: The results of the filament scaling experiment, reproduced from Paper I, a) the retrieved temporal profiles of the filaments, b) their spectra (solid lines) and spectral phase (dashed lines), in shaded gray the original laser spectrum, c) the different parameters sets of pressure, focal length and pulse energy. The solid lines are fits to the data, defined by the scaling laws.

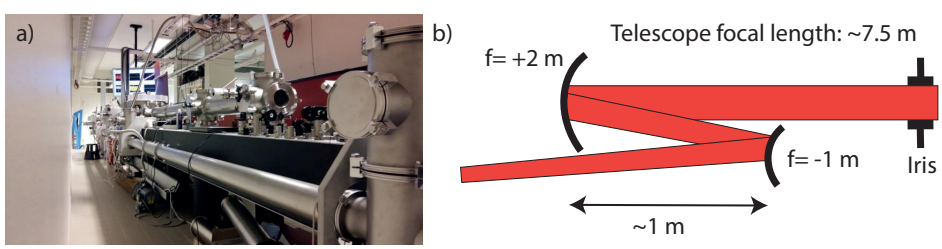

Figure 1.5: a) Long filament tube on the side of the intense XUV beamline. b) Telescope for long filament focusing, composed of one concave and one convex mirror. The length between them is adjusted to vary the total focal length.

iris and 7.5 m focal length is equal to 412, corresponding to a scaling parameter of $\eta = 2.7$ taking the same reference as in Table 1.2. The expected input energy is 7.1 mJ, and the gas pressure is 120 mbar. These parameters are quite close to those those we measured and are summarized in Table 1.3:

Table 1.3: Scaling parameters for the experiment of filament upscaling.

	experiment section 1.5	Upscaled filament	
focal length f (m)	1.5	7.5	
diameter D (mm)	9.9	18.2	
$f_\# = f/D \propto \eta$	150	412	
Scaling parameter η	1	2.7	
		expected	measured
Pressure (bar) $\propto 1/\eta^2$	0.9	0.120	0.140
Input energy (mJ) $\propto \eta^2$	0.95	7.1	10.3

The output energy was measured at 4 mJ (2.4 mJ at the core), and the output spectrum is plotted in Figure 1.6, along with the original laser spectrum. Spectral broadening is very clear, ranging from 600 to 900 nm. It is nevertheless not as broad as the previous experiments performed with the kHz system, because the spectrum of the 10 Hz laser is narrower than that of the kHz one (50 nm instead of 80 nm). Thus, the pulses are longer (40 fs instead of 20 fs), so the compressibility of the resulting filaments is not as good. We measured 12 fs pulses instead of 5.4 fs. The spatial quality of the laser was also slightly poorer. The output energy of these filaments was around 4 mJ, which is high for a single filament. This encouraging result proves that using intense lasers in loose focusing with appropriate scaling conditions may lead to short, intense filaments.

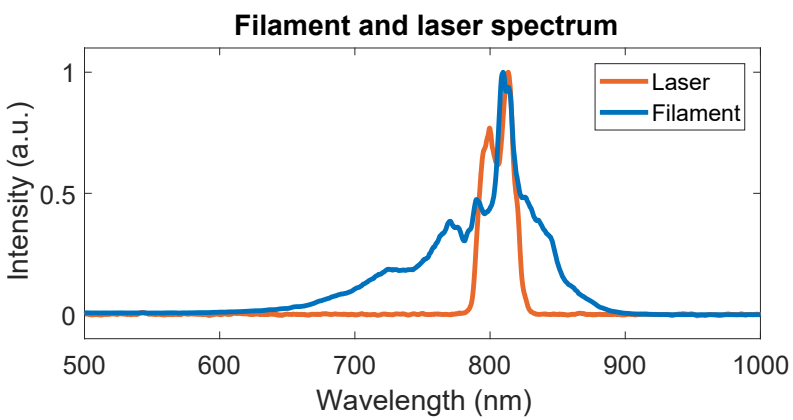

Figure 1.6: The measured spectra of the 10 Hz laser, and that of the obtained filament. It presents significant spectral broadening.

2 High-order Harmonic Generation

2.1 Three-step model

When an intense linearly-polarized electromagnetic field interacts with an atom, a highly nonlinear process can happen: High-order Harmonic Generation (HHG). This remarkable phenomena was observed for the first time in 1987 in the form of a harmonic plateau followed by a sharp cut-off. It could be explained not by regular perturbative nonlinear optics but by strong field physics, the regime where the electric field is on the order of the atomic potential. This phenomenon was first described by numerically solving the time-dependent Schrödinger equation (TDSE) for a single active electron [66, 67]. A simple semi-classical three-step model offering a very good understanding of the physics of HHG was also derived [68, 69].

In this model, an electron is first ionized from the atom (by tunneling or multiphoton ionization). It is then accelerated by the laser field and gains kinetic energy. Finally there is recombination, whereby the electron recombines with the parent ion and the excess energy is emitted in the form of a burst of extreme-ultraviolet (XUV) radiation. The total energy is the sum of the kinetic energy upon the return of the electron and the ionization energy. These three steps are represented in Figure 1.7.

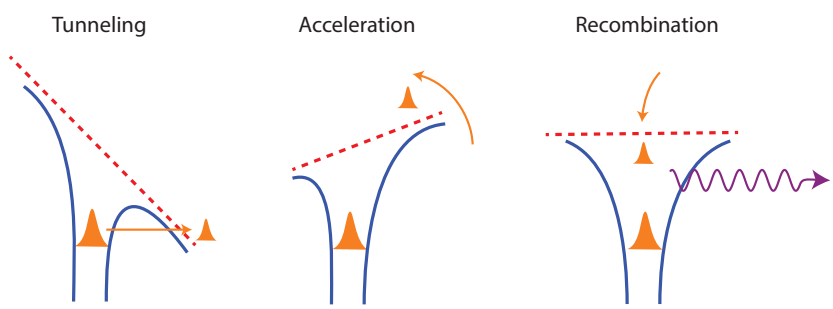

Figure 1.7: Illustration of the three-step model: an electron is ionized by the strong laser field, is accelerated and recombines with the atom, emitting XUV radiation.

The trajectory and energy acquired by the electron (step 2) can be derived from the laws of classical mechanics, Newton's Second Law. Let us consider an electron just after tunneling at time t_i, position $x(t_i) = 0$ and initial velocity $\dot{x}(t_i) = 0$. The sinusoidal laser driving field of carrier frequency ω_0 and amplitude E_0 accelerates it. Newton's law yields:

$$\ddot{x}(t) = -\frac{eE_0}{m_e} \sin(\omega_0 t), \tag{1.12}$$

where e and m_e are the charge and mass of the electron. This can be temporally integrated

as:

$$\dot{x}(t) = \frac{eE_0}{m_e\omega_0}[\cos(\omega_0 t) - \cos(\omega_0 t_i)], \tag{1.13}$$

and:

$$x(t) = \frac{eE_0}{m_e\omega_0^2}[\sin(\omega_0 t) - \sin(\omega_0 t_i) - \omega_0(t - t_i)\cos(\omega_0 t_i)]. \tag{1.14}$$

The possible trajectories (Eq. 1.14) are represented in Figure 1.8 a) for different ionization times t_i. Some of the trajectories come back to the atom, such that the electron may combine with it (step 3). The energy accumulated for a trajectory can be calculated from Eq. 1.13 as a function of ionization time t_i and return time t_r:

$$E_{kin} = \frac{1}{2}m_e\dot{x}^2(t_r) = \frac{e^2E_0^2}{2m_e\omega_0^2}[\cos(\omega_0 t_r) - \cos(\omega_0 t_i)]^2 = 2U_p[\cos(\omega_0 t_r) - \cos(\omega_0 t_i)]^2 \tag{1.15}$$

where U_p is the ponderomotive energy, i.e., the mean energy of an electron oscillating in the driving field. The return times t_r are the solutions of $x(t_r) = 0$, i.e.,

$$\sin(\omega_0 t_r) - \sin(\omega_0 t_i) - \omega_0(t_r - t_i)\cos(\omega_0 t_i) = 0 \tag{1.16}$$

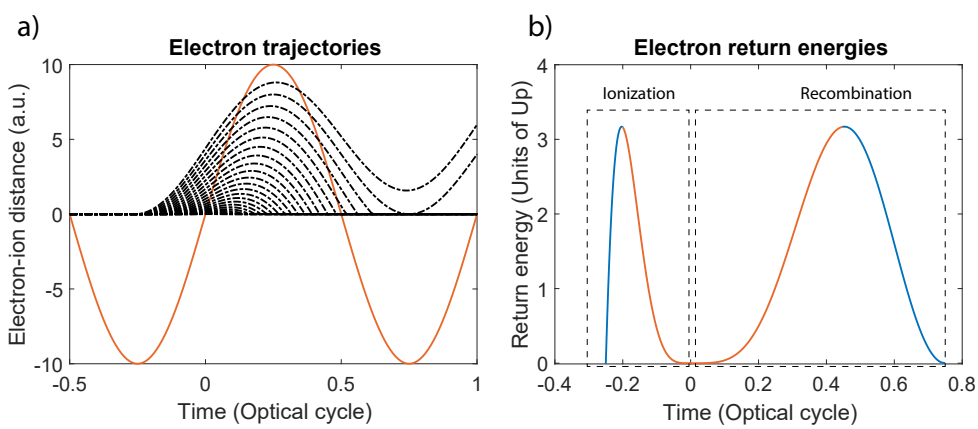

Figure 1.8: a) In black, some of the possible electron trajectories during a half-cycle of the driving field. Except for the top trajectory, they return to the parent ion. In orange, the driving laser field. b) Return energies plotted as a function of ionization time (left) and recombination time (right). In blue for the long trajectories, in orange for the short ones.

Kinetic energy as a function of t_i and t_r is plotted in Figure 1.8 b). There are two trajectories, short and long, that lead to the same return energy. The maximum kinetic energy is $3.17\,U_p$. The energy of the emitted photon is $E = E_{kin} + I_p$ with I_p the ionization potential of the

atom. Thus, the maximum reachable energy is $E_{max} = 3.17U_p + I_p$. This is called the cut-off law. It depends on the laser intensity I since U_p is proportional to I, and on the frequency ω_0. Possible photon energy ranges from a few electron-volts to a few hundreds electron-volts.

The probabilities for the different trajectories are similar, which leads to a plateau where many harmonics have similar intensity. Around the maximum energy, the intensity decreases quickly with energy: it is the cut-off region.

This process happens every half-cycle of the driving field, emitting XUV bursts each time and forming a train of attosecond pulses separated by $T/2$, with T the laser period. They interfere together, leading to a spectral selection of odd harmonics, spaced of $2\omega_0$. The longer the driving field the narrower the harmonic width. Conversely, if the driving field is only one cycle long, only one or two bursts are generated such that the interference process does not take place. Under some conditions, this can result in an isolated attosecond pulse (IAP) which has a broad spectrum with all the possible return energies.

2.2 Intensity-dependent dipole phase

The different frequency components generated at different times as seen in Figure 1.8 a), the short trajectories before the long ones, lead to a chirped attosecond pulse. During travel in the continuum, the electron acquires indeed a delay that is linked to the length of its trajectory. This is called the *dipole phase*, because the negative electron and the positive ion form an electric dipole. It is possible to predict this phase with Strong Field Approximation (SFA) calculations [70]. This phase depends on the intensity of the field.

The dipole phase is often expressed as a function of parameter $\alpha^{s,l}$ for either short or long trajectories:

$$\varphi^{s,l}(\Omega, r, z) = -\alpha^{s,l}(\Omega, I)I(r, z) \tag{1.17}$$

where Ω is the frequency of the emitted radiation and I the intensity of the laser beam. A problem with this formula is that $\alpha^{s,l}(\Omega, I)$ is dependent on intensity I [71–73]. Calculations requiring the knowledge of the phase over a large range of intensities in general use tabulated α values, obtained within the SFA. A more general analytical formula that was recently developed is derived below [74, 75]. The derivation is also described in Paper VI.

Figure 1.9 shows frequency Ω of the emitted radiation as a function of the electron return time, for two different IR intensities. This is similar to the right side of Figure 1.8 b), plotted in emitted frequency instead of return energy. The frequency is represented between threshold frequency $\Omega_p = I_p/\hbar$ and cut-off frequency $\Omega_c = (3.17U_p + I_p)/\hbar$. The return times for the short trajectories range between t_s and t_c and for the long ones between t_c and

t_l. For both intensities and trajectories, we approximate the return time of the electron by straight lines, and define the return times t_p^s, t_c^s,t_c^l and t_p^l as noted in Figure 1.9.

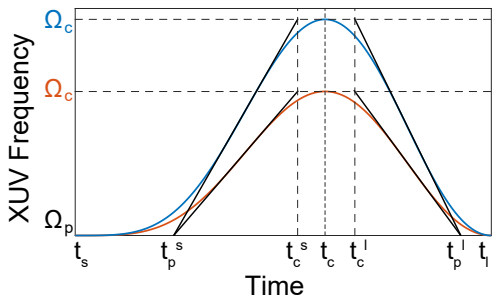

Figure 1.9: Emitted XUV frequency (blue and red solid lines) as a function of return time for two laser intensities. The short trajectories return between t_s and t_c, and the long ones between t_c and t_l. For every intensity, we can approximate the curves by straight lines that have the same starting and ending points: t_p^s and t_c^s for the short, t_c^l and t_p^l for the long.

With this approximation, the time of electron return $t^{(s,l)}(\Omega)$ can be written as:

$$t^{(s,l)}(\Omega) \approx t_p^{(s,l)} + \frac{t_c^{(s,l)} - t_p^{(s,l)}}{\Omega_c - \Omega_p}(\Omega - \Omega_p) \tag{1.18}$$

This can be interpreted as a group delay of the emitted radiation. Its integral is the spectral phase:

$$\Phi^{(s,l)}(\Omega) = \Phi^{(s,l)}(\Omega_p) + t_p^{(s,l)}(\Omega - \Omega_p) + \frac{t_c^{(s,l)} - t_p^{(s,l)}}{\Omega_c - \Omega_p}\frac{(\Omega - \Omega_p)^2}{2} \tag{1.19}$$

The second term is independent of the intensity. The coefficient in the third term can be written as:

$$\frac{t_c^{(s,l)} - t_p^{(s,l)}}{\Omega_c - \Omega_p} = \frac{2\gamma^{(s,l)}}{I} \tag{1.20}$$

where $\gamma^{(s,l)} = (t_c^{(s,l)} - t_p^{(s,l)})\pi c^2 m/(3.17\alpha\lambda^2)$. Classically, we consider $\Phi^s(\Omega_p) = 0$ for the short trajectories, while it is proportional to the intensity $\Phi^l(\Omega_p) = \alpha_0^l I$ for the long ones.

For a 800 nm laser field, the values of the introduced parameters are [74]:

$$\begin{aligned}
\beta^{(s)} &= 0.4758 \text{ fs} \\
\beta^{(l)} &= 1.8496 \text{ fs} \\
\gamma^{(s)} &= 1.030 \times 10^{12} \text{ fs}^{\,2}\text{W cm}^{-2} \\
\gamma^{(l)} &= -0.874 \times 10^{12} \text{ fs}^{\,2}\text{W cm}^{-2} \\
\alpha_0^{(s)} &= 0 \\
\alpha_0^{(l)} &= -2.376 \times 10^{-13} \text{ W}^{-1}\text{cm}^2
\end{aligned} \tag{1.21}$$

To summarize, the spectral phase of the attosecond pulses can be approximated, for both long and short trajectories, by:

$$\Phi(\Omega) = \alpha_0^l I + t_p^{(s,l)}(\Omega - \Omega_p) + \frac{\gamma^{(s,l)}}{I}(\Omega - \Omega_p)^2 \tag{1.22}$$

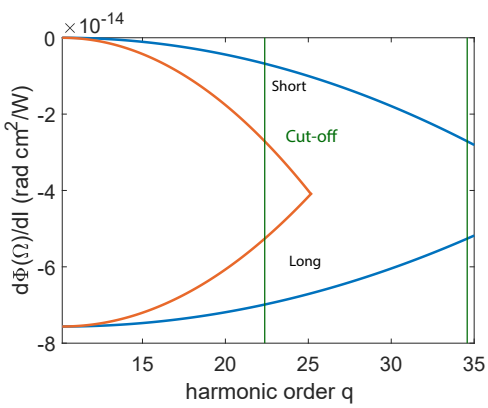

Figure 1.10: Derivative of the dipole phase over the intensity as a function of the harmonic order. The short (top) and long (bottom) trajectories are plotted, for two different intensities. The calculations were made for a 800 nm driving field in argon, for $I = 10^{14}$ W/cm^2 (orange) and $I = 2 \times 10^{14}$ W/cm^2 (blue). The cut-off frequency for each intensity is plotted as a green line.

We calculated the derivative of the dipole phase over the intensity, which corresponds to the traditional α, for a 800 nm driving field in argon. The results are shown in Figure 1.10. The long trajectories have a stronger phase variation than the short ones. When the harmonic order increases, the two tend to converge close to the cut-off [71, 72]. The results are presented for two different intensities: $I = 10^{14}$ W/cm^2 (orange) and $I = 2 \times 10^{14}$ W/cm^2 (blue). The corresponding cut-off frequencies are indicated by the green lines.

The formula from Eq. 1.22 will be used in Chapter 2 to investigate the influence of the dipole phase on the spatial properties of the harmonics.

2.3 Phase matching

So far, only the single-atom response has been considered. However, HHG results from the coherent addition of the emission from an ensemble of atoms. Efficient HHG builds up in the medium when phase matching is realized, i.e. when the radiation coming from all the atoms in the medium is in phase. This process is illustrated in Figure 1.11. For the q^{th} harmonic, the phase mismatch is expressed as $\Delta k = qk - k_q$ with k_q the wavevector of the q^{th} harmonic and k the wavevector of the IR. The conversion efficiency is maximized for $\Delta k = 0$ and decreases quickly as Δk increases.

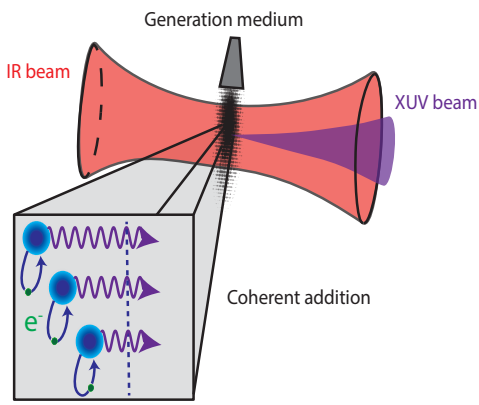

Figure 1.11: Concept of phase matching: many atoms in the gas emit radiation from the recombination, which are added in a coherent process: the radiation emitted in phase adds up constructively , forming the XUV beam.

Four main components contribute to the phase mismatch, which can be expressed as

$$\Delta k = \underbrace{\Delta k_G}_{①} + \underbrace{\Delta k_n}_{②} + \underbrace{\Delta k_p}_{③} + \underbrace{\Delta k_D}_{④} \tag{1.23}$$

① Gouy phase gradient: the Gouy phase is the difference between the on-axis phase of a Gaussian beam and that of a plane wave. The Gouy phase of the harmonic is usually neglected. Δk_G is the gradient of the fundamental Gouy phase and is always negative.

② Neutral dispersion: the driving field and the harmonic beam experience different indexes of refraction, which introduces a dispersion phase mismatch. The gradient of the neutral dispersion is $\Delta k_n = q\omega_0/c \times (n_1 - n_q)$, and is always positive as $n_1 > n_q$.

③ Plasma dispersion: similarly, the free electrons in the plasma introduce dispersion. The plasma dispersion gradient is proportional to the variation of refractive index caused by the free electrons. It is always negative.

④ The gradient of the dipole phase described above. It is positive for $z > 0$ and negative for $z < 0$, and shows strong variations along the radial direction (x,y) and the propagation direction z.

Through the four contributions described above, Δk depends on the gas pressure, the ionization rate, the laser intensity and the focusing conditions. It is clear that strict achievement $\Delta k = 0$ for all positions x,y,z and time is not possible, as all the components vary spatially and temporally. However the complex interplay of these four components gives some flexibility and it is possible to achieve satisfying phase matching over significant volumes. The experimental parameters to optimize generation are beam energy, beam size (so the *f*-number), gas pressure and focus position compared to the gas medium. The choice of cell length is also important, because of the trade-off between quasi-coherent build-up and reabsorption of harmonics in the medium.

2.4 Scaling of HHG and loose focusing

During the HHG process, the driving field induces a polarization $P_q = 2d_q\rho$ for each harmonic frequency upon propagation in the gas medium, with d_q being the dipole moment and ρ the gas density. It is possible to describe the propagation of the generated harmonic field by Eq. 1.7, using the nonlinear polarization P_q. HHG is a nonlinear phenomena that can be scaled according to the laws described in Section 1.4.

In Paper 1, numerical simulations were presented with the parameters scaled by $\eta = 16$, corresponding to a change in input energy of 256. The resulting HHG behavior was found identical, thus validating the scaling laws. The conversion efficiency of the process remains the same upon scaling, and the output energy follows the same scaling as the input energy, $\epsilon_q \rightarrow \eta^2\epsilon_q$.

Loose focusing geometry with long focal length, long interaction volume, low gas density and high pulse energy has the same conversion efficiency as a tight focusing, short interaction volume, high gas density and low pulse energy. It also lead to a higher output energy since a higher input energy is required. The focal length scales as η and the output energy as η^2 [76]. This principle was applied phenomenologically for the generation of intense XUV flux as early as 2002 in CEA [29] and RIKEN [27], then in FORTH [77] and the intense XUV beamline in Lund [26, 76], as presented in the next section. More recently, the design of the GHHG LONG beamline in ELI-ALPS was based on this concept [78, 79].

Scaling concepts were also applied in the other direction for tight focusing geometries, required with low-energy high-repetition rate laser systems [80, 81].

3 Intense XUV beamline

Most of the work on this thesis has been performed in the intense XUV beamline of the Lund High-Power Laser Facility. A lot of technical development has been done during the past four years. The laser beam path was shortened, partly placed under vacuum, and the pointing was stabilized to ensure a better beam quality. The focusing of the beam was improved, a lens was replaced by a deformable mirror and a metallic focusing mirror. The beamline was expanded with a chamber devoted to interferometers. Two particle detectors and the XUV-XUV interferometer were developed and installed. Finally, many alignment and acquisition softwares were automatized and synchronized. The focus of the work on the beamline shifted from optimizing the flux of the harmonics to using them for nonlinear experiments.

We describe here the present setup of the intense XUV beamline. IR pulses are provided by the 10 Hz TW laser system described in Section 1.1. The pulses are temporally compressed to 40 fs and the beam enlarged to a FWHM diameter of 24 mm. The pulse energy for optimal generation is around 20 mJ. The beam is reflected on a 70 mm diameter deformable mirror (AKA Optics) which includes 32 actuators, and apertured by an iris to a diameter between 20 and 30 mm. The beam enters a vacuum and is focused by a metallic curved mirror. An IR wavefront sensor images the deformable mirror to correct the aberrations. The laser is focused in a gas cell filled by a pulsed jet, generally with argon. A scheme of the setup is shown in Figure 1.12.

The generated harmonics co-propagate with the IR beam for 4 meters, and are reflected on a Fused Silica (FS) plate, which is Anti-Reflection (AR) coated in order to filter out most of the IR radiation. For time-resolved experiments, this silica plate can be replaced by a split-and-delay unit, which will be described in Chapter 4. The remainder of the IR is filtered through a metallic filter, usually 200 nm of aluminum. A rotating gold mirror permits transmission of the beam to an XUV spectrometer. An example of a measured spectrum is presented in Figure 1.13 a). The beam propagates to the interaction chamber, where it is focused by the XUV optics presented in Chapter 3 and in Paper IV. In the focal region, a pulsed valve introduces a gas with the atoms or molecules that are investigated. Particle detectors monitor the ions and electrons originating from the interaction between the XUV and/or IR pulses and the gas. Approximately 50 cm after the interaction region photon detectors are placed to monitor the XUV beam. Using a calibrated CCD camera and a photodiode (see below), 5 nJ total XUV energy has been measured in this chamber (Paper VI). The beam profile is also recorded, as in Figure 1.13 b).

Pulsed valve An Even-Lavie pulsed valve [82] is placed on top of the interaction chamber. When the valve opens, a high-pressure gas is sent into the chamber toward the interaction

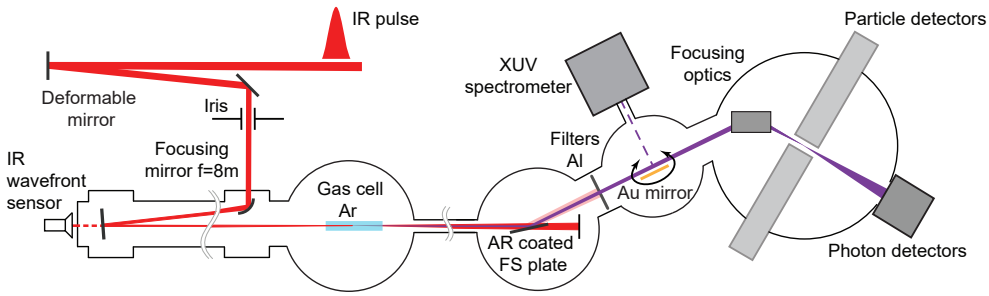

Figure 1.12: Scheme of the intense XUV beamline

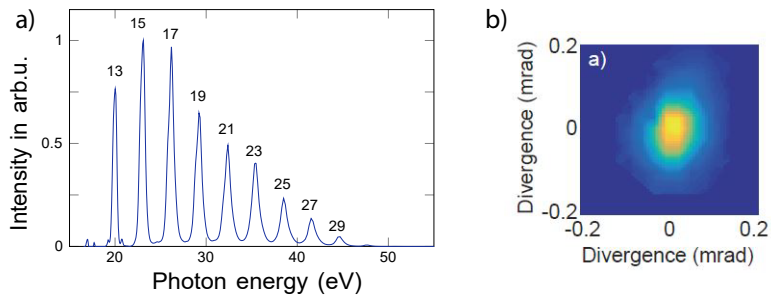

Figure 1.13: a) Typical harmonic spectrum measured with the XUV spectrometer. The harmonic orders are identified. b) Typical beam profile measured with the XUV CCD camera.

region. The gas goes through two conical skimmers, creating a dense collimated supersonic jet. The valve aperture time and repetition rate can be tuned. The diameter of the beam, defined by the second skimmer, is 1 mm. A small cylinder inside the valve can be filled with liquid or solid samples, and heated until evaporation. The atoms and molecules are pushed toward the valve and the interaction region with a noble gas such as Helium. This allows for more flexibility and gives the possibility to perform experiments with complex molecules.

3.1 Photon detectors

Photodiode An XUV photodiode is calibrated to measure the energy of the XUV pulses, allowing for shot-to-shot measurement of the value of the pulse energy, which can be useful for partial covariance analysis (see Section 3.2 and Paper III). It also permits monitoring of the fluctuations of the XUV energy and thus indirectly that of the IR. It is placed on a movable mount, so it can be removed to let the pulses reach an XUV camera.

Andor CCD camera An XUV CCD camera is used to acquire and monitor the spatial profile of the beam, and is calibrated to measure pulse energy. It can also be used to monitor the splitting by the split-and-delay unit (see Chapter 4). A mask with holes can be inserted before the camera to measure the beam wavefront (see Chapter 2).

XUV Microscope An XUV microscope was also developed for focal spot characterization and will be described in Chapter 3.

3.2 Particle detectors

Goals In light-matter interaction experiments with XUV photons, interesting observables are the momenta of the electrons and ions created by ionization, from which the energy and angular distribution of these fragments can be obtained. In order to access this information, the fragments are accelerated with electric fields, and their position (x, y) and/or their arrival time t is recorded on a detector. Depending on the configuration it is possible to retrieve their initial momentum (p_x, p_y, p_z).

A reaction microscope REMI [83] allows for acquisition of both the x, y position and the arrival time. If the flux is low enough to yield less than one event per pulse, it is possible to detect the fragments in coincidence. This allows for retrieving a complete molecular frame photoelectron angular distribution. By varying the delay between a pump and a probe pulse to observe different moments of the reaction, a "molecular movie" can be obtained. However, this requires a high repetition rate source to get significant statistics, and poses many technical challenges. Experiments with intense harmonic sources such as that developed in this work often have many events per shot (~ 1000) and typically low repetition rates ($10 - 100$ Hz). We are therefore more interested in recording many events and using a statistical analysis such as a covariance technique to extract information (see Paper III). Our apparatus for detection of ions and electrons, the Double Velocity Map Imaging Spectrometer (DVMIS), is described in Paper III, along with some results. Here we explain the working principle of two detectors used in this work, time-of-flight (TOF) and velocity map imaging (VMI).

Time-Of-Flight In a basic TOF spectrometer, the particles are accelerated by a strong electric field around the interaction region. Passing through a grid, they enter a long field-free drift region (flight tube) where they propagate until they arrive to a detector, often a micro-channel plate (MCP). Their arrival time depends on their mass, and the arrival position depends on their initial velocity. The grid ensures that the particles are accelerated only in the longitudinal direction.

The concept was further improved with the Wiley-McLaren TOF spectrometer [84]. A second acceleration region is added after the first one and tuning the ratio of the voltages in these two regions leads to a better resolution. Two particles with the same mass but from different regions arrive at the same time on the detector.

Velocity Map Imaging By replacing the grid with an open electrode, the electric field forms a focusing lens. The transverse initial velocities (p_x, p_y) lead to different positions (x, y) on the detector. The electrode ratio can be tuned to ensure that the position on the detector depends only on the transverse momentum (called the *VMI mode*). An additional mode called *spatial mode* consists of mapping the magnified position in the focal region on the detector instead of the initial energy distribution.

In order to record both electrons and ions simultaneously for each pulse, a new double-sided particle spectrometer was developed, presented and tested in Paper III. The principle is represented in Figure 1.14. A phosphor screen converts particles from the MCP to visible light, which is observed with a CCD camera.

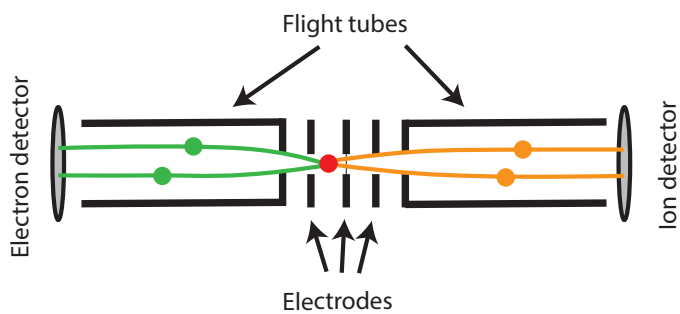

Figure 1.14: Principle of the DVMIS. Electrons (green) and ions (orange) generated in the interaction region (red) are accelerated into the flight tubes toward the detectors.

A conclusive proof-of-principle test of the DVMIS with N_2 molecules was conducted and is described in Paper III. The DMVIS was operated in different photo-electron and photo-ion detection modes: ion TOF, ion VMI, electron VMI. The covariance mapping technique was applied to mass selection of photo-ions and information about the specific ionization channels was extracted from photoelectron spectra. Other species will be investigated in the future.

3.3 Two-photon double ionization

Double ionization of atoms of molecules with one energetic photon is typically studied at synchrotron facilities, where photon energy can be high enough to exceed the double ioniz-

ation threshold (for instance 62.5 eV in neon) [85, 86]. Multiphoton ionization is possible with XUV photons because absorption of a few XUV photons can overcome ionization thresholds [30, 31, 87]. This requires nevertheless a higher intensity on target, on the order of 10^{12} W/cm^2.

In Paper II we report the two-photon double ionization (TPDI) of neon by intense XUV attosecond pulses. We observed a quadratic variation of the Ne^{2+} signal with the intensity, proving that it is created through a nonlinear two-photon process. There are two possible channels to achieve the TPDI: direct and sequential, as depicted in Figure 1.15. While they both involve absorption of two photons and lead to a doubly charged ion, they differ in two ways. For the direct channel, the two electrons are emitted back-to-back and share the extra energy continuously. For the sequential channel the electrons have discrete energies corresponding to the excess energy for each ionization step [88]. The second difference is the temporal behavior. The intermediate ionic state has a long lifetime, while the direct process cannot happen if the atom had time to relax into the intermediate state. The ratio between the yield of the two processes depends on the timescale. For instance, the transition between the two processes happens slightly below one femtosecond in the case of helium [88].

In our experiment, we investigated whether we could observe the direct process. The second step of the sequential process, which requires photon energy of 40.9 eV, gives us a way to experimentally distinguish these processes. We generated harmonics in krypton up to 45 eV and observed Ne^{2+} with the time-of-flight spectrometer. With the same total flux but a lower cut-off, up to 38 eV, we did not detect Ne^{2+} anymore. This supports domination of the sequential process, even though only the few most energetic harmonics ($\hbar\omega \geq 40.9$ eV) could contribute to the second step of the sequential process.

The low cross-sections of these processes make these experiments challenging, and the available XUV flux is not strong enough to obtain sufficient statistics to observe electron rings on the VMI. The work described in Paper II is nevertheless proof that we can realize nonlinear experiments and measure atomic cross-sections. The road toward further perspectives of nonlinear time-resolved experiments will be described in Chapter 4.

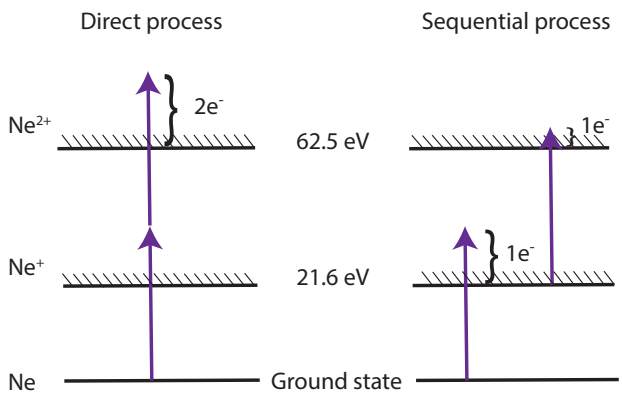

Figure 1.15: Energy diagram representing the direct and the sequential process of the two-photon double ionization of neon and the corresponding energies of the emitted photoelectrons.

Chapter 2

Spatial metrology of high-order harmonics

The spatial metrology of laser beams consists of measuring and assessing such properties as the shape of the spatial profile and the deformation of the wavefront, or spatial phase. It is important to have a beam with good spatial quality in order to use it for diverse applications. This chapter introduces the concepts and setup that we use to assess the quality of the high-order harmonic beam. First, the Gaussian formalism we use to describe our laser beam is presented, followed by an introduction to the concept of optical aberration and a description of the most important aberrations we encounter. The method of measuring the wavefront (or phase) of a beam is then explained. Transfer of aberrations from the IR to the XUV beam is also explored. Finally, the results of wavefront measurements are presented, along with a discussion of the ways the IR beam influences the aberrations of the XUV beam.

1 Theoretical background

1.1 Summary of Gaussian optics

Gaussian beams are a solution to the paraxial Helmholtz equation, which describes wave propagation in the small-angle approximation, i.e. the propagation of waves that have small angles with the optical axis. Gaussian beams are often a good mathematical description of laser beams. The electric field of a Gaussian beam propagating along the z direction can be

written as:

$$\widetilde{U}(r,z) = U(r,z)\exp\left(-i\phi(r,z)\right) \tag{2.1}$$

$$\text{with} \quad U(r,z) = U_0 \frac{W_0}{W(z)} \underbrace{\exp\left(-\frac{r^2}{W^2(z)}\right)}_{\text{Gaussian profile}} \tag{2.2}$$

$$\text{and} \quad \phi(r,z) = \underbrace{kz}_{\text{Propagation}} + \underbrace{k\frac{r^2}{2R(z)}}_{\text{Spherical phase}} - \underbrace{\arctan\left(\frac{z}{z_R}\right)}_{\text{Gouy phase } \zeta(z)} \tag{2.3}$$

where R is the radius of curvature of the beam wavefront, W the $1/e^2$ of the intensity waist, z_R the Rayleigh range, and r the radial coordinate $r = \sqrt{x^2 + y^2}$. The spatial profile $U(r,z)$ is a 2D Gaussian defined by the waist W(z), U_0 and W_0 are the amplitude and waist at $z = 0$. The spatial phase $\phi(r,z)$ is composed of three terms, a propagation term along z, a spherical phase determined by the radius of curvature $R(z)$, and the Gouy phase $\zeta(z)$, which represents the difference of phase between a Gaussian and a plane wave during the propagation along z. The Rayleigh range z_R is the distance over which the beam waist $W(z)$ is$\sqrt{2}$ times W_0. The waist variation is plotted in Figure 2.1 a) and expressed as:

$$W(z) = W_0\sqrt{1 + \frac{z^2}{z_R^2}}. \tag{2.4}$$

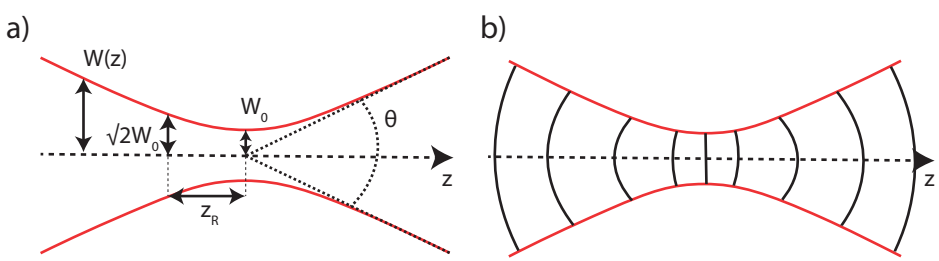

Figure 2.1: a) Waist variation along propagation direction z. At the position of the Rayleigh range $z = z_R$, the beam is$\sqrt{2}$ bigger than at the waist. b) Curvature evolution along the propagation direction. The curvature is largest for $z = z_R$.

Beam curvature and wavefront For a Gaussian beam, the wavefront (i.e. surfaces of equal phase) is plane in the focus, then become curved, such that the radius of curvature decreases and the curvature (the inverse of the radius of curvature) increases, reaching a maximum curvature for the Rayleigh range z_R. Afterwards, the curvature decreases until the wavefront becomes flat again at infinity. This evolution is illustrated in Figure 2.1 b) and Figure 2.2.

The evolution of the radius of curvature of a Gaussian beam is given by:

$$R(z) = z + \frac{z_R^2}{z}. \tag{2.5}$$

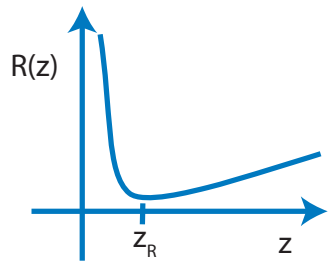

Figure 2.2: Evolution of the radius of curvature as a function of z, reaching a minimum for the Rayleigh length z_R.

Focusing a Gaussian beam The Rayleigh length is expressed as:

$$z_R = \frac{\pi W_0^2}{\lambda}. \tag{2.6}$$

$2z_R$ is called the depth of focus or confocal parameter.
In this focal region $z - z_f < |z_R|$, the beam width is no larger than $\sqrt{2}W_0$ and the peak intensity is more than $0.5I_0$. A beam with a small waist has a short depth of focus, reffered to as "tight" focusing, as opposed to "loose" focusing.

Divergence in the far field of a Gaussian beam is expressed as:

$$\theta = \frac{\lambda}{\pi W_0}. \tag{2.7}$$

When focusing a collimated Gaussian beam of diameter D with a lens of focal length f, the resulting diameter in the focus can be approximated by:

$$2W_0 \sim \frac{4\lambda f}{\pi D}. \tag{2.8}$$

The smaller the wavelength or the larger the diameter of the beam before focusing is, the smaller the focal spot.

1.2 Aberrations in optical systems

Definition

When a point is imaged through an ideal optical system, all rays coming from the object point have the same optical path length. They meet in the same point, called the image point. The conjugation of these two points by the optical system is called stigmatic. However, in a real optical system, some rays may take paths with different optical path length, and not meet at the image point. This deviation from the stigmatic conjugation is called aberration. Some geometric shapes are stigmatic when used between infinity and the focus of a parabola, the two focii of an ellipse, or the two focii of an hyperboloid. Working outside these specific points or with other shapes gives rise to aberrations. The rays that are

close to the optical axis and have small angles, called paraxial rays, give rise to negligible aberrations: this is referred to as the paraxial approximation.

The transition from ray optics to wave optics can be made considering that the rays are parallel to the local wavevectors k. The wavefronts are thus the surfaces perpendicular to the rays. This is illustrated in Figure 2.3. These wavefronts are aberrated after going through an optical system. It is possible to study aberrations both with wavefront and ray optics.

An aberrated wavefront leads to a degradation of the beam focusing quality, that is why we first want to study the aberrations of the beam, in order to optimize its focusing to a small spot (see Chapter 3).

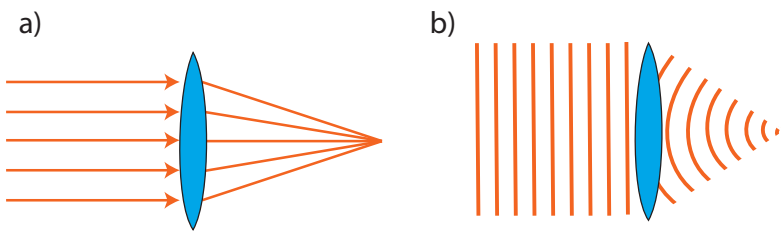

Figure 2.3: a) Ray optics representation of the focusing by a lens. b) Wavefront representation.

The concept of point source comes from geometric optics. In reality, the image spot has a certain size because of diffraction. The challenge of optical design is to weight how much the aberrations compromise imaging quality, depending on the limiting factor between aberrations, diffraction and detector resolution. We here consider only geometric optics.

Wave aberration We define aberration as the optical path length difference between a reference spherical wavefront that would produce perfect focusing, and the real wavefront. If we consider a reference wavefront $W_{F\text{ref}}$ in Figure 2.4 a), the aberration is the optical path length difference ΔW_F between the real wavefront W_F and $W_{F\text{ref}}$. A widely used metric to quantify the aberration is the root-mean square (RMS) of the wavefront error: RMS $= \sqrt{< (W_F - W_{F\text{ref}})^2 >}$, with $<>$ denoting the average over the wavefront. Another often used metric is the Peak-to-Valley (PV), the difference between the two extreme points of the wavefront compared to the reference: PV $= \Delta W_{F\text{min}} - W_{F\text{max}}$. Aberrations are expressed in length units (often nm), and can also be written as units of the light wavelength. One parameter is often not enough to describe wavefront quality; for instance in Figure 2.4 a), the two wavefronts have the same PV but a different RMS. Wave aberration disturbs the image formation. Due to local wavefront deformations, the rays coming from different parts of the wavefront do not form the image at the same place as the ray coming from the reference sphere, as shown in Figure 2.4 b).

Let us consider an optical system that is imaging an object point B, located along the vertical

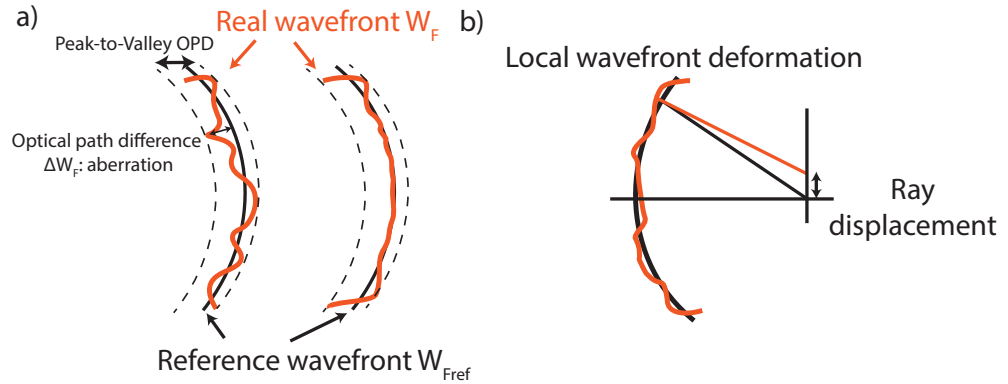

Figure 2.4: a) Wave aberration: optical path difference (OPD) between the perfect reference sphere and the real wavefront. b) The wavefront deformation leads to displacement of the ray.

direction for the sake of simplicity. The different rays coming from the object point B go through the system's pupil (for a single optical system it is the optics itself) and form afterwards a point in the image plane. The principal ray is the ray from the object going through the center of the pupil. It forms the point B'_p, as illustrated in Figure 2.5. Another ray crosses the pupil at a different position P. The position P is defined by the normalized radius ρ and the angle φ. The position of the object point B is determined by coordinates x and y: $B(0, y)$. In the image plane the coordinates are noted x' and y'. The position of B'_p is $(0, y')$. The image B' of a ray is noted by its deviation from B'_p: $B'(\Delta x', y' + \Delta y')$.

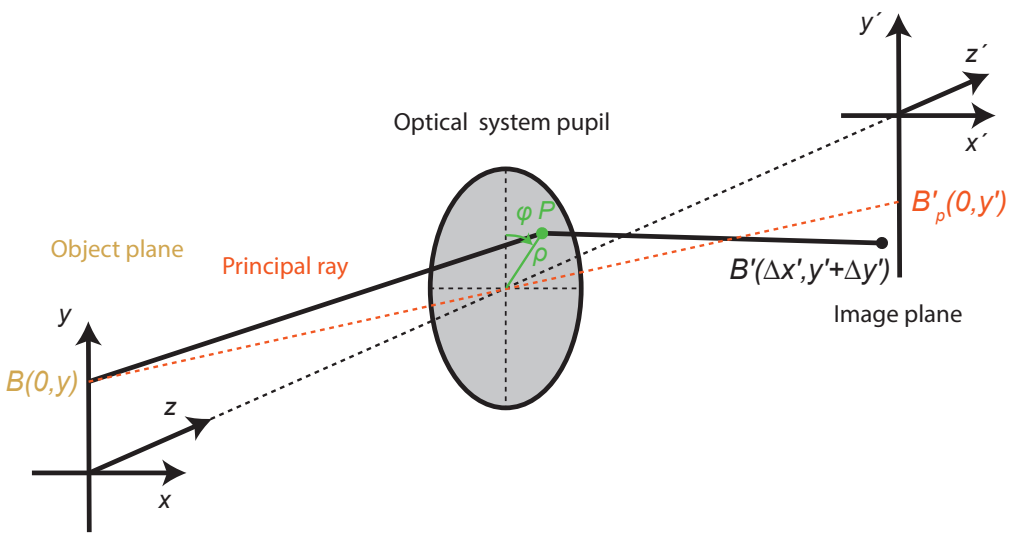

Figure 2.5: Optical system imaging a point B into B'.

We are interested in characterizing the deviation from the perfect imaging. We consider first the wave aberration, i.e., the difference of optical path between the wavefront and the sphere of reference, just after the pupil of the system. For a circular symmetric system, it has been proven that the wave aberration is a function of the field position y, the normalized height on the pupil ρ and the angle on the pupil φ as follows:

$$\Delta W_F(\rho, \varphi, y) = \sum_{p,q,m} a_{pqm} y^p \rho^q \cos(\varphi)^m \tag{2.9}$$

The first few terms of the development are written in Table 2.1, with the corresponding associated aberration. Due to circular symmetry, only the (p+q) even terms are taken into account. The first four terms, i.e. the zeroth and second order term, piston, tilt and defocus, are not strictly considered as aberrations, as they can be eliminated by a change of reference. The last five aberrations in Table 2.1, the fourth order terms, are historically called Seidel aberrations.

Table 2.1: Zeroth, second and fourth order terms of the wave aberration development.

Associated aberration	Coefficient	Field and pupil dependence
Piston	a_{000}	1
Defocus	a_{020}	ρ^2
Tilt	a_{111}	$y\rho\cos\varphi$
Second order piston	a_{200}	y^2
Spherical aberration	a_{040}	ρ^4
Coma	a_{131}	$y\rho^3\cos\varphi$
Astigmatism	a_{222}	$y^2\rho^2\cos^2(\varphi)$
Field curvature	a_{220}	$y^2\rho^2$
Distortion	a_{311}	$y^3\rho\cos\varphi$

Focusing on the wavefront analysis only, independently of the optical system, one can consider y fixed. The resulting aberrations, forming the base of Seidel polynomials, are summarized in Table 2.2.

Table 2.2: Development of the first few terms of the wave aberration on the pupil, omitting the piston terms.

Aberration	Pupil dependence
Defocus	ρ^2
Tilt	$\rho\cos\varphi$
Spherical aberration	ρ^4
Coma	$\rho^3\cos\varphi$
Astigmatism	$\rho^2\cos^2(\varphi)$
Field curvature	ρ^2
Distortion	$\rho\cos\varphi$

Seidel polynomial basis demonstrates the drawback of not being orthogonal. In order to solve this problem, a basis of orthogonal polynomials was developed to describe wavefront

aberrations over a circular pupil: the Zernike polynomials [89]. The wavefront aberration is now expressed as:

$$\Delta WF(\rho, \varphi) = \sum_{m,n} c_{n,m} Z_{n,m}(\rho, \varphi) \tag{2.10}$$

with $Z_{n,m}(\rho, \varphi)$ the Zernike polynomials and $c_{n,m}$ their respective weights. The expression of some of the first normalized Zernike polynomials and the corresponding aberrations are detailed in Table 2.3. They are presented in Figure 2.6. They can be expressed as linear combinations of the Seidel polynomials from Table 2.2.

Table 2.3: Some of the first 9 normalized Zernike polynomials and associated aberrations.

n	m	$Z_{n,m}$	Associated aberration
0	0	1	Piston
1	1	$2\rho\cos(\varphi)$	Tilt at 0°
1	-1	$2\rho\sin(\varphi)$	Tilt at 90°
2	0	$\sqrt{3}(2\rho^2 - 1)$	Defocus (+field curvature)
2	2	$\sqrt{6}\rho^2\cos(2\varphi)$	Astigmatism at 0°
2	-2	$\sqrt{6}\rho^2\sin(2\varphi)$	Astigmatism at 45°
3	1	$\sqrt{8}(3\rho^2 - 2\rho)\cos(\varphi)$	Coma at 0°
3	-1	$\sqrt{8}(3\rho^2 - 2\rho)\sin(\varphi)$	Coma at 90°
4	0	$\sqrt{5}(6\rho^4 - 6\rho^2 + 1)$	Spherical aberration

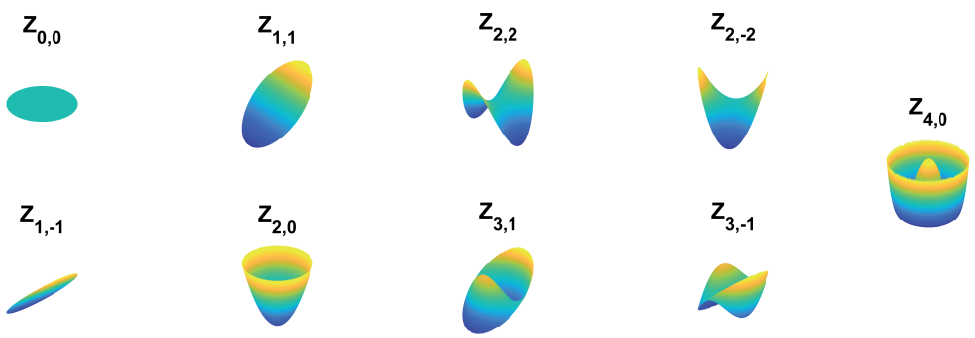

Figure 2.6: Visualization of the first 9 Zernike polynomials detailed in Table 2.3.

This description of the wavefront error offers little sense of what the image spot of the object looks like. The error on the wavefront and the deviation of the image spot are linked through the local slopes of the wavefront, a local angular deviation of the wavefront generates a lateral translation in the image plane. For the five Seidel aberrations, the displacements in image plane $\Delta y'$ and $\Delta x'$, for an object of position $(0, y)$, are given in table 2.4.

Table 2.4: Displacement $\Delta y'$ and $\Delta x'$ of the image caused by the five Seidel aberrations, for an object along the y direction.

	$\Delta y'$	$\Delta x'$
Spherical aberration	$\rho^3 \cos\varphi$	$\rho^3 \sin\varphi$
Coma	$y\rho^2(2+\cos 2\varphi)$	$y\rho^2 \sin 2\varphi$
Astigmatism	$y^2\rho\cos(\varphi)$	0
Field curvature	$y^2\rho\cos\varphi$	$y^2\rho\sin\varphi$
Distortion	y^3	0

The dependence order in ρ and y of the image position is 3, which is why these Seidel aberrations are commonly called *third order aberrations*. It is now possible to visualize the shape of the image spot. We will briefly present the main aberrations we encounter in our optical systems: spherical aberration, astigmatism and coma. When the object position y is fixed, the field curvature cannot be distinguished from the defocus and the distortion from the tilt (see Table 2.2), so we do not present them here.

Spherical aberration The image spot is described by the parametric equations of a circle. The aberration does not involve the height of the object y but the height of the ray in the pupil ρ. This field-independent aberration is called *spherical aberration*. As shown in Figure 2.7 a), the higher the rays, the closer they focus, creating circles on the paraxial imaging plane (black line). This often arises from spherical shapes used for lenses or spherical mirrors. Aspherical lenses can compensate this but they are more difficult to manufacture.

Coma The equation describes a circle that becomes larger as y and ρ increase. This circle also offsets progressively in the y'-direction. This is the coma aberration. Coma arises when an object is off-axis ($y \neq 0$). The principal ray ($\rho = 0$) focuses to the paraxial focus, and the rays coming from further apart (ρ increasing) focus in larger and larger circles which are shifted from the paraxial focus position. This results in the typical comet shape focus, represented in Figure 2.7 b).

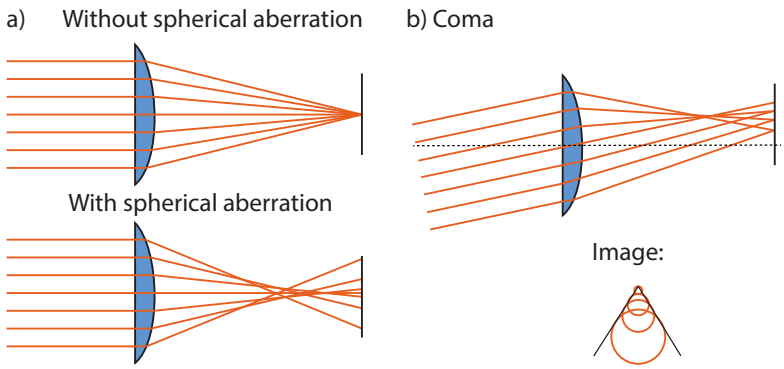

Figure 2.7: a) Spherical aberration b) Coma

Astigmatism For an off-axis point, astigmatism arises when rays in the tangential plane (defined as the one that contains the object and the axis of symmetry) do not focus at the same place as the rays in the sagittal plane (the plane perpendicular to the tangential one containing the object). These two focii, presented in Figure 2.8, are called tangential and sagittal focii; they are a horizontal and vertical line. The distance between these focii is proportional to the strength of the astigmatism.

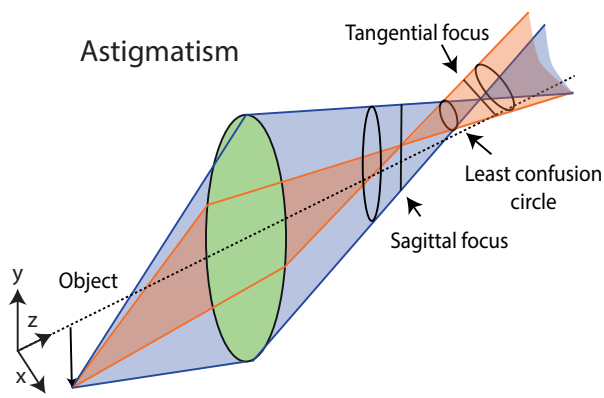

Figure 2.8: Astigmatism

Defocus Although the defocus is not strictly an aberration, it is important to consider. If the image plane is placed after the focus of a perfect beam, the image is "blurry". This is corrected by shifting the imaging plane. For our wavefront measurements, it appears as an extra parabolic phase (curvature) due to wave propagation. Removing this parabolic phase is the first step in the wavefront analysis.

1.3 Wavefront metrology

We here introduce the measurement technique based on a wavefront sensor that we use in Paper IV and V. Complete spatial characterization of an HHG beam requires measurement of both the spatial profile and the spatial phase (or wavefront). The spatial profile can be obtained with a CCD camera, but the phase is more difficult to measure.

Some techniques used for XUV phase measurements are point-diffraction [90], slit diffraction [91] and lateral shearing interferometry (LSI) [92]. They are based on inserting and scanning a component in the beam focus, which is often a drawback, for instance for our experiments where the DVMIS occupies the space in the focal region (see Chapter 1). In addition, these techniques yield only the phase. LSI shows the advantage of being spectrally resolved. A wavefront sensor based on Talbot interferometry was recently used for monitoring x-ray FEL quality [93].

In our experiments we used a Hartmann wavefront sensor [94, 95]. Shack-Hartmann sensors, based on a micro-lens array and a CCD sensor, are routinely used in the visible or near-IR regime, but they are not available in the XUV (see Chapter 3).

Hartmann wavefront sensor The wavefront sensor that was employed for this work is composed of a Hartmann mask and an XUV CCD camera, as illustrated in Figure 2.9 a). The mask is composed of an array of small holes. The beam diffracts from each hole. In the case of a flat and non-tilted wavefront, the diffraction spots on the camera are equally spaced (black dots) and resemble the arrangement of the holes on the mask. If there is a local wavefront deviation, the corresponding spot positions is shifted in proportion to this wavefront deviation (red dots). The positions are calibrated for a well-known wavefront (typically the spherical wavefront created by diffraction onto a pinhole). The local wavefront slopes, $(\partial W/\partial x, \partial W/\partial y)$ with W denoting the wavefront, are proportional to these deviations ($\vec{h}$ in the figure), and are calculated for each hole. The wavefront is then reconstructed over the whole aperture. This sensor permits accurate phase reconstruction, and provides a spatially sampled intensity distribution.

Wavefront reconstruction There are two main types of wavefront reconstruction from the measured slopes [96]. The first one is called zonal reconstruction, which corresponds to direct numerical integration of the local slopes. The other type is modal reconstruction, aiming to decompose the wavefront in the basis of orthogonal polynomials, which correspond to a set of different aberrations. The coefficients are determined by directly fitting the derivatives of the polynomials to the measured local slopes. This permits extraction of the aberrations independently, with the drawback of fitting them over a circular pupil, which does not always match real beam profiles and leads to slightly underestimated aberrations

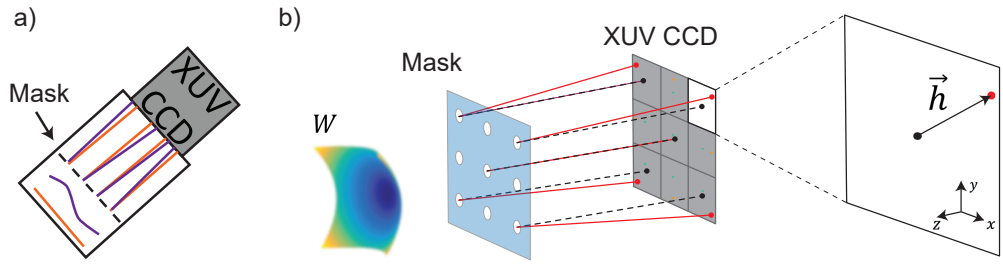

Figure 2.9: Principle of the Hartmann wavefront sensor: a) A flat wavefront (orange) yields an evenly spaced array of points after diffraction from the mask, while a deformed wavefront (purple) locally diffracts to a different position depending on the local deformation. b) The Hartmann vector $\vec{h}$ indicates the direction and magnitude of the displacement of the diffraction pattern, and thus presents a measure of the local wavefront slope at the position of each diffraction hole.

[89]. The basis of orthogonal polynomials is provided by the Zernike polynomials, which are often the preferred choice for extracting and studying aberrations independently.

1.4 Wavefront and aberration transfer from IR to XUV

Because the IR beam creates the XUV beam via the HHG process, it influences the spatial properties of the XUV beam. Understanding the transfer of IR aberrations to the XUV could be a major step toward more control of the spatial quality of XUV beams created by HHG.

The phase of the XUV field can be described, with a simple model, as the sum of q times the phase transferred from the IR (q being the harmonic order) and the dipole phase, which is the phase accumulated by the electron during its trajectory, neglecting here the influence of tunneling and recombination. The XUV phase is written as:

$$\phi_q(x, y, z) = q\phi_{IR} + \phi_{dipole}. \tag{2.11}$$

The spatial transfer of aberrations from the IR to the harmonics can be decomposed into two contributions.

Direct transfer from the IR The first term of Equation 2.11 corresponds to the transfer of the wavefront from the IR to the harmonics and leads to direct transfer of IR aberrations. Since the wavelength of a harmonic is q times smaller, proportionally the deviation from a perfect wavefront, i.e. the aberration, is q times stronger than for the IR: a good quality IR wavefront, for instance $\lambda_{800\text{nm}}/20$ RMS, yields an aberration on the order of $\lambda_{42\text{nm}}/1$ RMS for H19. The HHG process happens only in a small area of the IR beam, where the

intensity is high enough. For instance one can make an approximation $E_{XUV} \propto | E_{IR} |^n$ with $n \sim 4$. The higher the order the smaller the area. Only the aberrations of the beam in the area where the process happens are transmitted, which reduces the effect of this transfer. This small area coincides with the area where the IR focus quality is the best. Furthermore, HHG is usually performed in a focused beam. Local wavefront aberrations correspond to high spatial frequencies, which if one understands focusing as a spatial Fourier transform (within the Fraunhofer approximation), appear outside the main peak. Therefore, the wavefront RMS of a focused beam is usually smaller than in the far field. This can be understood similarly to how a pinhole cleans the spatial profile of a beam. Phase-matching also affect the properties of the XUV beam. Finally, the IR beam may undergo reshaping while propagating in the nonlinear medium, which also affects the spatial properties of the XUV beam.

Influence of the dipole phase variation Assuming that both IR and XUV beam are Gaussian beams and approximating the dipole phase variation as a spherical phase, the curvature of the harmonic beam can be described as the sum of the curvatures from the IR and dipole phase:

$$\frac{1}{R_q} = \frac{1}{R_{IR}} + \frac{1}{R_{dipole}}. \tag{2.12}$$

The dipole phase adds a defocusing curvature, changing the focus size and position of the harmonic beam. As the dipole phase depends on the intensity, one consequence is that the curvatures created in the different planes are not be the same if the IR beam is anisotropic spatially. The harmonic beam has two different focii, leading to astigmatism. This is illustrated in Figure 2.10. The dipole phase depends on the harmonic order, and so does the astigmatism.

The formula for the dipole phase Eq. 1.22 have been derived in Chapter 1. Using Gaussian optics formalism for the intensity, approximating for small quantities $\exp\left(\frac{2(x^2+y^2)}{W(z)^2}\right) = 1 + \frac{2(x^2+y^2)}{W(z)^2}$ and neglecting the terms that do not have a radial dependence, one can rewrite the dipole phase for short trajectories as:

$$\phi_{\text{dipole}}(x, y, z) = \frac{2\gamma^{(s)}(q - q_p)^2\omega^2}{I_0} \frac{(x^2 + y^2)}{W_0^2} \tag{2.13}$$

with I_0 and W_0 the peak intensity and waist of the IR beam. It follows that the dipole

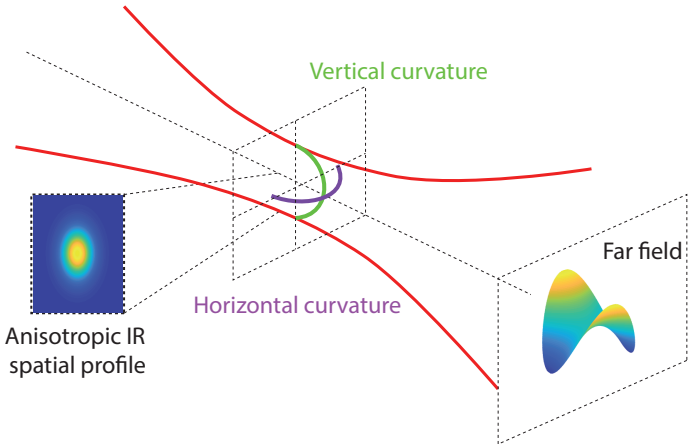

Figure 2.10: If the IR spatial profile is anisotropic, the waist is different in the different directions, so the dipole phase adds a slightly different curvature to the harmonic beam, and the focii are different. In the far field, that can be seen as astigmatism.

phase adds a curvature radius that can be written as:

$$R_{\text{dipole}} = \frac{-qI_0 W_0^2}{4\gamma^{(s)}(q-q_p)^2\omega c} \tag{2.14}$$

It is remarkable that this radius does not depend on the longitudinal position z, so it is the same in the different planes. If the IR beam has different waists $W_{0,x}$ and $W_{0,y}$ in the x and y directions, it follows that there is a difference between the radii $R_{\text{dipole},x}$ and $R_{\text{dipole},y}$, which is a characteristic of astigmatism.

For the typical focusing values in our loose configuration, with $W_0 = 200$ µm and $I_0 = 2\times10^{14}$ W/cm^2, the radius of curvature introduced by the dipole phase is $R_{dipole} = 0.69$ m for H19, and $R_{\text{dipole}} = 0.176$ m for H33. For comparison purpose, the radius of the IR Gaussian beam with these parameters reaches a minimum of 0.31 m at the Rayleigh range. Therefore, the effect from the dipole phase is not negligible and needs to be taken into account.

Conclusion

To conclude, our simple model describes the transfer of aberrations from the IR to the XUV through two processes, the direct transfer from wavefront to wavefront, and the transfer from the IR spatial profile to the XUV wavefront through the dipole phase. It is also clear that the dipole phase has an impact on the XUV beam focus position and size, which will be discussed in the next chapter.

2 Results

2.1 Wavefront measurements

The wavefront sensor from Imagine Optics was used during a series of campaigns in collaboration with the group of Philippe Zeitoun from the Laboratoire d'Optique Appliquée (LOA). The Hartmann mask contains an array of 34 × 34 square holes of side 110 µm, separated by 387 µm. Thanks to the low repetition rate and high flux of the intense XUV beamline, this sensor can record single-shot wavefronts.

It was placed in different positions in order to study aberrations before and after the focusing optics. Position 1 in Figure 2.11 is before the optics, 9.5 meters after the generation plane, in order for the beam to be sufficiently diverged. In position 2, the sensor is placed 60 cm after the XUV focus in the end-station of the beamline. In a third position, referred to as position 3 and not shown in the Figure 2.11, a multilayer mirror placed a few meters behind the generation point was used to select a single harmonic and send it to the wavefront sensor.

The results obtained in positions 1 and 3 are described in Paper VI. The results of the measurements after the focus in position 2 are published in Paper IV and detailed in the next chapter.

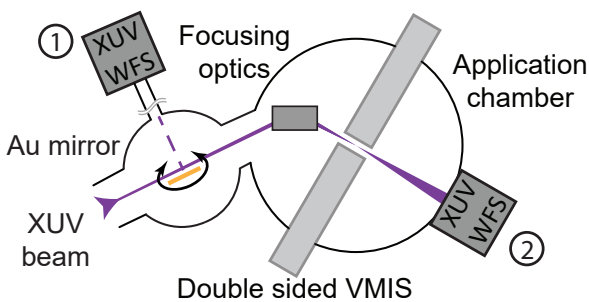

Figure 2.11: Different positions of the wavefront sensor in the intense XUV beamline end-station: before (1) or after (2) the XUV focus.

A typical XUV beam generated in our setup is composed of harmonics between H13 and H27, as shown in Figure 1.13 a). Depending on the generation conditions, it is possible (in our setup and in Argon) to obtain up to H35. A typical XUV beam spatial profile and wavefront measured in position 1 is plotted in Figure 2.12 a) and 2.12 b). The wavefront is plotted in units of λ_{19}, the 19th harmonic dominating at the time of measurement. The beam profile is slightly anisotropic, and the wavefront presents astigmatism at 0°. The RMS of the wavefront is close to $\lambda_{19}/4$, averaged over 5 different single-shot measurements. Figure 2.12 c) is obtained by filtering out the astigmatism contribution to the wavefront. What remains is negligible, proving that astigmatism is the main aberration present in the

XUV beam. Depending on the experimental conditions on different days, we obtained a maximum quality of $\lambda_{19}/9$ RMS. A few graphs showing the evolution of the wavefront RMS as a function of different generation parameters are presented in Paper v.

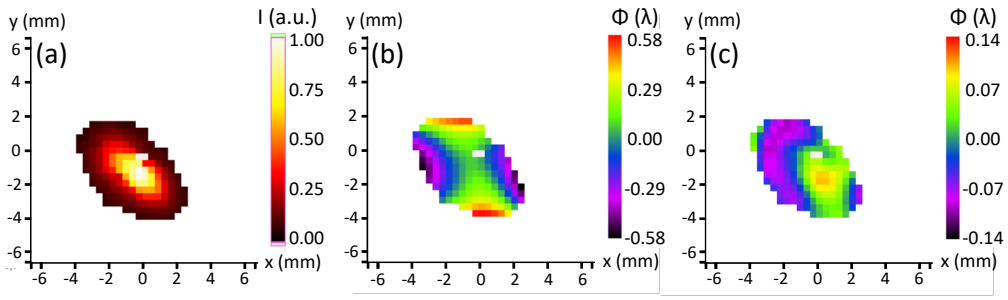

Figure 2.12: The far field XUV beam measured in position 1. a) The spatial profile. b) The wavefront in unit of λ_{19}. c) The residual wavefront with astigmatism removed.

In Figure 2.13 are plotted the spatial profiles and wavefronts of the different harmonic orders taken with spectrally selective multilayers mirrors in position 3: H19 in Figure 2.13 a) and 2.13 d), H23 in Figure 2.13 b) and 2.13 e), and H33 in Figure 2.13 c) and 2.13 f). They are plotted in units of their own wavelength: λ_{19}, λ_{23} and λ_{33}. H19 shows no visible astigmatism and low aberrations, with an RMS of $\lambda_{H19}/16$. H23 shows very low astigmatism, and the RMS of the wavefront is $\lambda_{H23}/12$, while H33 has a strong astigmatism. However, H33 was in the cut-off, and we had to significantly change the generation conditions to obtain enough signal. This strong astigmatism could be due to the sensitivity of the wavefront quality to the generation conditions, or to the fact that the aberration transfer from the IR beam scales with the order as described in Section 1.4.

2.2 Aberration transfer

We investigate here the strength of the different contributions to the phase of the XUV beam, presented in Section 1.4. These results are presented in Paper v. Numerical simulations were performed, using the spatial profile and phase of the IR far field (see Paper v) and propagating it to the near-field, i.e. the proximity of the geometric focus, where the XUV is generated. The generated XUV beam is then propagated to the far field and its aberrations are analyzed. The propagations are done from z' to z using the wave propagator:

$$E_q(x,y,z) = FT^{-1}\left[\tilde{E}_q(k_x,k_y,z')\exp\left(-i(z-z')\sqrt{k^2-k_x^2-k_y^2}\right)\right], \tag{2.15}$$

where $\tilde{E}_q(k_x,k_y,z')$ is the spatial Fourier transform of the harmonic field in the z' plane. Nonlinear medium or phase matching are not taken into account.

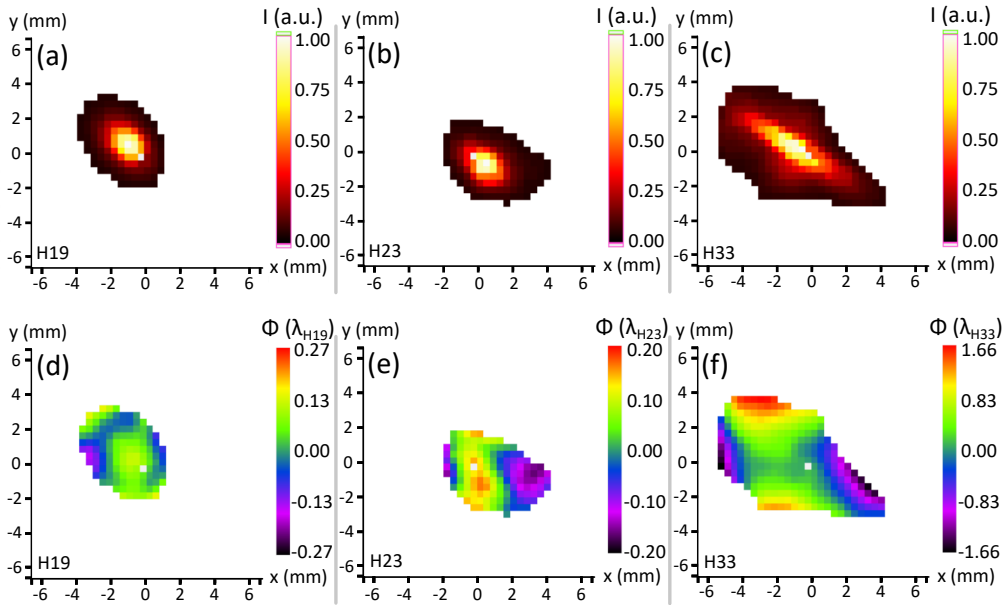

Figure 2.13: Spatial profiles and wavefronts of different individual harmonics H19 (a and d), H23 (b and e) and H33 (c and f).

The XUV spatial profile in the focus was created as $E_{XUV} \propto | E_{IR} |^4$. A mask was applied depending on the intensity, to cut the harmonics after the cut-off. It leads to a different beam size for the different orders. Only the short trajectories were considered as the long ones lead to higher divergence and lower intensity in the far field.

Different sets of parameters were chosen for H19, H23 and H33, as the experimental parameters were changed for H33, which is beyond the cut-off in regular conditions. The generation position was scanned around the focus, and was taken to be 80 mm before the IR focus for H19 and H23, and 130 mm for H33. The peak IR energy was 3×10^{14} W/cm^2 for H19 and H23, and 4×10^{14} W/cm^2 for H33. Both the contribution of the IR transfer and of the dipole phase were taken into account.

The spatial profile and wavefront in the far field of the different harmonics are presented in Figure 2.14: Figure 2.14 a) and 2.14 d) for H19, Figure 2.14 b) and 2.14 e) for H23, Figure 2.14 c) and 2.14 f) for H33. The average defocus curvature is removed from each wavefront. The spatial profiles and wavefronts are displayed with a 5% intensity threshold. The wavefront RMS of H19 is $\lambda_{19}/6$, $\lambda_{23}/7$ for H23 and $\lambda_{33}/8$ for H33. The wavefront RMS is proportionally stronger for H19, however the shape deformation due to astigmatism is clearly visible for H23 and even stronger for H33, confirming the order dependence of the aberration transfer.

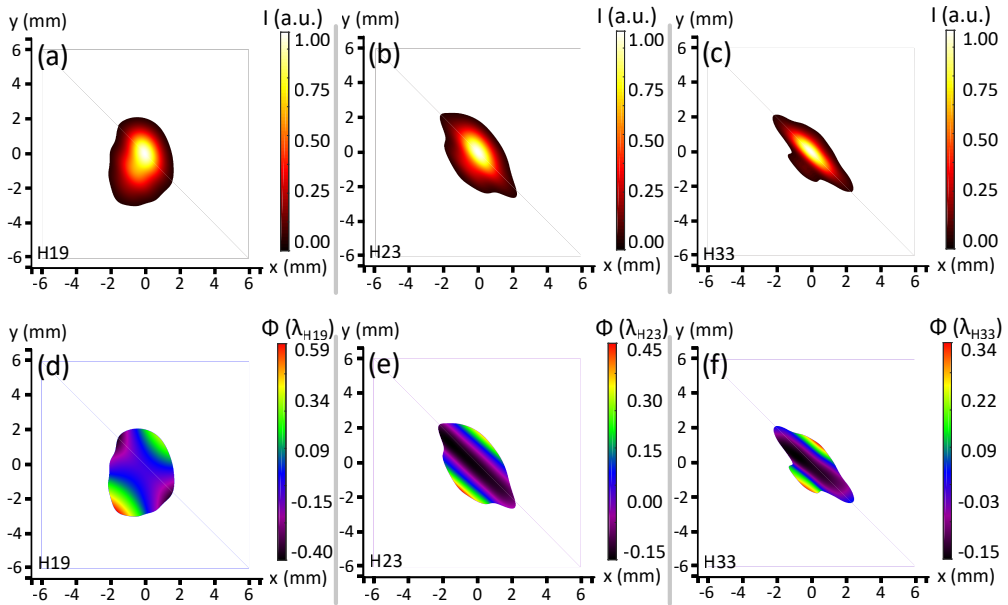

Figure 2.14: Simulated spatial profile and wavefront of the far field harmonics H19 (a and d), H23 (b and e) and H33 (c and f), taking into account the aberration transfer from the back-propagated IR beam and the dipole phase effect. Adapted from Paper v.

It is difficult to extract independently the contributions of the transfer from the IR wavefront and from the IR spatial profile through the dipole phase, as phase and spatial profile are intrinsically linked and evolve upon propagation. For instance, an astigmatic beam has two focii, sagittal and tangential, so the beam shape evolve between an anisotropic beam in one direction, a round beam in between the focii, and an anisotropic beam in the other direction. Meanwhile, the wavefront is composed of two different curvatures in the two sagittal and tangential directions, which evolve strongly upon propagation between the focii. The two types of transfers are thus coupled and the resulting behaviors very complex (see Figure 10 of Paper v).

The difficulty of such analysis is that the properties of the far-field and near-field seem quite different because of diffraction upon propagation. Having only access to the far-field experimentally necessitate to make approximations about what the near-field transfer look like.

These simulations raise however interesting points, confirming the strong influence of the IR beam spatial properties upon the XUV spatial properties through both the spatial profile and the wavefront. Further investigations are planned at the time of writing. Using that knowledge, a possible outlook is to use a deformable mirror to control the XUV spatial properties (see Paper v).

Chapter 3

Focusing high-order harmonics

Our goal is to perform ultrafast nonlinear experiments on atoms and molecules. In order to reach the nonlinear regime, a high intensity on target is needed: more than 10^{12} W/cm^2. High intensity requires both high flux and a small focal spot. We achieve high flux thanks to our loose focusing configuration, as explained in Chapter 1. However obtaining a small focal spot is also challenging. The main reason is that attosecond pulses have short wavelengths, in the XUV regime. XUV is the transition regime between UV and soft X-ray light, and is usually defined as ranging between 10 and 124 eV (corresponding to 124 to 10 nm). It makes the focusing more complex for several reasons. First, XUV radiation is absorbed in every material so only mirrors can be used, limiting the number of available elements. Second, it also requires a grazing incidence in order to have correct reflectivity while conserving bandwidth. It makes the beamline longer but also introduces aberrations. These aberrations can be compensated for by combining several mirrors.

This chapter details the specific challenges of the XUV domain, leading to the different solutions for focusing harmonics beams in grazing incidence. The focusing configuration used in this work is introduced, along with alignment tests to measure wavefront quality. The size of the accessible focal spot is discussed. Finally, the influence of the generation position on the XUV beam focus position, divergence and refocusing is studied.

1 Specificities of XUV optics and focusing

1.1 Introduction to XUV optics

The refractive index has an impact on refraction and reflection in a medium.

Refractive index The index of refraction is defined as the ratio between the speed of light c and the phase velocity v_p of the wave in the medium:

$$\tilde{n} = \frac{c}{v_p} \tag{3.1}$$

It can also be written as the sum of its real and imaginary parts $1 - \delta$ and β:

$$\tilde{n} = 1 - \delta + i\beta \tag{3.2}$$

This notation is commonly used for the XUV regime because the real part of the refractive index in most materials is slightly less than 1 [97].
Considering a wave propagating along z, with wave vector $\tilde{k} = 2\pi\tilde{n}\lambda_0$:

$$\begin{aligned} E(z,t) &= E_0 \exp -i(\omega t - \tilde{k}z) = E_0 \exp\left(-i\left[\omega t - \frac{2\pi z(1-\delta)}{\lambda_0}\right]\right) \exp\left(\frac{-2\pi z\beta}{\lambda_0}\right) \\ E(z,t) &= E_0 \underbrace{\exp\left(-i\left[\omega t - \frac{2\pi z}{\lambda_0}\right]\right)}_{\text{Vacuum propagation}} \underbrace{\exp\left(-i\frac{2\pi z\delta}{\lambda_0}\right)}_{\text{Phase shift}} \underbrace{\exp\left(\frac{-2\pi z\beta}{\lambda_0}\right)}_{\text{Decay}} \end{aligned} \tag{3.3}$$

The imaginary part of the index of refraction β leads to exponential decay while propagating in the material. The penetration depth, after which the intensity is reduced by 1/e, is defined as $\delta_p = \lambda_0 4\pi\beta$. In the XUV regime, β is on the order of 10^{-5} 10^{-6}, giving penetration depth ranging between a few tens of nm to hundreds of μm. The XUV radiation is quickly absorbed in every material, which is why refractive optics such as lenses is not used. In order to focus XUV radiation, one needs refractive or reflective optics such as zone plates or mirrors.

The real part of the refractive index $1 - \delta$ leads to a frequency-dependent phase velocity. Different frequency components travel at different velocities in the medium. This effect is called dispersion. In the XUV regime, the real part of the refractive index is slightly less than 1, and the phase velocity is higher than c.

Total external reflection We consider a wave propagating in a vacuum impinging a medium with an index of refraction $\tilde{n}$ (Eq. 3.1). We consider it to be real for the sake of simplicity: $n = \mathrm{Re}(\tilde{n}) = 1 - \delta$ with $\delta \ll 1$. The angle of incidence is noted as ϕ, while the transmitted angle is ϕ' and the reflected angle is ϕ'', as in Figure 3.1. $\phi'' = \phi$ by law of reflection, and $\sin(\phi') = \sin(\phi)/n$ by Snell's law. When ϕ approaches $\pi/2$, ϕ' approaches it faster. At the limit, the critical angle of incidence is defined for: $\sin\phi_c = 1 - \delta$. For $\phi \geq \phi_c$, the wave is reflected instead of transmitted. By analogy with total internal reflection, where the light is reflected instead of refracting in a medium with higher n, such as

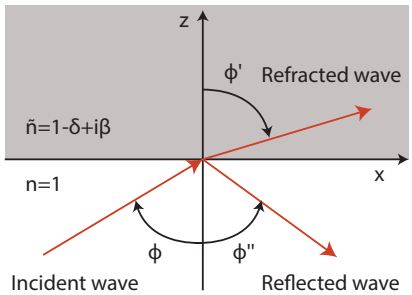

Figure 3.1: An electromagnetic wave impinging with an incidence angle ϕ on an interface between vacuum and a medium, experiencing reflection at an angle ϕ'' and refraction at an angle ϕ'.

water or optical fibers, this phenomena is called total external reflection. Because $\delta \ll 1$, it happens only close to a 90° incidence angle. The grazing angle is $\theta = 90° - \phi$.

Fresnel equations Reflection and refraction at an interface are governed by the Fresnel equations. Considering only s-polarization as used in the present work and with the same notations as Figure 3.1, the reflectivity coefficient can be expressed as:

$$R_s = \frac{|\cos\phi - \sqrt{\tilde{n}^2 - \sin^2\phi}|^2}{|\cos\phi + \sqrt{\tilde{n}^2 - \sin^2\phi}|^2} \tag{3.4}$$

In the case of normal incidence, this yields

$$R_{s,\perp} \simeq \frac{\delta^2 + \beta^2}{4} \tag{3.5}$$

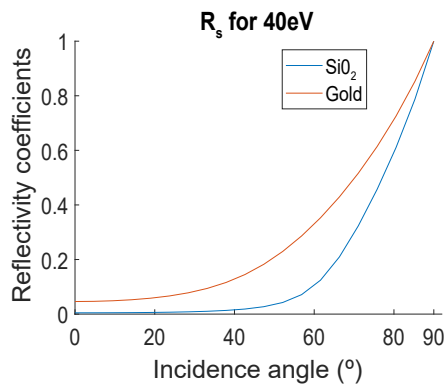

Figure 3.2: Reflectivity coefficients for $Si0_2$ and gold as a function of the incidence angle.

Because δ and β are very small, one can conclude that the reflectivity coefficient at normal incidence for XUV radiation is very weak. Increasing the incidence angle increases the reflectivity, as shown in Figure 3.2 for fused silica (Sio_2) and gold. For this reason, XUV optics is often used at grazing incidence.

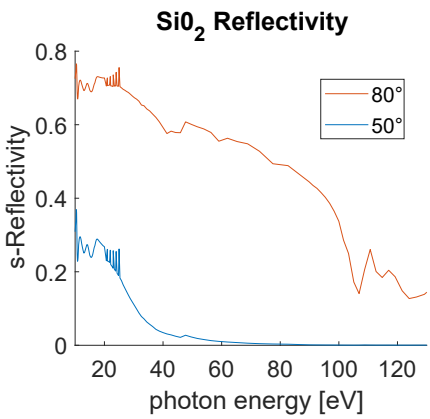

Figure 3.3: Reflectivity coefficients for $Si0_2$ at a 50° and 80° incidence angle as a function of the photon energy.

Influence of wavelength Since the index of refraction depends on the wavelength, so do thus the reflectivity coefficients. Resonances aside, the reflectivity coefficients of all materials are smaller for shorter wavelengths, which implies that a smaller grazing angle is required to reflect shorter wavelengths with the same reflectivity. In Figure 3.3 the reflectivity of Sio_2 in function of the photon energy is plotted for two different incident angles: 50° and 80°. As seen previously, reflectivity is smaller for 50° than for 80° and the reflectivity drop as a function of photon energy occurs earlier at 50° than at 80°. This, it is important to consider this aspect when focusing high-order harmonics, as they are by nature very broadband.

Multilayer mirrors We have shown before that grazing incidence is better for XUV optics, but normal incidence is often preferred for many reasons: the optics are smaller and so less expensive, the collecting angle is larger, aberrations are lower, and the length of the optical system is shorter.

In order to operate in normal incidence, multilayer mirrors were developed to increase the reflectivity. They consist of a superposition of many thin layers of different materials. The result is an interference process between the waves reflected from the different layers, with constructive interference according to the Bragg condition: $\lambda = 2d\sin\phi$ with d the layer thickness. High reflectivities can be achieved, but only for a narrow bandwidth as the interference depends on wavelength. One way to overcome this is to use aperiodic mirrors, which have a broader bandwidth but unfortunately very low reflectivity [98, 99].

In order to preserve both flux and broad bandwidth, we opted for grazing incidence metallic mirrors [100]. The grazing incidence leads us to carefully investigate the optical system aberrations.

1.2 Focusing with grazing incidence optics

Spherical mirror From pure geometrical considerations, very strong astigmatism arises when a spherical mirror is used in grazing incidence, as shown in Figure 3.4.
From the Fermat principle it can be derived [101] that for grazing angle θ, the focal lengths

in the sagittal and tangential planes f_S and f_T of a spherical mirror of radius R are:

$$f_T = \frac{R \sin\theta}{2}$$
$$f_S = \frac{R}{2 \sin\theta} \tag{3.6}$$

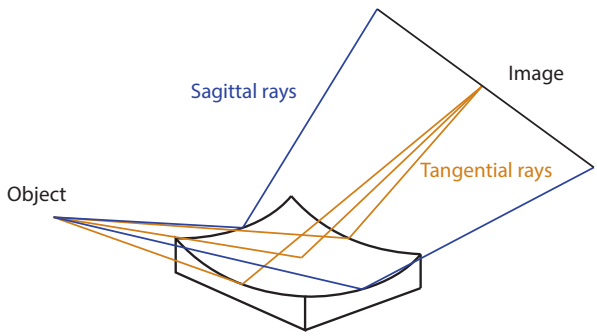

Figure 3.4: Spherical mirror grazing incidence focusing

For a grazing angle $\theta = 10°$ and a radius $R = 1$ m, $f_T = 8.7$ cm and $f_S = 2.9$ m. A spherical mirror always focuses strongly in the tangential plane and weakly in the sagittal plane so is not suitable for focusing.

Toroidal mirror One way to overcome this limitation is to create a mirror with two different curvatures in the different planes. Eq. 3.6 becomes:

$$f_T = \frac{R_T sin\theta}{2}$$
$$f_S = \frac{R_S}{2 sin\theta} \tag{3.7}$$

This way, the curvatures R_T and R_S can be adjusted separately to make the focii coincide.This is called a toroidal mirror and is depicted in Figure 3.5. The aberrations are minimized in a $2f-2f$ configuration, so toroidal mirrors are often used in HHG beamlines to refocus harmonics. The drawback is that the demagnification is only 1 so it is not suitable for microfocusing. Apart from this special configuration, coma aberration dominates and quickly reduces the focusing quality. It is more complicated to manufacture than a spherical mirror and consequently more expensive, and it works only for the angle of incidence for which it is designed.

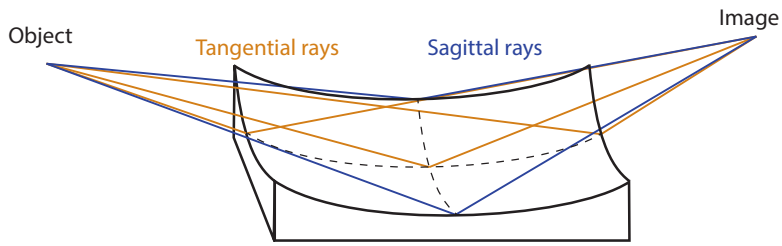

Figure 3.5: Toroidal mirror grazing incidence focusing

Ellipsoidal mirrors In principle, ellipsoidal mirrors permit almost perfect focusing if the source is placed in one of the focii of the ellipse and it is not too extended. It is, however, very sensitive to alignment [102] and to the quality of the surface. Ellipsoidal mirrors are very difficult to manufacture especially for XUV wavelengths and thus expensive. An ellipsoidal mirror was used to focus harmonics between 24 and 38 nm (33 to 51 eV) with a focal spot measured to be 2.5 µm FWHM [103].

In order to compensate for the limitations of focusing with a single mirror, combinations of mirrors can be used.

Kirkpatrick-Baez optics The limitation of spherical mirrors can be overcome by using two of them perpendicular to each other. One mirror focuses in the vertical plane and the other one in the horizontal plane. The radii and distance are adjusted to make the focii coincide. This was used by Kirkpatrick and Baez to create the first X-ray microscope [104]. Kirkpatrick-Baez optics are widely used in the X-ray domain [105], allowing for sub-micrometer focal spots [106, 107].

Combinations of toroidal mirrors Another way to achieve the microfocusing is to use a combination of toroidal mirrors, allowing to compensate for coma aberration. A Z-shaped configuration with two toroidal mirrors was used to focus high-order harmonics between 30 and 70 nm (17 to 38 eV) to an 8 µm FWHM spot [108].

Wolter optics In the 1950s, Wolter [109] demonstrated that some combinations of two confocal conic sections, such as ellipsoid, paraboloid, and hyperboloid, can minimize aberrations. This idea is widely used in astronomy for X-ray telescopes [110], focusing neutron beams [111, 112], and inertial confinement fusion imaging experiments [113, 114]. An even more advanced solution that combines two hyperbolic and two elliptic mirrors have been proposed [115]. Because the toroidal surface is a local approximation of the ellipsoidal sur-

face, this concept can be applied to toroidal mirrors. In this work and Papers II, III, IV, we used a combination of two toroidal mirrors in a Wolter-like configuration.

2 Harmonic focusing with Wolter-like optics

A drawing of the combination of two mirrors used in this work is shown in Figure 3.6. The grazing angle is 15°. The curvatures and focal lengths of the individual mirrors and the assembly are presented in Table 3.1. The combined focal length from the center of the second mirror is 16.5 cm. The HHG source, located 6 meters from the optical system, is imaged 17 cm after the center of the second mirror. The demagnification is 35. The mirrors were installed in a mechanical assembly and pre-aligned by the manufacturer. The assembly is mounted on a 5-axis stage: two goniometers, one rotation stage, and two linear stages. This provides enough degree of freedom to align the assembly. The actuators are piezo-driven, stick-and-slip positioners in an open-loop configuration.

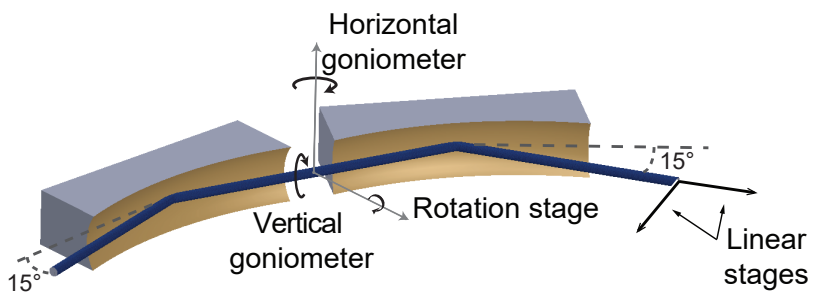

Figure 3.6: Focusing optics of our beamline: two toroidal mirrors in a Wolter-like configuration, assembled in a mount with a rotation stage, two goniometers and two linear translation stages.

Table 3.1: Radii of curvature (provided by the manufacturer) and focal lengths of the individual mirrors in the two planes and the equivalent focal length of the assembly.

	Tangential		Sagittal	
	R_T [mm]	f_T [mm]	R_S [mm]	f_S [mm]
First mirror	2050	265.3	137.2	265.0
Second mirror	4213	545.2	281.8	544.4
Combined	Focal length = 164.2 mm			

The alignment of the Wolter-like optics is crucial to achieve a small focal spot and therefore high intensity on target. We present here different alignment methods.

2.1 Direct measurement of the focal spot

An XUV microscope was developed to measure the XUV focal spot distribution directly. A Ce:YAG scintillation crystal is placed in the focus of the XUV beam. Green photons are emitted, pass through a window and are collected with a long working-distance optical microscope that is not in a vacuum. Relay-imaging lenses bring the light to a high-sensitivity CCD camera. This system was used first in Paper II to assess focal spot size, which was found to be 11×16 µm, significantly higher than the expected values of 4.2×4.5 µm (see Section 2.4). That was due to long integration time (300 shots), so the pointing instabilities tend to broaden the recorded spot. For Paper IV, single-shot characterization was subsequently performed but still led to overestimated values of the focal spot (9×9 µm). The setup did not permit reliable calibration of the microscope as the window separating the optical system from vacuum introduces spherical aberration. Moreover, saturation and quenching effects in the crystal require low XUV flux, which leads to even fewer photons, and challenges the limits of the camera. Finally, this device is not compatible with running experiments and day-to-day alignment, as the tube holder crosses the particle detectors in the interaction region. However it was useful for a first coarse alignment, as the elongated beam shape typical from astigmatism could be observed. It was also used to test and calibrate the split-and-delay unit.

2.2 Alignment with particles detectors

When the optical system is aligned, the focal spot is the smallest, so the beam intensity is the highest. For that reason, an indirect method to align the system is to rotate the actuators to optimize nonlinear signal yield in the detectors in the application chamber. The precision is however limited.

2.3 Alignment with wavefront sensor

During the wavefront campaigns described previously we took the opportunity to use the wavefront sensor for the alignment of the optics. This proved to be very precise and reliable, and became the preferred alignment technique. In order to build our own wavefront sensor, a mask and software were designed and implemented in the beamline.

We now describe the results obtained during the campaign, which are published in Paper IV. We scanned the different actuators while recording the wavefronts. After removing the tilts and defocus, we extracted the aberrations RMS σ with zonal reconstruction. The Strehl ratio S is a good indicator of beam quality. It is defined as the ratio of the peak intensities of focal distribution in the aberrated and unaberrated cases. A good approximation is given by $S = \exp(-\sigma^2/\lambda^2)$ [116]. The RMS and Strehl ratio are plotted in Figure 3.7 as a

function of the number of steps. The wavefronts were measured single-shot, and the values are averaged over 5 measurements. A sharp V-trend is clearly visible for each actuator and the minimum value for a) is $\lambda/36$, meaning that achieving perfect focusing is possible when optimizing the alignment of the actuators.

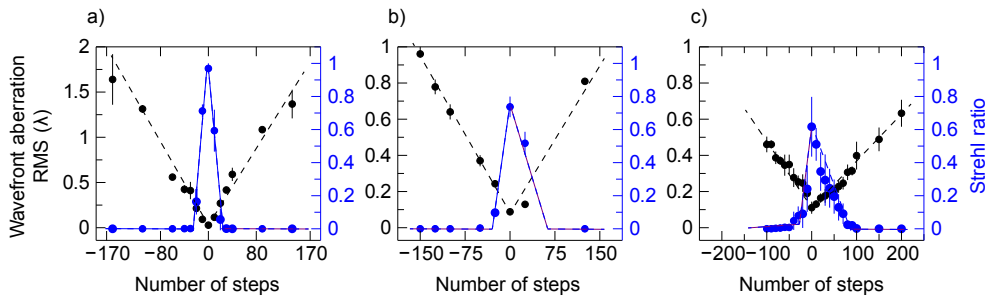

Figure 3.7: Evolution of the XUV wavefront RMS as a function of the focusing optics relative angle (number of steps) along the different axes: a) rotation stage, b) horizontal goniometer and c) vertical goniometer. The RMS is plotted in black dots in units of lambda for $\lambda = 42$ nm (left axis), with error bars coming from several single-shot measurements. The corresponding Strehl ratios are plotted in blue dots (right axis). The qualitative trends are plotted in dashed lines.

In order to determine which aberrations contribute most to the RMS, we used modal reconstruction to extract the different Zernike coefficients. Astigmatism was shown to be the dominant aberration, accounting for most of the deviation from a perfect wavefront. In Figure 3.8 are plotted the evolution of the relative Zernike coefficients for astigmatism 0° (green dots) and 45° (red dots) and coma (white dots). We note that the coma is always completely compensated, which validates the Wolter-like configuration. It is also interesting to note that astigmatism at 0° is introduced only by the horizontal goniometer, while the two other actuators only introduce astigmatism at 45°. This decoupling is useful for in-line alignment.

Ray-tracing simulations with FRED software were preformed to validate this behavior, for harmonic 19. The relative Zernike coefficients are plotted in Figure 3.8 in solid lines as a function of the angle: green for 0° astigmatism, red for 45° astigmatism and black for coma. The values for the three graphs were normalized using the $-0.8°$ point as a reference for the rotation stage. With a zonal method to extract the wavefront RMS, we were able to use the very good agreement to estimate the step size as a function of the relative angle for each actuator.

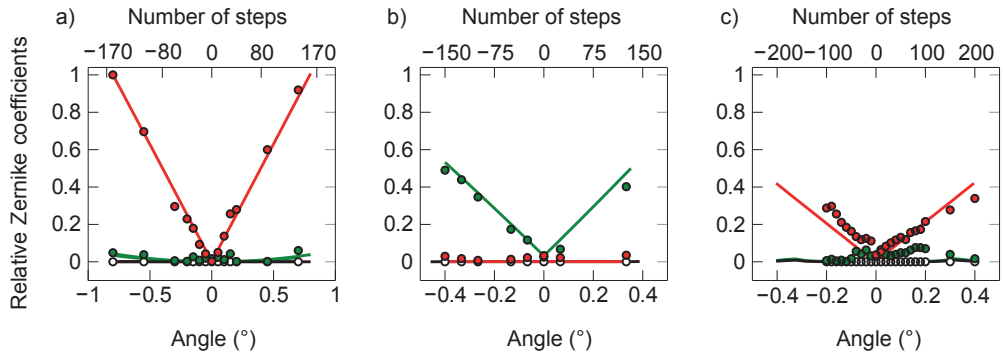

Figure 3.8: Relative Zernike coefficients for the main aberrations as a function of the angle of the a) rotation stage, b) horizontal goniometer and c) vertical goniometer. The experimental data are represented as circled colored dots, plotted as a function of the number of steps (top axis). The ray-tracing simulation data are represented as solid lines, plotted as a function of the angle in degrees (bottom axis). Red corresponds to 45° astigmatism, green to 0° astigmatism, and white/black to the coma.

The beam before the focusing optics often presents some astigmatism, as shown in Chapter 2, which can be compensated for. In Figure 3.9 a) and 3.9 c), the intensity and wavefront of the beam before focusing are shown. The beam presents some 0° astigmatism and has an RMS value of $\lambda/9$. The beam after focusing is shown in 3.9 b) and 3.9 d); the RMS is $\lambda/36$ which corresponds to perfect quality. Our focusing optics do not introduce further aberrations and can even compensate for the pre-existing ones.

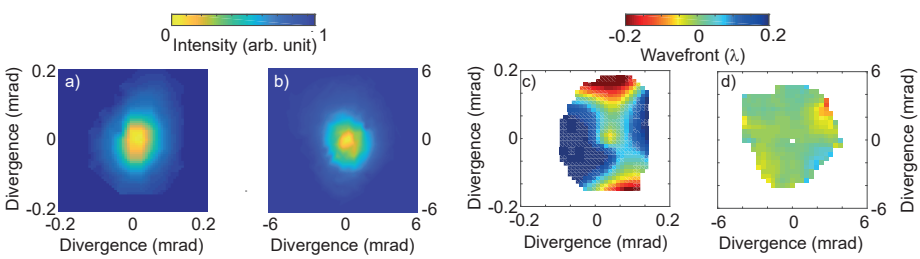

Figure 3.9: Intensity and wavefront of the XUV beam before [a) and c)] and after [b) and d)] focusing.

2.4 Focal spot

One crucial factor for our experiments is the intensity on target. It requires a small focal spot. The best wavefront, the one from Figure 3.9 b) and 3.9 d), was back-propagated to the focus. This calculated focal spot is shown in Figure 3.10 a), with the corresponding profiles along the x and y axes. The FWHM size is 3.6×4.0 µm^2. The ray-tracing simulations, assuming a perfect Gaussian beam and using the experimentally measured divergence, led to a focal spot of 3.0×3.2 µm^2, as shown in Figure 3.10 b). Agreement is quite good; the

20% difference in size can be explained by the estimations made on the divergence and by distortions of the spatial profile.

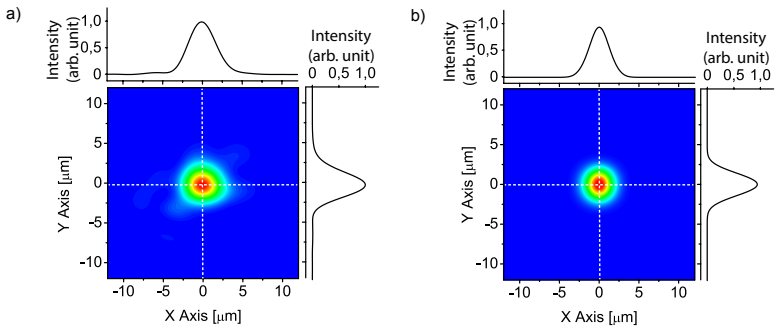

Figure 3.10: Focal spot calculated from a) wavefront measurement by back-propagation, b) ray-tracing simulations.

With focal size calculated from back-propagation and typical energy measured in the interaction region of 5 nJ, we estimated the intensity of the focused attosecond pulse at 7×10^{12} W/cm^2, which is satisfactory for nonlinear experiments.

The limitation of the wavefront sensor is that it does not discriminate between the different wavelengths. What is measured is the weighted average of the diffraction patterns of the different harmonics. We cannot access the focus of each harmonic independently. The calculations are based on H19, the most intense harmonic.

2.5 Refocusing of the harmonics

We here discuss the influence of the dipole phase curvature on the harmonic focus position, divergence and refocusing. This model and its implications are presented in more details in Paper VI.

Effect of the dipole phase on divergence and focus position

The dipole phase adds a positive curvature (defocus) to the generated XUV beam. The curvatures induced by the IR field and that due to the dipole phase variation add or compensate for each other depending on the position of the generation position relative to the IR beam focus:

1. If the generation plane is after the focus, both curvatures have the same sign. The harmonic beam is divergent, and the focus is virtual and is located before the generation generation position.

2. If the generation position is before the focus, several cases are possible. The waist size (and therefore divergence) of the XUV beam strongly depends on the generation position and relative strength of the curvatures.

   (a) If the defocusing curvature introduced by the dipole phase is stronger than that due to the IR beam, the focus of the XUV beam is virtual, before the generation position (3.11 a)).

   (b) In the opposite case, the harmonics are generated as a convergent beam, as illustrated in Figure 3.11 b). In this drawing the beam has the same divergence than in a) but it could also be different.

   (c) If the defocusing curvature introduced by the dipole phase is on the order of the IR curvature they are compensating each other, the divergence of the beam becomes small and around this point the focus position experience a fast variation between virtual and real position, see Figure 3.11 c).

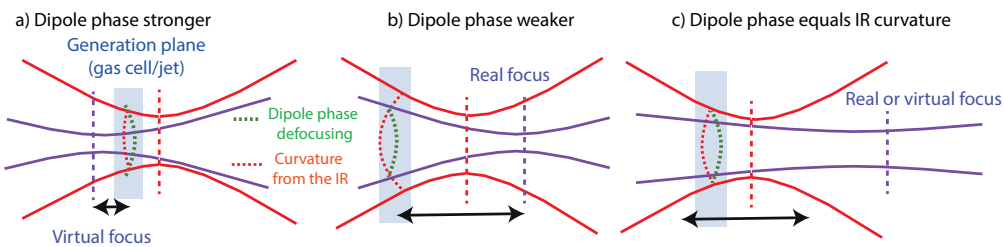

Figure 3.11: For a configuration with the generation plane placed before the IR focus, several cases are possible. a) When the curvature due to the dipole phase is larger than the curvature transferred from the IR, the focus is virtual and before the generation plane. b) In the opposite case, the focus is real and after the generation plane. c) When the curvature from the dipole phase and the IR compensate each other, the waist is bigger and the divergence reaches a minimum. The focus can be real or virtual around this point.

Analytical model

Figure 3.12 presents the predictions of the model in Paper VI for estimating the focus position as a function of generation position, between $-2z_R$ and $+1z_R$.

It is clear from the figure that all the harmonics focii are virtual and located close to each other if the generation position is after the IR focus. In that case, both curvatures from the IR and the dipole phase diverge, so there is no significant impact on the focus position. However, when the generation plane is before the focus, strong variations are visible, depending on the relative strengths of the IR and dipole phase curvature. For example, at $-z_R$, the difference between low order and high order harmonics reaches $5z_R$ i.e. 2.5 meters in our experimental conditions, which is a significant difference. This effect from the dipole phase therefore needs to be taken into account.

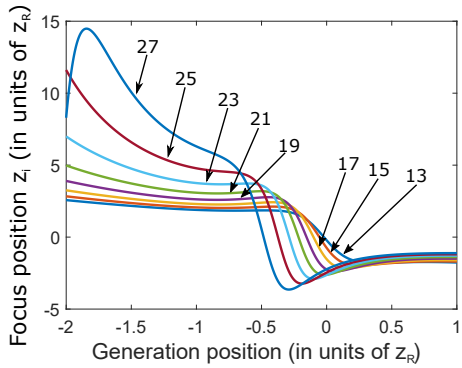

Figure 3.12: Simulations based on the simple Gaussian optics model, showing the focus position of different harmonics depending on the generation position.

Experimental results

The waists of the harmonics in the far field in the XUV spectrometer have been measured for different generation positions in the proximity of the IR focus. The focus position was scanned changing the deformable mirror curvature over the range where the harmonics were efficiently generated. The theoretical waists were determined from the Gaussian optics model: estimating the distance from the XUV focus to the spectrometer for each harmonic, and multiplying it by the divergence. The experimental waists are compared to the theoretical ones in Figure 3.13. The trends are well reproduced. For the two highest orders, H25 and H27, sharp variations deviating from the theory are observed at the extreme positions. For these positions, the intensity being lower, the highest harmonics enter the cut-off where this model does not apply anymore. Others effects, such as propagation in the medium (reshaping, plasma defocusing...) and deviation from Gaussian optics, are not taken into account in the model.

Effect on the refocusing

The longitudinal magnification is the square of the lateral magnification. Upon refocusing by the optics, the $5z_R$ (2.5 m) difference of the focus positions of the different harmonic orders is divided by 35^2, which becomes 2 mm. Using Eq. 2.6 and considering a beam waist of $W_0 = 3.4$ µm (corresponding to 4 µm FWHM), the Rayleigh range of the 19th harmonic can be estimated to 0.9 mm, twice smaller than the maximum difference between the focii. The result is that the plateau and higher order harmonics can be refocused in different positions. Such chromatic aberration is inadequate for broadband applications such as time-resolved experiments. The ability to isolate some specific orders through refocusing could be of interest for other applications.

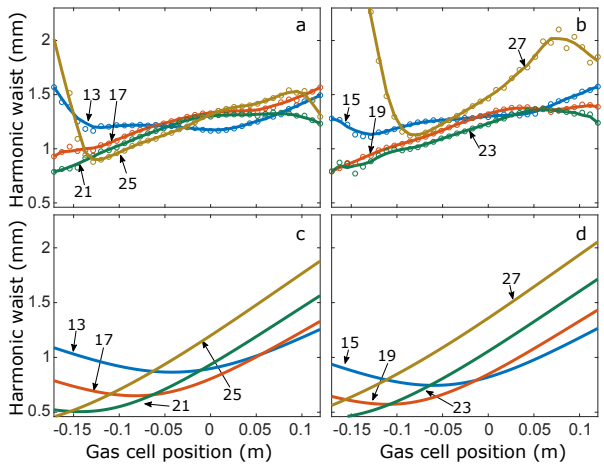

Figure 3.13: Measured waist sizes of the harmonics (top) compared with those estimated using the Gaussian model (bottom). Reproduced from Paper VI.

Calculations based on tabulated TDSE results through a few centimeters of medium have been performed and show very good agreement with the simple Gaussian optics model. The coupling between spatial and spectral properties of harmonics could have an impact for broadband pulses, creating spatio-temporal couplings (see Paper VI).

To conclude, these differences in focus positions may potentially prevent performance of the nonlinear experiments described in Chapter 4. This effect could be used to isolate a specific order, or to achieve direct focusing of HHG without optics. It points out the importance of better spatial control of the harmonics.

Chapter 4

Temporal metrology of attosecond pulses

Our goal is to perform time resolved pump-probe experiments with attosecond pulses on atoms and molecules. In a pump-probe experiment, a pulse is used to trigger a reaction; and after a certain delay, another pulse is used to probe the system [117]. In our context this involves using ultrashort pulses with varying delays in an atomic or molecular gas jet and observing the spectral behavior and momenta of the reaction products, such as photo-electrons and photo-ions. Time-resolved experiments have been performed with attosecond pulses [11, 36, 37, 118–123] or Free-Electron-Lasers (FEL) [20–22], unraveling ultrafast dynamics in atoms and molecules.

A step prior to time-resolved experiments is characterization of the pulses being used. It is essential to have information about the pulses; if possible both the spectral phase and amplitude and the temporal phase and amplitude. In order to characterize pulses, one would ideally use a detector with a response time shorter than the pulse; for instance a nanosecond pulse can be measured with a fast photodiode. However, as the fastest electronic detectors have a response time on the order of picoseconds, no such detector is available for ultrashort femtosecond or attosecond pulses. One can use another ultrashort pulse. The pulse itself is often used as a reference: this is called a self-referencing technique. The simplest one is autocorrelation: the pulse is duplicated, and one of the replicas is temporally delayed. The interaction between the two, for instance in a Michelson interferometer or focused in a nonlinear crystal for femtosecond pulses, provides spectral or temporal information. This chapter details how this is performed and what information is accessible.

However, autocorrelation alone does not allow for full characterization of the pulse. Other techniques have been developed for that purpose. For instance, Frequency Resolved Op-

tical Gating (FROG) [124, 125] and Spectral Phase Interferometry for Direct Electric-field Reconstruction (SPIDER) [126] are two self-referencing techniques that are widely used to characterize completely femtosecond IR or visible pulses. FROG is based on spectrally resolved autocorrelation. The pulse and its delayed replica, acting as a *gate*, are focused in a nonlinear second harmonic (SHG) crystal, as for autocorrelation, and the resulting spectrum is recorded as a function of the delay. SPIDER is based on spectral shearing interferometry: in one arm, the pulse is duplicated and the two replicas are delayed from each other. In the other arm, the pulse is spectrally chirped and stretched. The pulses in the two arms are focused in a SHG crystal. The two replicas will thus interfere with a different part of the spectrum of the stretched pulse. This results in two spectrally shifted pulses, which interfere in a spectrometer. This allows for the determination of the spectral phase.

Direct transposition of the these techniques to attosecond pulses is generally not possible, due to technical constraints. As discussed in Chapter 3, attosecond pulses, which are in the XUV range, are strongly absorbed in every material, so use of nonlinear crystal is not an option. Ionization of atoms in gas phase is used instead. Autocorrelations with attosecond pulse trains [33, 127–129] or isolated attosecond pulses [122, 123] have been performed, paving the way for XUV FROG [130, 131]. Other techniques, that use an ultrashort IR field, have been developed. The most widely used is Reconstruction of Attosecond Beating By Interference of Two-photon Transitions (RABBIT) technique [71, 132, 133]. It relies on analysis of the interferences between electron wavepackets created by absorption of different harmonics and absorption of a photon from the fundamental IR field. Another way to extract information by using the electron wavepacket generated by the attosecond pulse is the streaking technique [13, 38, 134, 135]. The IR field acts as ultrafast phase modulation to the electron wavepacket, like a gate, similar to FROG. When the FROG algorithm is used in combination with streaking it becomes Frequency-Resolved Optical Gating for Complete Reconstruction of Attosecond Bursts (FROG-CRAB) [40, 136, 137] and is often used for the characterization of isolated attosecond pulses.

This chapter presents the concept of autocorrelation and its implementation in the intense XUV beamline using a split-and-delay unit (see Paper VII). Finally the initial steps toward time-resolved experiments is described.

1 Principle of autocorrelation

1.1 Temporal and spectral description of a pulse

A laser pulse that propagates along z can be written as the product of a spatial profile $U(x, y)$ and a temporal field $E(t)$. This temporal field can be expressed with time-dependent real field envelope $\varepsilon(t)$, carrier frequency ω_0, and time-dependent phase $\varphi(t)$. $\widetilde{\mathcal{E}}(t)$ is the

complex field envelope.

$$E(t) = \varepsilon(t)\exp(i\omega_0 t - i\varphi(t)) = \widetilde{\mathcal{E}}(t)\exp(i\omega_0 t). \tag{4.1}$$

The instantaneous frequency ω is linked to the derivative of the phase φ. A constant phase means that there is no frequency variation in time.

$$\omega(t) = \omega_0 - \frac{d\varphi}{dt}. \tag{4.2}$$

In the frequency domain, the pulse can be written with spectral envelope $\widetilde{\mathcal{E}}(\omega)$ (linked to the spectral intensity, in other words to the *spectrum*) and the spectral phase $\widetilde{\varphi}(\omega)$.

$$\widetilde{E}(\omega) = \widetilde{\mathcal{E}}(\omega)\exp(i\varphi(\omega)). \tag{4.3}$$

Knowledge of the intensity and the phase either in the temporal or spectral domain, in addition to carrier frequency ω_0, fully determines the pulse in the other domain. The aim of characterization techniques is to extract as much relevant information about the temporal/spectral waveform as possible.

1.2 Field autocorrelation

Field autocorrelation is the most basic autocorrelation, and is also referred to as *first order* autocorrelation. It is defined, with τ the relative delay between pulses, by:

$$G_1(\tau) = \int_{-\infty}^{\infty} \tilde{\mathcal{E}}(t)\tilde{\mathcal{E}}^{\star}(t-\tau)e^{i\omega_0\tau}dt + c.c. \tag{4.4}$$

Experimentally, this autocorrelation can be achieved with a Michelson interferometer, as shown in Figure 4.1. The incident field is split into two parts, one of them is delayed and they are recombined with another beam splitter. The signal on a photodiode at the output is the intensity of the sum of the two pulses $E(t)$ and $E(t-\tau)$, G_1 being the cross term:

$$I_M(\tau) = \int_{-\infty}^{\infty} |E(t) + E(t-\tau)|^2 dt = 2I + 2Re\{G_1(\tau)\} \tag{4.5}$$

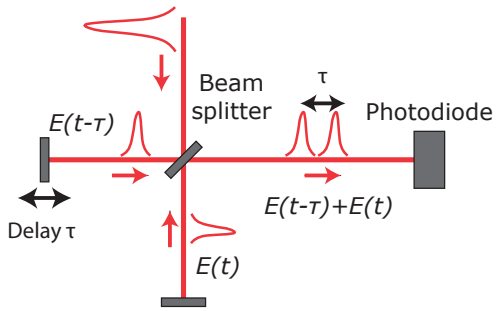

Figure 4.1: Field autocorrelation setup, based on a Michelson interferometer.

The Fourier transform of the field autocorrelation is the spectrum of $\mathcal{E}(t)$ [138]. Field autocorrelation allows retrieval of the spectrum of the pulse, but not the spectral phase. An example of field autocorrelation for a 25 fs pulse is presented in Figure 4.2.

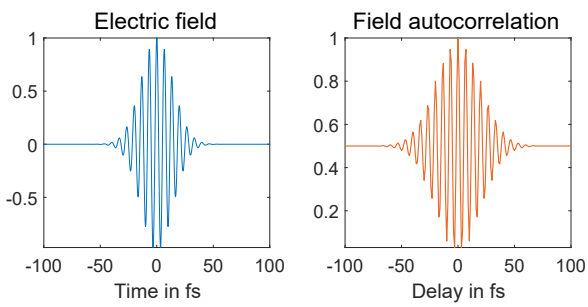

Figure 4.2: Pulse field and its field autocorrelation

1.3 Intensity autocorrelation

Intensity autocorrelation is autocorrelation of the intensity $I(t) = |E(t)|^2$, i.e.

$$G_I(\tau) = \int I(t)I(t-\tau)dt \tag{4.6}$$

Figure 4.3 shows a typical setup for intensity autocorrelation. The pulse is split into two parts with a beamsplitter and the two replicas $E(t-\tau)$ and $E(t)$ are separated. They are focused with a lens in a *non-collinear geometry*. A second harmonic crystal is placed in the focus. The second harmonic field is generated in the direction between the two fundamental beams. It is thus spatially separated from the two beams. The intensity of the SH signal is detected with a photodiode, yielding G_I.

This technique offers the advantage of being background-free, as only the signal in the collinear direction is detected. It is often used to determine the width and the peak intensity of ultrashort pulses even if spectral phase information and temporal details are missing. Assuming a certain pulse shape and flat spectral phase, it is possible to obtain an estimate of the temporal FWHM of the pulse. For a Gaussian pulse, the FWHM of the autocorrelation is $\sqrt{2}$ the FWHM of the pulse. An example of intensity autocorrelation is presented in Figure 4.4 using the same 25 fs pulse as above. This technique is called *second order intensity autocorrelation*.

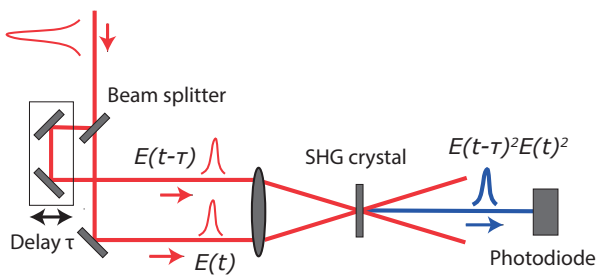

Figure 4.3: Typical intensity autocorrelation setup. The two delayed pulses are focused non-collinearly in a SHG crystal, and the resulting field between them is detected.

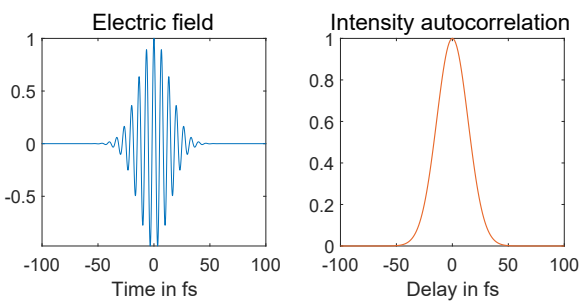

Figure 4.4: Electric field and its intensity autocorrelation

1.4 Interferometric autocorrelation

Combining these two techniques, the interferometric autocorrelation (IAC), also called *2nd order interferometric AC*, consists of placing a SH crystal at the output of a Michelson interferometer. The geometry is *collinear*; all the beams propagate in the same direction. A typical setup is presented in Figure 4.5. The signal recorded is proportional to:

$$G_2(\tau) = \int_{-\infty}^{+\infty} |\,[E(t) + E(t-\tau)]^2\,|^2 dt \tag{4.7}$$

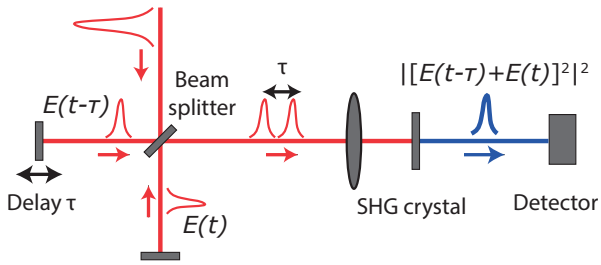

Figure 4.5: A typical interferometric autocorrelation setup

This can be decomposed into several terms [138]:

$$G_2(\tau) = A(\tau) + Re\{4\widetilde{B}(\tau)e^{i\omega_0\tau}\} + Re\{2\widetilde{C}(\tau)e^{2i\omega_0\tau}\} \tag{4.8}$$

with

$$A(\tau) = \int_{-\infty}^{+\infty} \{\mathcal{E}^4(t-\tau) + \mathcal{E}^4(t) + 4\mathcal{E}^2(t-\tau)\mathcal{E}^2(t)\}dt, \tag{4.9}$$

$$\widetilde{B}(\tau) = \int_{-\infty}^{+\infty} \{\mathcal{E}(t-\tau)\mathcal{E}(t)\left[\mathcal{E}^2(t-\tau) + \mathcal{E}^2(t)\right] e^{i[\varphi(t-\tau)-\varphi(t)]}\}dt, \tag{4.10}$$

$$\widetilde{C}(\tau) = \int_{-\infty}^{+\infty} \{\mathcal{E}^2(t-\tau)\mathcal{E}^2(t)e^{2i[\varphi(t-\tau)-\varphi(t)]}\}dt. \tag{4.11}$$

$G_2(\tau)$ is composed of a DC component $A(\tau)$, a term with $\widetilde{B}(\tau)$ oscillating around ω_0 and a term with $\widetilde{C}(\tau)$ oscillating around $2\omega_0$. $A(\tau)$ represents intensity autocorrelation. For $\tau = 0$, the peak value is $6\int \mathcal{E}^4(t)dt$. For infinite delay it is $2\int \mathcal{E}^4(t)dt$. The peak-to-background ratio is $3:1$. $A(\tau)$ is called intensity autocorrelation with background, as opposed to the background-free intensity autocorrelation $G_1(\tau)$ defined earlier.

When considering all the terms in $G_2(\tau)$, they add up constructively to $16\int \mathcal{E}^4(t)dt$ for zero delay. For infinite delays, it is again $2\int \mathcal{E}^4(t)dt$. The peak-to-background is $8:1$.

An example of interferometric autocorrelation can be seen in Figure 4.6 using the same 25 fs pulse as above. The peak-to-background ratio is $8:1$. The solid black line is obtained by low-pass filtering; the signal is Fourier transformed and frequencies higher than $\omega_0/2$ are cut. This corresponds to intensity autocorrelation with background, and a $3:1$ ratio.

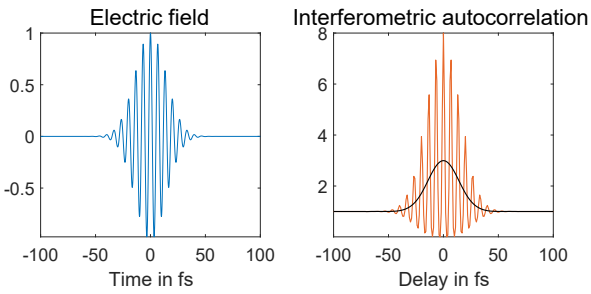

Figure 4.6: Pulse field and its interferometric second order autocorrelation. The solid black line is obtained by low-pass filtering and generates intensity autocorrelation with background.

1.5 Higher order autocorrelation

If the process order is more than two, it is possible to perform higher-order autocorrelation. For a n-order process, this yields:

$$G_n(\tau) = \int_{-\infty}^{+\infty} |\left[E(t) + E(t-\tau)\right]^2|^n dt \tag{4.12}$$

Several orders of autocorrelation are plotted in Figure 4.7. The main oscillation period is always ω_0, $2\omega_0$ is present for the second order AC and higher order are present for the higher order AC. As expected, the profile narrows for higher orders. We use a 45-fs long pulse at 800 nm, similar to the IR pulse in our experiments.

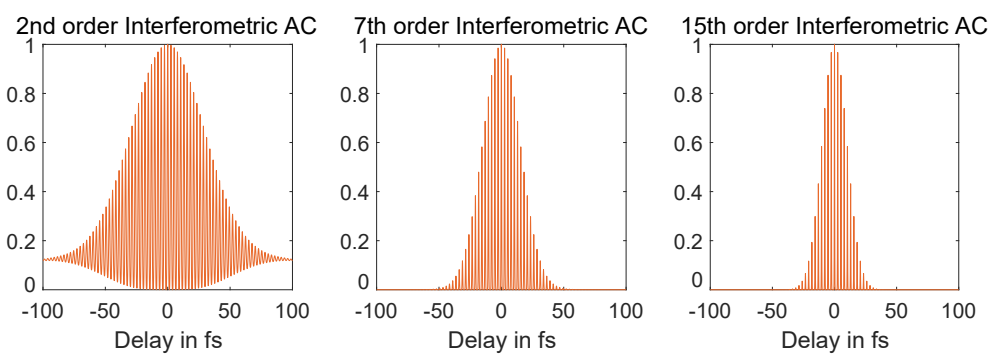

Figure 4.7: Interferometric autocorrelation for a 45 fs IR pulse: a) Second order b) 7th order c) 15th order.

1.6 Autocorrelation with attosecond pulses

We are now going to investigate how the autocorrelation patterns would look like with the attosecond pulses used in the intense XUV beamline.

First let us consider the case of a pulse of carrier frequency ω_q. The main oscillation frequency of the second order interferometric autocorrelation (IAC) is frequency ω_q. The electric field of such a pulse, 20-fs long for harmonic 19, is plotted in Figure 4.8 a) and its second order IAC in Figure 4.8 c). The period of the oscillations is 137 as. If two frequencies are present, interference beating appears between them. The electric field of the combination of H19 and H33 is plotted in Figure 4.8 b), and its second order IAC in Figure 4.8 d).

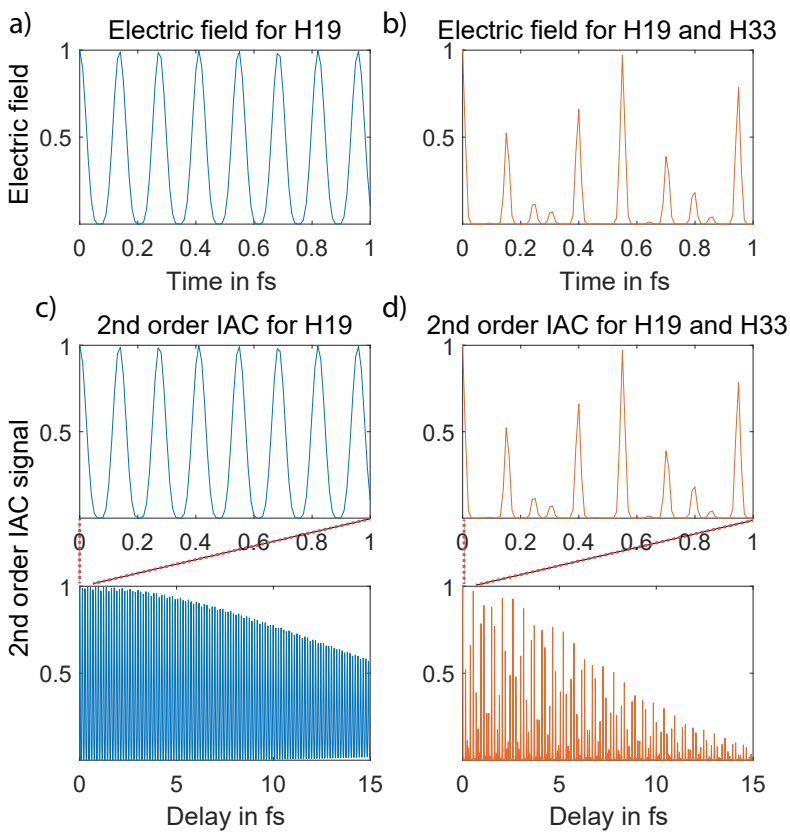

Figure 4.8: The electric field for one harmonic H19 a) and for two harmonics H19 and H33 b). Second order interferometric autocorrelation for c) H19, d) H19 and H33 in a 30 fs range and magnified in a 1 fs range. The oscillation frequency is ω_{19} for c) and a complex beating between ω_{19} and ω_{33} for d)

An interesting feature of the attosecond pulses is that they are often generated in a train. An Attosecond Pulse Train (APT) is the sum of different odd harmonics of the driving field

ω_0. It can be described, with A_{2n+1} the amplitude, ϕ_{2n+1} the relative phase, as:

$$E(t) = \sum_{n=n_1}^{n_2} A_{2n+1} e^{-i\{(2n+1)\omega_0 t + \phi_{2n+1}\}} \tag{4.13}$$

The temporal periodicity of the train pulse is 1.3 fs, corresponding to a half-cycle of the driving 800-nm IR field. An example of the electric field of a train composed of 20-fs long harmonics between H15 and H33 is plotted in Figure 4.9. The train is phase locked and all the harmonics have the same amplitude. The coherent sum of the different frequencies creates a comb interference pattern. This interference phenomena can similarly be understood as the way that an ultrashort pulse is formed by adding many different frequencies in phase: in the end, the most constructive signal is reached where they are in phase. This happens every half-cycle of the IR field that drives the HHG process.

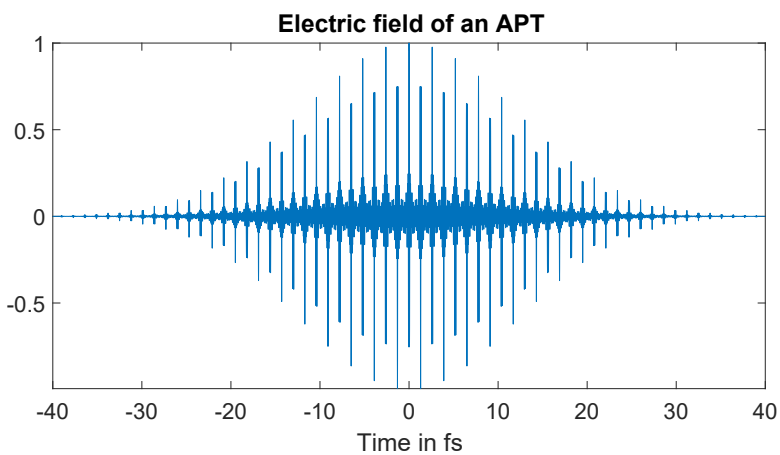

Figure 4.9: Electric field of an APT composed of 20-fs long harmonics between H15 and H33. The periodicity of the modulation is 1.3 fs, half the driving IR-field period.

Autocorrelation of such a train also leads to a complex temporal interference pattern. The simulated second order IAC is plotted in Figure 4.10. The intensity modulation contains the high harmonic frequencies but the main modulation occurs at half the period of the IR, every 1.3 fs.

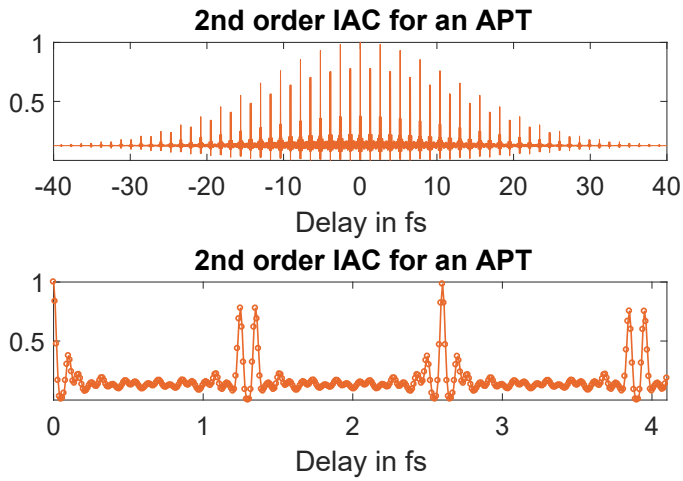

Figure 4.10: Second order interferometric autocorrelation for an APT between H15 and H33. The periodicity of the intensity modulation is half the period of the IR, so there is a maximum every 1.3 fs.

2 Experimental realization

In this section, we first present the device developed for XUV autocorrelation in the intense XUV Beamline: the Split-and-delay Unit (SDU). We then explain how spatial volume effects impact autocorrelation, and present the results of both the offline and multiphoton inline tests.

2.1 Split-and-delay-unit

Introduction

In order to make an XUV autocorrelator, one first needs a device to split the XUV pulse into two and delay one of them: a split-and-delay unit (SDU). There are two ways of splitting a beam: by amplitude or by wavefront. Amplitude splitting is performed with a beamsplitter, which transmits half the energy and reflects the other half. This has the advantage of conserving the spatial properties of the beam, as the replicas are identical. Wavefront splitting consists of reflecting the beam over two plates or mirrors. The two beams have different wavefront and spatial properties.

Autocorrelators for XUV attosecond beams can only be reflective, therefore based on wavefront splitting, for two reasons. First, the XUV radiation is strongly absorbed in every material, as seen in Chapter 3, preventing use of beamsplitters. The second reason is related to temporal characteristics. Ultrashort pulses suffer from dispersion when propagating in a

material. This is also the case for femtosecond ultrashort pulses, which is why all-reflective interferometers have been developed [139–141].

The autocorrelation of attosecond pulses have been demonstrated previously using a dispersionless Michelson interferometer with gratings [142], a split focusing mirror [33, 128, 143], and a vertical split mirror [34, 129, 144]. Analogous developments involved synchrotron [145] and FEL radiation [146], which present similar challenges.

In the following section, a description of our SDU is presented, along with alignment procedures and experimental tests. More details are provided in Paper VII.

Setup

The SDU is located between the generation chamber and the application chamber as shown in Figure 4.11 a). It is composed of two plates that deflect the beam by 20 degrees. Grazing incidence is chosen because, as seen in Chapter 3, it is preferable for XUV optics. A photograph of the SDU is shown in Figure 4.11 b) and the mechanical setup is presented in Figure 4.12 b). The plates are anti-reflection coated for the IR, so most of the IR radiation is transmitted through the plates and stopped afterwards with a beam block. A thin metallic filter (often Aluminum) located before the application chamber allows us to block the remaining IR without stopping the XUV.

The plate positions are monitored by a green laser stabilization system, situated outside the chamber. Holey mirrors, as shown in Figure 4.12, allow the green laser to propagate to the plates at the same angle as the XUV, and take it out of the chamber to the stabilization system. The SDU is set on a translation stage that moves along the plane of the plates, such that it is possible to choose whether the beam will be split in two or not, and adjust the split position/splitting ratio. A beam block on a translation stage can also block one beam or the other, which is useful for alignment.

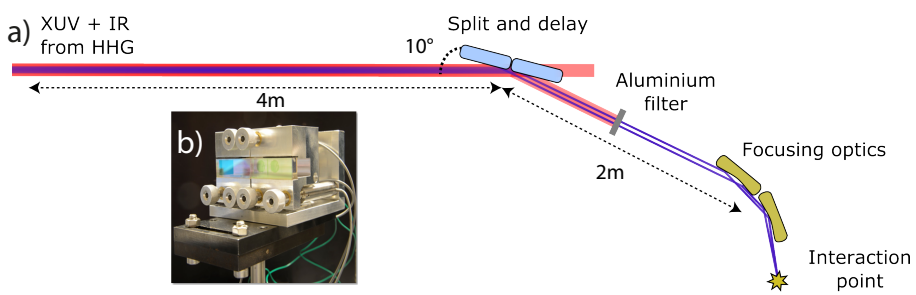

Figure 4.11: a) Position of the SDU in the beamline. b) Photograph of the SDU. Adapted from Paper VII.

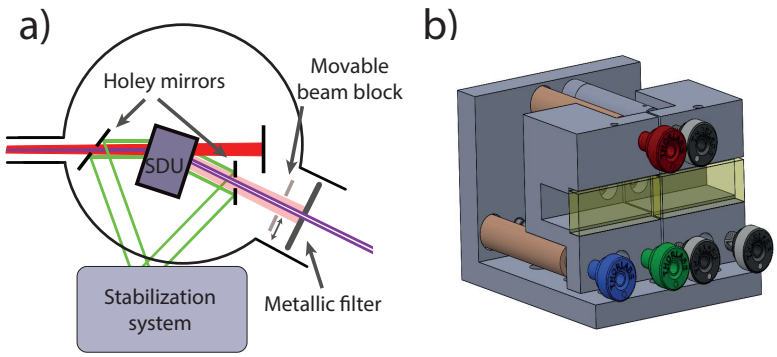

Figure 4.12: a) Position of the SDU in the interferometer chamber. A stabilization system with a green laser is placed outside the chamber, and the green laser is sent to the SDU, and outside the chamber afterwards with holey mirrors. A beam block targets the transmitted IR while a metallic filter stops the remaining IR. A double beam block can target either one of the two split beams. b) Mechanical setup of the SDU. The piezoelectric actuators are in orange, and the silica plates in yellow. The manual actuators for the horizontal axis, vertical axis and pivot are blue, red and green respectively.

Splitting geometry

The two plates of the SDU are made of silica (SiO_2); one is set up on a movable part that is targeted by three piezoelectric actuators. Manual actuators also operate the same motion. The manual actuators are finely threaded differential screws, ensuring a very high precision for prealignment (25 µm/revolution). The piezoelectric actuators have a travel range of 45 µm. The actuators have sub-nanometer resolution, allowing for attosecond resolution. The mechanical assembly is presented in Figure 4.12 b).

The height of the plates was set at 14 mm in order to be fully illuminated by the IR beam. The XUV beam, which is in general less divergent, has a maximum diameter of 1 mm after propagating 4 meters. It is reflected without vertical clipping if properly aligned. The length of each plate was chosen based on the fact that the size of the beam is six times larger in the horizontal plane than the vertical plane due to the 10° incidence angle, i.e., 6 times longer. Each plate is 40 mm long. A thickness of 7 mm was chosen for purposes of mechanical stability.

The space between the two plates is minimized to the thickness of a paper sheet that is used during alignment (around 100 µm). It is important to minimize the gap in order to avoid energy losses. The part of the incoming beam that hits the gap is not reflected. Positioning the plates side by side instead of on top of each other was a priority to reduce energy loss, since the beam is bigger on the plates in the horizontal direction.

The beam is reflected on the two plates, creating two half-beams. One part is reflected with a delay that depends on the displacement of the plate relative to the other. Thus, displacing one plate parallel to the other allows us to scan the delay. The relation between

plate displacement ΔS and temporal delay τ can be expressed with θ the grazing angle as:

$$\Delta\tau[\text{fs}] = 2 \times \Delta S \sin\theta / c = 1.158 \times \Delta S[\mu\text{m}]. \tag{4.14}$$

A small angle reduces the accessible delay range by a factor of $\sin\theta$ but also reduces the influence of mechanical vibrations and the smallest accessible step. With 10 degrees, the maximum range is 50 fs. The optimal direction of the displacement is chosen in order to minimize losses due to "shadowing", which is the direction shown in Figure 4.13 a). If the displacement is in the other direction as in Figure 4.13 b), the central part of the incoming beam is lost. During alignment of the device, we ensure that displacement is in the correct direction for most of the delay range.

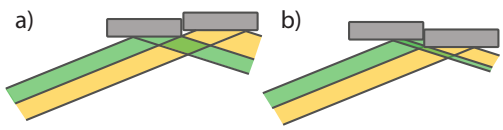

Figure 4.13: Problem of shadowing: in the a) configuration, the whole flux is transmitted while in b), a part of the beam is clipped and the transmitted flux is lower.

Overlap control

In our experimental setup, the beam diverges, the two beams do not have the same focus anymore when displacing one plate parallel to the other, as shown in Figure 4.14 b). Thus, it is therefore necessary to control the beams by tilting the plate horizontally and vertically until the focii overlap, which is achieved when distance δx between V1 and V2 is 0.

For that reason, the plate has three actuators, as shown in Figure 4.12: one for vertical motion (red in Figure 4.12 b)), one for horizontal motion (blue in Figure 4.12 b)) and a pivot one (green in Figure 4.12 b)). Parallel displacement is performed by moving the three actuators by the same value, while correction of horizontal and vertical displacement is done by the corresponding actuator. The stabilization system that was developed to ensure the proper overlap of the two focii and control the relative delay is presented in Paper VII.

Overlap alignment methods were developed. The temporal overlap is monitored using the IR spatial fringes between the two beams. The zero delay is were the fringes contrast is the highest. For the spatial overlap, the spatial mode of the VMIS and the TOF are used. If the plates are not well vertically overlapped, the signal yields two horizontal lines on the VMIS. The resolution of this method is 2 µm, which is the limit to distinguish two 4 µm beams. If the plates are not well horizontally aligned, it yields two different ion packets in the TOF. The principles are presented in Figure 4.15.

In the next section we are going to focus on the peculiarities of our autocorrelator configuration.

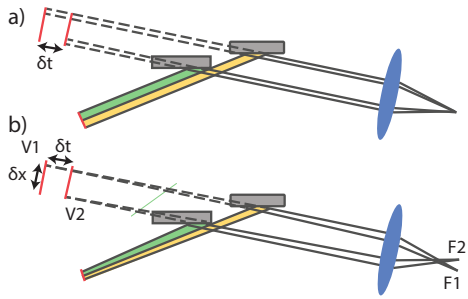

Figure 4.14: a) If the beam is collimated before the SDU, the two split beams focus at the same position even when a delay is introduced, since the two virtual focii are at infinity. b) If the beam is divergent, the two split beams have their virtual focii at different positions V1 and V2 when a delay is introduced, resulting in two focii F1 and F2 in the focal plane.

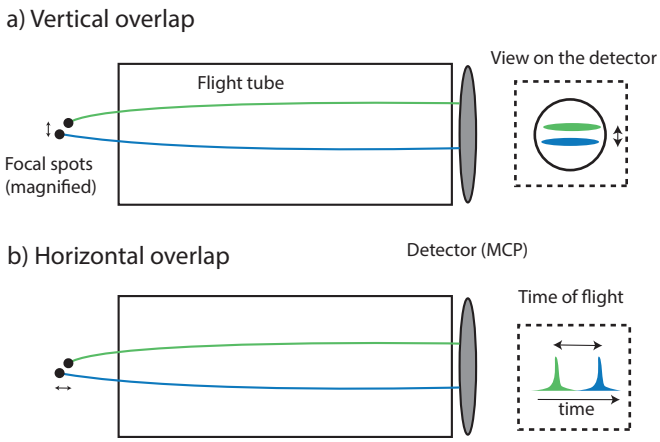

Figure 4.15: a) Alignment of the vertical overlap with the spatial mode of the VMIS. The signal from the two beams forms two shifted horizontal lines on the VMIS detector. b) Horizontal overlap: the two beams yield ions packets arriving at different times on the TOF detector.

2.2 Volume autocorrelation

Spatial effects in the focus As explained previously, we use the nonlinear interaction with a gas medium and not with a thin crystal in our experiments. This implies that we need to consider the effects in a volume instead of just one point.

First, one needs to understand the specifics of our configuration. We performed numerical simulations with a vertically split beam. The two resulting half-beams, left and right, represented in Figures 4.16 a) and 4.16 d), were numerically propagated to the focus. The intensity profiles in the focus are plotted in Figures 4.16 b) and 4.16 e). They are identical, and close to an anisotropic Gaussian profile, longer in the horizontal direction. Their phase profiles are presented in Figure 4.16 c) and 4.16 f). They present a tilt in the horizontal dir-

ection, which is the opposite for the left and right beams. To realistically reproduce our focusing configuration, we used a 0.6 mm FWHM beam focused with 17 cm focal length. The phase variation can be roughly approximated by $\pm \arctan(\alpha x)$ with $\alpha = 0.25$. These results are very close to the analytical calculations reported in [147] for a similar type of splitting configuration.

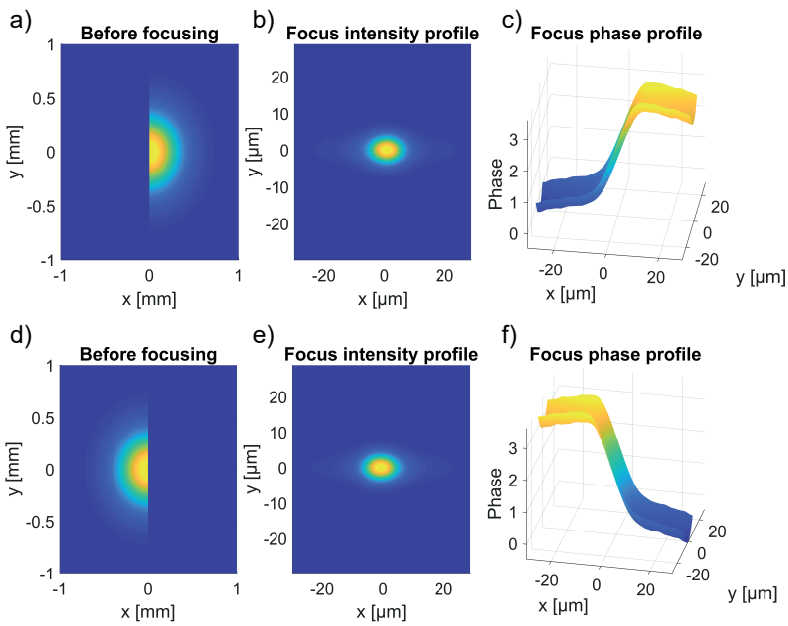

Figure 4.16: a) Intensity profile of the right vertically split beam, b) and c) its intensity profile and phase in the focus. d) e) and f) are for the left beam. The intensity distributions are identical in the focus and close to an anisotropic Gaussian profile. The phases of the left and right beams have an opposite tilt in the horizontal direction.

This phase variation can be understood by considering the case where two non-collinear beams are cross. As shown in Figure 4.17 a), the wavefront in the focus is flat when focusing a Gaussian beam. When two parallel beams cross non-collinearly in the focus, they have different directions and optical axes. Their wavefronts exhibit different tilts relative to the initial propagation direction, as shown in Figure 4.17 b). The phase of the two beams in the focus is equal to $\pm\alpha x$, with α as the relative angle between the propagation direction before the lens and the beam direction after it. The focal spot is also bigger, as the size of the focal spot is inversely proportional to the diameter of the beam before the lens (see Eq 2.8). With our configuration (Figure 4.17 c)), if the delay between the beams is 0, it is equivalent to the full beam focusing: the focus has the same size and the wavefront is flat in the focus. When a delay is introduced, the interference pattern between the two half-beams changes, the focal spot becomes bigger and a tilt is introduced in the focus similarly to the case of the non-collinear crossing.

In order to better understand how this interference pattern changes with the delay, let us

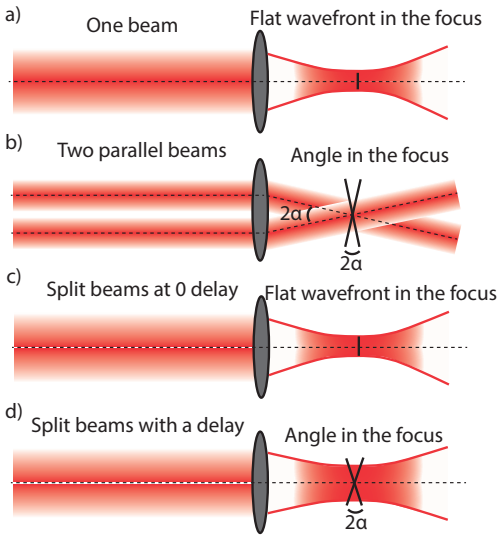

Figure 4.17: a) When a Gaussian beam is focused, the wavefront is flat in the focus. b) When two shifted parallel beams are focused by the same lens, their wavefronts are tilted in the focus and the focal spot is bigger c) When a Gaussian beam split in two is focused by a lens, at zero delay it is equivalent to the full beam case. d) If there is a delay between the two beams, the wavefronts of the two halves are crossed and the focal spot bigger as in b).

consider two beams that cross in the focus with a relative delay compared to each other. The phase difference between the beams varies spatially. This spatial variation also depends on the delay. This is illustrated simply in Figure 4.18. For each Figure 4.18 a), 4.18 b) and 4.18 c), the phase difference is 0, as indicated by orange dots, when two wavefronts with the same delay (mod 2π) cross. A π phase difference is indicated with a blue dot. The dots with the same phase are aligned in the z-direction, forming an intensity profile with constructive and destructive interference patterns, as represented by the orange curves. The interference patterns moves as a function of the delay.

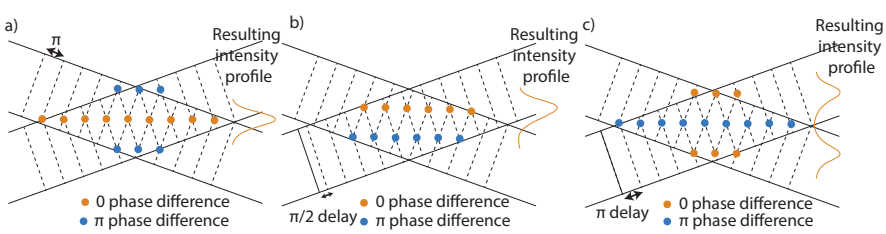

Figure 4.18: An intuitive image when two beams have crossed wavefronts in the focus. Dotted black lines representing the wavefronts are drawn every π. Orange dots represent the crossing of the two beams in phase, and blue dots when there is a π phase difference. The sum over all points in the plane creates a spatial profile with constructive and destructive interference fringes.

In order to validate this intuitive concept, we carried out numerical simulations in one (x, y) plane. Two beams with identical Gaussian profiles $U(x, y)$, and opposite tilts φ_1 and

φ_2 in the x-direction were added up with a delay $\omega\tau$:

$$E_{focus} = U(x,y)e^{i\varphi_1} + U(x,y)e^{i(\varphi_2+\omega\tau)}$$
$$\text{with} \quad U = e^{-\log(2)(x^2+y^2)} \quad \text{and} \quad \varphi_{1,2} = \pi/2 \pm \arctan \alpha x \tag{4.15}$$

A destructive interference fringe appears in the spatial profile and moves according to the delay $\omega\tau$, as shown in Figure 4.19 a). The peak intensity, plotted in Figure 4.19 c), is not constant when the delay varies, but oscillates as $\cos(\omega\tau)$. This illustrates why we need a nonlinear signal for our autocorrelation experiments, given that a linear signal would be constant as a function of the delay such that no information could be extracted. The contrast of the intensity variation depends on the angle α between the two beams. For parallel beams, the contrast is at its maximum and the interferences is fully destructive. The larger the angle, the lower the contrast and the more interference fringes appear in the spatial profile.

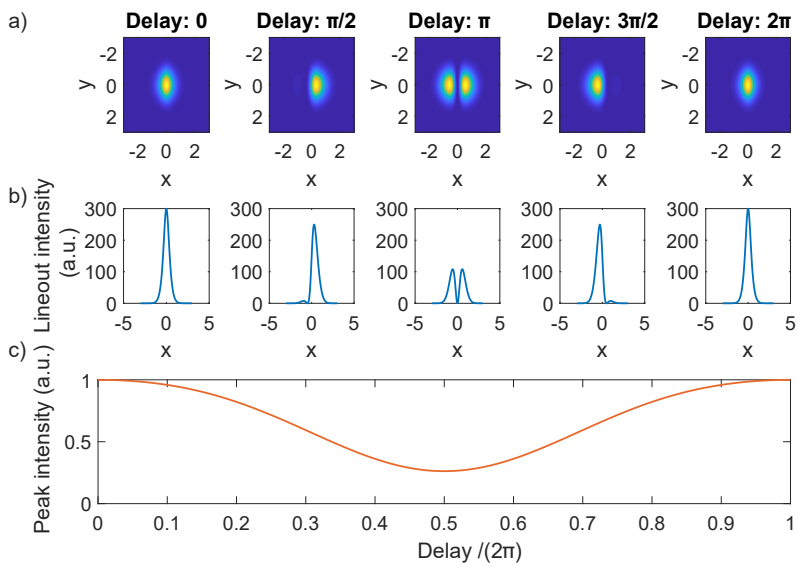

Figure 4.19: Spatial interference profile between two beams with phase angle. a) Spatial profile for different delays. A destructive interference fringe is clearly visible and is moving according to the delay. b) An horizontal lineout in the middle of the spatial profile. c) The variation of the peak intensity as a function of the delay. It is periodic and is at its minimum for a half-period, where the destructive interference fringe is in the middle of the spatial profile.

Spatio-temporal autocorrelation This spatial modulation modifies the second order autocorrelation (see Eq.4.7), which can be calculated as

$$G_2(\tau) \propto \iiint |E_{focus}(x,y,t,\tau)^2|^2 dxdydt \tag{4.16}$$

with

$$E_{focus}(x,y,t,\tau) = e^{-t^2/(2\sigma^2)}\,U(x,y)e^{i\varphi_1} + e^{-(t-\tau)^2/(2\sigma^2)}\,U(x,y)e^{i(\varphi_2+\omega\tau)}. \tag{4.17}$$

We calculated interferometric autocorrelation $G_2(\tau)$ in the case where the two beams are parallel, the regular collinear case as in Figure 4.17 a), as well as when the phases of the two beams are tilted with $\varphi_1(x)$ and $\varphi_2(x)$ as in Figure 4.17 c), which is the same for the wavefront splitting configuration. We obtained the curves plotted in Figures 4.20 a) and 4.20 b). In the collinear case, the contrast is $8:1$ as expected from Section 1.4, while with the wavefront split the shape changes and the contrast drops to $4.5:1$. However, the main oscillation frequency ω remains the same.

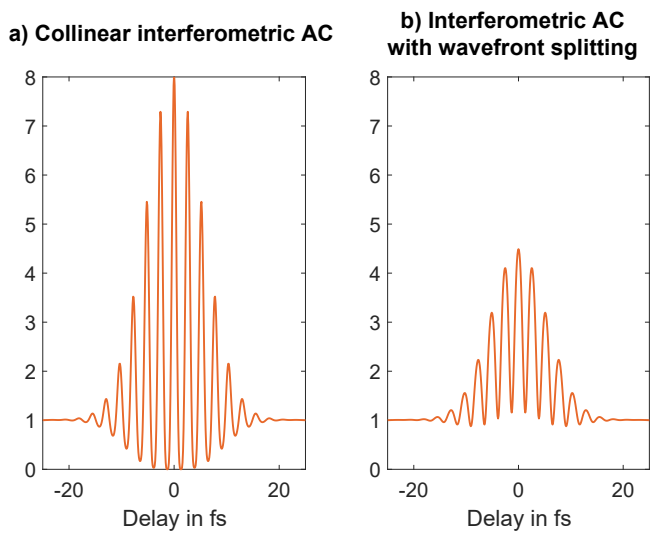

Figure 4.20: Interferometric autocorrelation simulation, for the collinear case a) and with a phase tilt between the two beams b). The oscillations have the same frequency but the contrast is reduced with wavefront tilt from $8:1$ to $4.5:1$.

These simulations were performed in one plane. The next step would be to take into account the entire volume of the interaction region. However, the gas jet width is 1 mm FWHM which is on the order of the Rayleigh range, so the gas jet is 2 times smaller than the focal region ($2z_R$), which justifies our approximation that neglects the volume effects. Full volume AC calculations have been reported in [128, 148], and showed that the peak-to-background ratio decreases even further to $2.8:1$ for the interferometric AC and $2.1:1$ for the intensity AC in that particular configuration. The fast oscillations at ω are however still present and measurable. To avoid the problem of contrast losses in volume autocorrelation, gratings were used to return to a collinear configuration and suppress the volume effect [149]. Full interferometric autocorrelation in krypton at 160 nm was [150], with a peak to background ratio close to the expected $8:1$.

To conclude, with our wavefront splitting configuration, a spatial phase difference appears between the two beams when focused. It lowers the contrast of the autocorrelations, but does not affect theoretically measurable oscillation frequencies.

2.3 Offline autocorrelation tests

In order to test the SDU offline, first and second order autocorrelations of an IR laser were performed and presented. These experiments are described in more detail in Paper VII.

Field autocorrelation

A few-cycle high-repetition rate laser was used for this measurement. The IR was focused and a pinhole was placed in the focus, followed by a photodiode, as shown in Figure 4.21. The pinhole allows the selection of only a specific part of the focus in order to avoid the volume effects described previously.

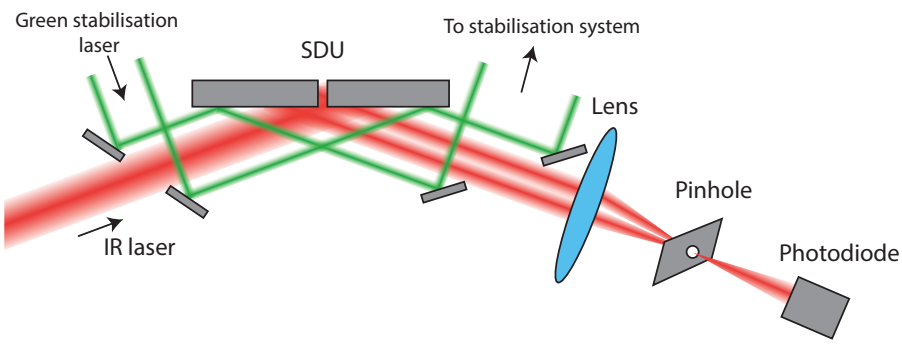

Figure 4.21: Field autocorrelation setup. The IR laser beam is reflected on the split-and-delay unit, and the two split beams are focused to a pinhole. The resulting signal is detected by a photodiode. The delay and overlap are monitored during the scan with the green laser stabilization system described in Section 2.1 and in Paper VII.

The resulting autocorrelation is shown in Figure 4.22 a). The laser spectrum before the SDU was measured and is shown in Figure 4.22 b). From that spectrum, we calculated the expected field autocorrelation, assuming a Fourier-limited pulse. It correlates well with the measured one. The difference can be explained by the assumption of a flat spectral phase and the possibility that the coating modifies the bandwidth. Another cause is the selection of only a small part of the focus, ignoring possible spatial chirp.

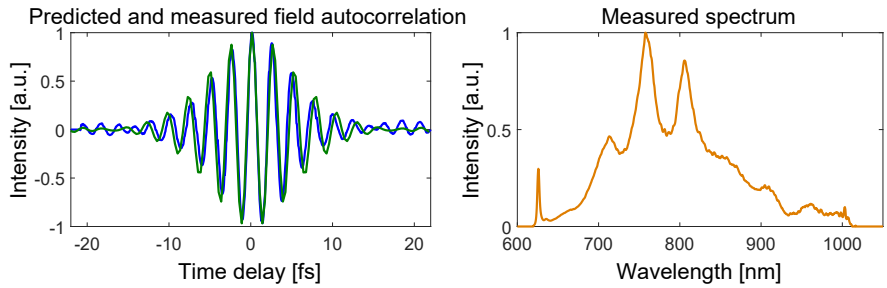

Figure 4.22: Measured field autocorrelation (in blue) compared to the predicted one (in green) from the few-cycle laser spectrum shown in the right panel. Adapted from Paper VII.

Second-order autocorrelation

Afterwards we performed an all-reflective second-order interferometric autocorrelation. The pinhole was replaced by a second harmonic crystal. The setup is shown in Figure 4.23.

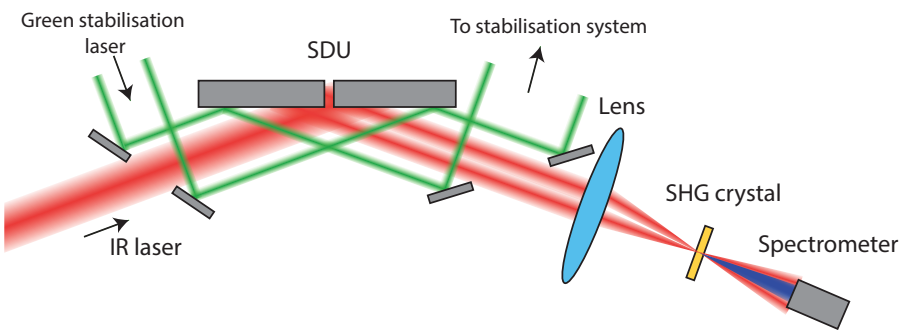

Figure 4.23: Second-order autocorrelation setup. Similar to Figure 4.21, but the pinhole is replaced by an SHG crystal and the photodiode by a spectrometer.

The delay was varied while recording the spectrum with a fiber spectrometer, similar to FROG. The results for a compressed and an intentionally stretched pulse are shown in Figures 4.24 a) and 4.24 b) respectively. Integration of the signal over the bandwidth is shown in Figures 4.24 b) and 4.24 d) in blue as a function of the delay. The low-pass component after filtering is drawn as a black dashed line. A Gaussian fit to the low-pass component is plotted as a red solid line. The oscillation period of the fringes is around 2.8 fs, which roughly corresponds to the IR period.

The fit assumes a Gaussian shape and yields pulse durations of 9.1 fs for the compressed pulse and 25.5 fs for the stretched one. This is in rough agreement with the durations of 6.2 fs and 30 fs measured with the d-scan technique. The peak-to-background ratio, around 5 : 1, is lower than 8 : 1 as expected because of the volume effect. This test showed

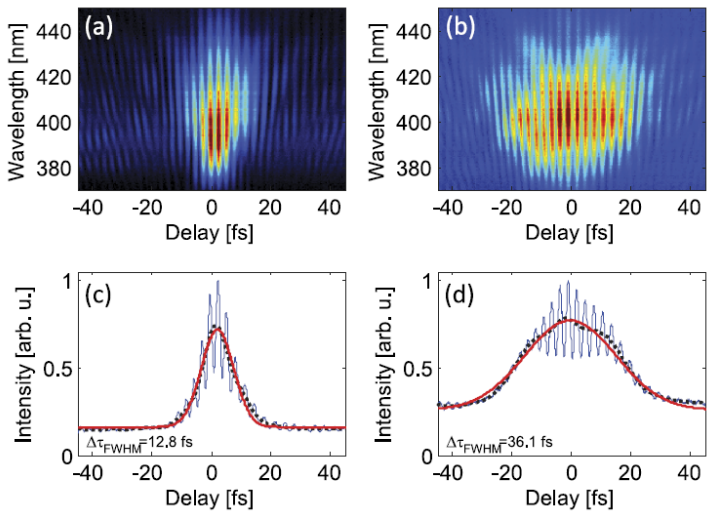

Figure 4.24: Second-order autocorrelation with the SDU, for two pulse durations: 6.2 fs (a) and (c), and 30 fs (b) and (d). The top panels show the evolution of the spectrum with the delay, and the bottom panels show the spectrally integrated signal for each delay. The slowly varying component is in a dashed black line, with a solid red Gaussian fit. Reproduced from Paper VII.

that this device permits us to obtain interferometric fringes and see a clear effect of the pulse duration.

2.4 High-order interferometric autocorrelation

Once the SDU was integrated in the beamline, an initial way to test for the spatial and temporal overlap of the beams was to observe the ionization of Argon with the IR laser. It is a highly nonlinear strong field process that has a power dependence with the laser intensity of more than ~ 6. As the process order is high, the temporal and spatial overlap of the two pulses is critical to observe a signal, which makes it a good test of the interferometer.

The positive ions generated by the interaction of the IR pulses and a gas jet of Argon were recorded with the VMI spectrometer described in Chapter 1. For each point the signal was accumulated for 200 shots, in steps of 100 as. The stability of the delay was around 50 as. The signal is the sum of the positive ions detected, mainly Ar^+ as well as Ar^{2+} and Ar^{3+}.

We observed sharp constructive and destructive interferences as shown in Figure 4.25 a), with a frequency corresponding to the IR. It is also possible to observe a drop of the signal envelope on both sides of the delay range. The signal is plotted as a function of the relative delay, as we do not have an absolute calibration for the 0-delay position.

We performed simulations in order to reproduce this signal, for $n = 4$ and $n = 7$. The

4th order IAC simulation with a 62-fs-long pulse is plotted in Figure 4.25 b). It seems to reproduce the observed signal very well. Because of the volume effect, the minima reach 0.1 instead of 0, as in Figure 4.25 a). For the 7th order, which is more realistic for this process, the IAC becomes narrower. To compensate, we used a longer pulse duration for the simulation, 83 fs. The result is plotted in Figure 4.25 c). It also fits well, but the minima reach 0 instead of 0.1.

These results are different from what we expected with our experimental parameters ($n \geq 7$ and a 50-fs-long pulse). One possible explanation is that the pulse duration is measured outside a vacuum. Propagation of the compressed pulse in air and then through a lens and a glass window increases the pulse duration by an unknown amount. Another explanation is that the observed signal is not exactly an IAC, as many ions, including the background, are ionized, not only Ar^+. To conclude, this experiment validates the SDU alignment and confirms that our delay calibration is correct, but it also calls into question the actual pulse duration of the IR pulse in vacuum.

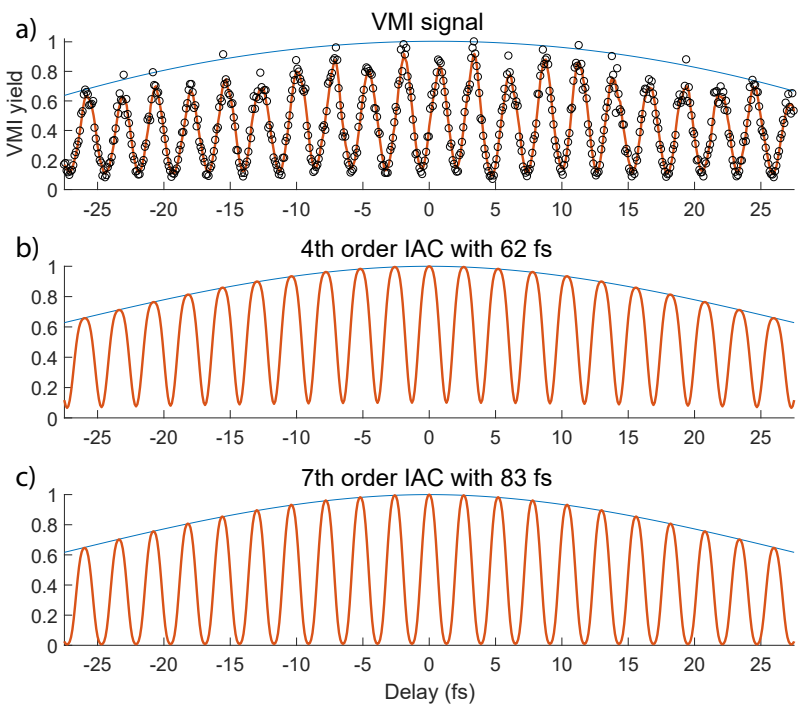

Figure 4.25: a) Total yield on the detector from the ionization of Argon. Clear oscillations of 2.6 fs period are visible. The blue line is an enveloppe fit. b) Simulation of a 4th order IAC with a 62-fs-long pulse, and volume effect. c) Simulation of a 7th order IAC with a 83-fs-long pulse, and volume effect.

2.5 APT autocorrelation

In our experiments, we use a train of attosecond pulses (APT), composed of about 10 harmonics between H15 and H35. As explained in Section 1.6, we expect to see a complex interference pattern between all the frequencies, with maxima every half period of the IR field so every 1.3 fs, as the simulations in Figure 4.26. Due to the number of frequencies contributing to the signal, Fourier analysis is necessary during time-resolved experiments to extract and separate the different components. This is called "nonlinear Fourier-transform spectroscopy" [118, 121].

As discussed previously, volume has an impact on the autocorrelation signal but it reduces only the contrast. In Figure 4.26, the simulations that take into account the tilt in the focus, as in Section 2.2, show that the peak-to-background ratio is 4.1 : 1. 3D volume simulations of interferometric autocorrelation were performed [128] for an APT and showed very similar results, only with further reduced contrast because of the volume effect. The fast oscillations should still be visible if temporal resolution is sufficient.

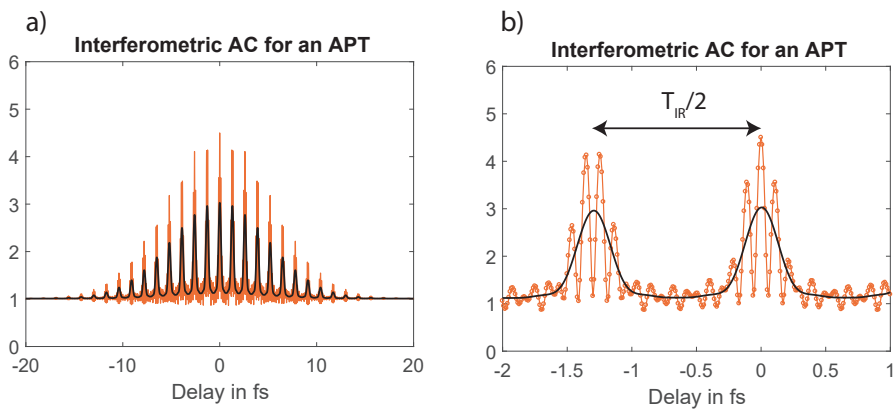

Figure 4.26: a) Interferometric AC for an APT, including volume effects, for a 40 fs range, and b) for a reduced range of 3 fs.

Several experimental difficulties prevent us from measuring the volume autocorrelation of an APT. First, the overlap between the two split beams is critical. Our routines allow for daily alignment, but obtaining a 2 µm precision for a 4 µm beam stretches the limits of the current system. Second, the beam pointing fluctuations directly impact the splitting ratio, which is detrimental to the contrast of the oscillations. Developments to reduce the pointing fluctuations are ongoing . Last, it is possible that the different harmonics do not have the same focus because of the dipole phase defocusing (see Chapter 1), which is yet to be investigated. Overall, the signal levels are so low that very long acquisition times are required, such that ensuring good stability over a very long time is challenging. To our knowledge, these fast oscillations were measured only once with an APT [34, 129] due to experimental difficulties. At the least, the intensity AC yields information about the

duration of the ”wagons” of the train pulses [33, 128].

Summary and outlook

The work presented in this thesis concerns the generation of attosecond pulses through HHG, and their use for nonlinear experiments on atoms and molecules at the intense XUV beamline of the Lund High Power Laser Facility. Nonlinear time-resolved experiments, such as XUV-pump XUV-probe, could lead to a better understanding of ultrafast atomic and molecular processes. The combination of a high XUV flux and its focusing to a small focal spot is a requirement to perform nonlinear experiments. The main results of this work all contribute to this goal:

- A general model for scaling nonlinear processes in gases, such as HHG and filamentation, was presented, and scale-invariance was experimentally demonstrated using filamentation [Paper I]. Going towards high energy filaments can be a way to generate intense ultrashort IR pulses, which themselves could lead to isolated attosecond pulse generation. The loose focusing configuration of the beamline is based on the scaling concept, allowing for the generation of high XUV flux.

- The XUV beam is micro-focused with a double toroidal mirror in a Wolter-like configuration to ensure high intensity on target. The first nonlinear experiments with XUV pulses in the beamline were realized. Two-photon double ionization of neon was observed, proving that the setup is capable of reaching a high intensity estimated to 3×10^{12} W/cm^2 [Paper II].

- In order to optimize the focal spot size, it is necessary to minimize the XUV aberrations. A wavefront sensor was used to monitor the beam quality, and align the focusing optics [Paper IV]. It led to an estimation of the focal spot size to 3.6×4 μm. The evolution of the wavefront quality with the generation conditions was monitored and the transfer of aberrations from the IR to the XUV explored [Paper VI]. In Paper VII we studied the focus of harmonics and how the position of the focus depends on the generation position.

- Finally, the interferometer for splitting and delaying the beam was developed and

tested [Paper III], proving that it is suitable for realizing time-resolved experiments with good temporal resolution.

In addition to this work, i.e. optimizing the intensity on focus, a double VMIS was developed for the intense XUV beamline in order to detect simultaneously the kinetic energies of ions and electrons and perform covariance analysis [Paper V].

Attempts to perform XUV-XUV time-resolved experiments in neon were so far unsuccessful. There are still limitations preventing us from seeing clear time-dependent structures. The yield of nonlinear processes being very low results in long acquisition times of several hours, over which maintaining a good stability is challenging. The energy fluctuations of the IR laser impact both the yield and the spectrum generated for each shot and also on the long-term. The pointing instabilities affect the splitting ratio, to which the time-resolved signal is sensitive. The sensitivity of the harmonic focus to the generation position and the induced chromatic aberration could also be a limitation, as the highest harmonic orders are the main contributors to the signal in certain processes, such as sequential TPDI.

Future developments

Technical developments at the beamline are planned to address these problems. To reduce the fluctuations, the beam path will be fully placed under vacuum, the energy and the splitting ratio for each shot will be monitored and this information will be synchronized with the DMVIS software. A spectrometer will also be built after the focal region to analyze the shot-to-shot spectrum.

New setups will be added to the beamline. An optical parametric amplifier (TOPAS) will be used to mix two colors during HHG, with the aim to enable the generation of IAPs. Other interferometers have been developed, to allow for IR/XUV experiments such as RABBIT, or even IR/XUV/XUV pump-probe experiments, and will be implemented in the near future. Another interferometer will enable molecular alignment.

The work presented in this thesis highlighted the need for monitoring and controlling the spatial properties of the XUV beam. An XUV wavefront sensor was built and will be used for day-to-day optimization. Combined with the deformable mirror, it could lead to a better insight into how to control the XUV aberrations. Wavefront measurements with a spectrally resolved wavefront sensor are also planed to study the influence of the generation position on the XUV spatial properties.

Outlook

The knowledge gathered in the intense XUV beamline has been applied in the conception of the GHHG (Gas HHG) LONG beamline in ELI-ALPS [79]. ELI-ALPS, European Light Infrastructure - Attosecond Light Pulse Source, is a European facility based in Szeged, Hungary. The GHHG LONG beamline represents one step further in the up-scaling, as the beamline is 45 meters long. A drawing of the beamline is presented in Figure 4.27. It will be driven by a state-of-the-art OPCPA (SYLOS) laser. The SYLOS laser provides 45 mJ, $<$ 10 fs, CEP-stable pulses at 1 kHz repetition rate, at a tunable wavelength around 880 nm [151], which gives a peak intensity of 5 TW. A further planed upgrade will deliver pulses below 5 fs, reaching 20 TW peak intensity. Most of the features of the GHHG LONG beamline were designed based on the knowledge acquired at the intense XUV beamline in Lund. The split-and-delay unit and the Wolter-like double toroiral mirror are directly transposed from our design. The post-generation interferometer setup allowing for various pump-probe schemes with up to four different IR, second/third harmonic and XUV beams was also adapted and developed from our design. This drastic up-scaling of the laser and beamline parameters will open up unprecedented opportunities to realize time-resolved experiments with intense IAPs or APTs.

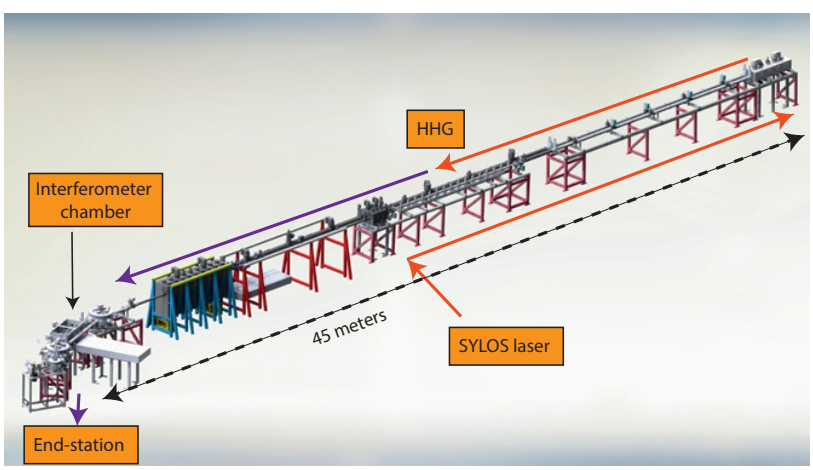

Figure 4.27: THE HGGH LONG beamline in ELI-ALPS, 45 meters long, driven by the SYLOS laser.

To conclude, when the technical challenges are solved, the generation of intense IAP will allow to unravel sub-femtosecond dynamics in atoms and molecules. Studying the dynamics at the electron timescale would lead to a greater understanding of fundamental processes, such as ionization, excitation, molecular dissociation, etc. The way the charge transfers between atoms in a molecule is not yet understood. A desirable outlook after observing such dynamics is to control them. Controlling the charge transfer or fragmentation process could have a tremendous impact in chemistry and biology.

The author's contributions

Paper I: Scale-invariant nonlinear optics in gases

In this paper, we show for the first time the scale invariance of most nonlinear optics phenomena in gases and present a general scaling method for HHG and filamentation. I played an active role in the experiments demonstrating the scale invariance of filamentation and contributed to the manuscript with feedback.

Paper II: Two-photon double ionization of neon using an intense attosecond pulse train

In this paper, we present the first results of two-photon double ionization of neon with the intense XUV beamline, opening the door to further nonlinear experiments. We measured the pulse energy and the focal spot size to estimate the XUV intensity on target to 3×10^{12} W/cm^2. I took part in the experiments, participated in the discussions and provided feedback on the manuscript.

Paper III: A Versatile Velocity Map Ion-Electron Covariance Imaging Spectrometer for High-Intensity XUV Experiments

In this paper, we present the design of a double-sided Velocity Map Ion-Electron Spectrometer, along with the initial results and covariance analysis. I took part in the experimental acquisition of data and provided feedback on the manuscript.

Paper IV: Micro-Focusing of Broadband High-Order Harmonic Radiation by a Double Toroidal Mirror

In this paper, we present the focusing optics of the intense XUV beamline, along with wavefront sensing experiments to optimize the focusing and estimate the focal spot size. I performed focal spot and wavefront sensing experiments, wavefront analysis and numerical ray-tracing simulations. I prepared half of the figures and wrote a major part of the manuscript.

Paper V: Single-shot XUV wavefront measurements of high harmonics

We present a series of measurements of harmonic wavefront, and study the transfer of aberrations from the IR to the XUV. This work was a collaboration with the group of Philippe Zeitoun in LOA, which provided the XUV wavefront sensor. I took part in the experiments, and played a major role in the development of the model. I performed the numerical simulations and wrote parts of the manuscript.

Paper VI: Spatio-temporal coupling of attosecond pulses

We investigate the influence of the generation position on the harmonic divergence and focus position using analytical derivation based on Gaussian optics, TDSE calculations and harmonic divergence measurements. The variation of harmonic divergence is experimentally observed. I participated in the early discussions for developing the Gaussian optics model, made a figure and contributed with feedback to the manuscript.

Paper VII: Design and test of a broadband split-and-delay unit for attosecond XUV-XUV pump-probe experiments

We present the design and preliminary tests of a split-and-delay unit and its active stabilization scheme. I set up, tested and improved the stabilization system, both hardware and software. I performed autocorrelation tests using a 200 kHz OPCPA system, and analyzed the data. I contributed to the manuscript through making figures and providing feedback. I share the first authorship with Filippo Campi.

Acknowledgments

I know that this is the first (and only?) page that you will read when this thesis finally ends up in your hands, and ironically it is often the last one that one writes. At the start of your PhD journey, your name will not appear in the acknowledgments because all the theses were written before you joined the group. One day it will start appearing, in a standard way in the beginning, and then in a way reflecting your personality and impact on the group. Many years after your graduation, the memory of you will slowly fade away... The acknowledgments pages of the group thesis are therefore just a long-term pump-probe experiment on your personality and on the group dynamics.

I would like to first thank Anne for giving me the opportunity to join the group and supervising me for the last four years. You created such a nice and welcoming group atmosphere, where everyone can express themselves, proving that ambitious research and treating everyone kindly and humanely are not incompatible. It is very inspiring to see the sparkle of fresh curiosity in your eyes when discussing a new idea. Your perseverance is remarkable, never giving up and transforming an intuition into two papers in half a year! Please keep spreading the love of physics. Thank you as well for putting me back on track when I was drifting away; starting a PhD at the age of 22 was harder than what I thought. I really appreciated the quality of your feedback during the writing, often leading to a lot of things to rewrite, but always in the right direction.

My second thought is for Per, thank you for managing the intense XUV beamline. I love your optimism and dedication to make things work out, and your ability to always come up with a smart idea at the right time. I also appreciate the emphasis you rightfully put on work/life balance, which more researchers should do. May the pump-probe force be with you!

Thank you Cord for bringing your optics perspective and helping me solving both numerical and deep fundamental optics questions. Thank you also for the filament experiments, and for the badminton games. It was nice to have three supervisors who are each specialists in a different field.

I would like to thank Claes-Göran for the amount of work you are doing to keep atomic physics running. Another reason why things at the division are going smoothly is all the competent underground work accomplished by Anne, Åke the rockstar and Jakob. Ni är alltid så snälla och hjälpsamma, tack så mycket!

I would also like to thank Philippe Zeitoun and Hugo for the wavefront campaigns and collaboration which triggered many things. Another fruitful collaboration is with the three Balázs from ELI, it is always a pleasure to have you here.

A special thanks for the "10 Hz" people and all the bullshitting! Jan for the interesting conversations and always being social, Hampus for your special music tastes, Sylvain for the kindness hidden behind your mustache, Filippo for the pineapples on pizzas, Linnea för att du pratade svenska med mig och för pingisen, Christoph for the scaling, Jasper the sailor, Bastian many years ago, and now Hugo. Piotr I am very grateful for all the help and guidance you provided me. Tack Anders for being the holy keeper of the 10 Hz laser, nursing it with your magic touch (which is mostly hard work and experience).

I am glad to have worked in such a social group, so I would like to thank the current and former "atto" people, hoping not to forget someone : Johan, Samuel, Mathieu, Shiyang, Yu-Chen, Lana, Saikat, Marcus, Sara, David B., David K., Jan V., Alexandre, Damien, Timothé, ANne, Arthur, Leon, Jana, Lisa, Ello for your kindness, Fabian, wavefront-Fabian, wavefront-Emma, Emma R. for your positivity aura, Stefanos for sharing your extensive knowledge of languages, music, history and quantum physics, Neven for your sense of humor, Maïté for the skate, the help and the fun (café ?), Marija for sharing my passion for the outdoors, Esben for keeping me good company, Miguel for your precious help at the very beginning. I would like to thank Jenny, Diego, Isabel and Karolina for the student chapter. The intense efforts of the "dipole phase team" have not been unnoticed during the final rush, thank you Hampus, Jan, and especially Chen for your patience facing my multiple questions many times a day.

I am very grateful to the developers behind Overleaf for increasing a lot my writing productivity, and to the AC for making it a pleasure to come to the office and write during the very long summer heat wave.

On the personal level, I have met many fantastic people over these four years, so I will just name a few: Marion, Kenneth, Hani, Mihai, Johan, Lulu, Martin... Ačiū Albertas for all the (banana)bread, nanri Ram for the bean soup, tack Johan för potatis och ost, Joe för konsten, Rebecka för klippningar och bubblor. Merci Laurie pour les mojitos et les forams, Altaaf pour les inombrables lunchs et ta contribution plus ou moins scientifique mais indéniable à ma thèse. Dankeschön Vanessa, dafür dass du du bist! Tack Johanna för din kärlek och för kaniner. Merci aussi à la famille ainsi qu'à Tazou, Mathieu et Ichrak, je vous aime fort! Thanks to the Smålands community for turning Lund into my home. Maybe the real treasure was the friends we made along the way. Lunch ?

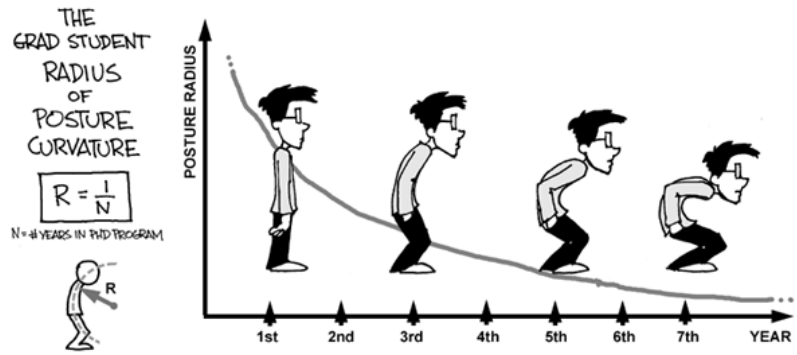

Figure 28: Evolution of the grad student radius of posture curvature as a function of the years. By Jorge Cham, from www.phdcomics.com

References

[1] R. Näsänen, H. Ojanpää, T. Tanskanen, and J. Päällysaho. *Estimation of temporal resolution of object identification in human vision*. Experimental Brain Research, 172(4):464–471, 2006.

[2] A. H. Zewail. *Femtochemistry: Atomic-Scale Dynamics of the Chemical Bond* . The Journal of Physical Chemistry A, 104(24):5660–5694, 2000.

[3] A. McPherson, G. Gibson, H. Jara, U. Johann, T. S. Luk, I. A. McIntyre, K. Boyer, and C. K. Rhodes. *Studies of multiphoton production of vacuum-ultraviolet radiation in the rare gases*. Journal of the Optical Society of America B, 4(4):595, 1987.

[4] M. Ferray, A. L'Huillier, X. F. Li, L. A. Lompre, G. Mainfray, and C. Manus. *Multiple-harmonic conversion of 1064 nm radiation in rare gases*. Journal of Physics B: Atomic, Molecular and Optical Physics, 21(3):L31–L35, 1988.

[5] P. M. Paul, E. S. Toma, P. Breger, G. Mullot, F. Augé, P. Balcou, H. G. Muller, and P. Agostini. *Observation of a train of attosecond pulses from high harmonic generation*. Science, 292(5522):1689–1692, 2001.

[6] M. Hentschel, R. Kienberger, C. Spielmann, G. A. Reider, N. Milosevic, T. Brabec, P. Corkum, U. Heinzmann, M. Drescher, and F. Krausz. *Attosecond metrology*. Nature, 414(6863):509–513, 2001.

[7] C. Ott, A. Kaldun, L. Argenti, P. Raith, K. Meyer, M. Laux, Y. Zhang, A. Blättermann, S. Hagstotz, T. Ding, R. Heck, J. Madroñero, F. Martín, and T. Pfeifer. *Reconstruction and control of a time-dependent two-electron wave packet*. Nature, 516(7531):374–378, 2014.

[8] E. Gagnon, P. Ranitovic, X. M. Tong, C. L. Cocke, M. M. Murnane, H. C. Kapteyn, and A. S. Sandhu. *Soft X-ray-driven femtosecond molecular dynamics*. Science, 317(5843):1374–1378, 2007.

[9] A. S. Sandhu, E. Gagnon, R. Santra, V. Sharma, W. Li, P. Ho, P. Ranitovic, C. L. Cocke, M. M. Murnane, and H. C. Kapteyn. *Observing the Creation of Electronic*. Science, 23(November):1081–1085, 2008.

[10] F. Kelkensberg, C. Lefebvre, W. Siu, O. Ghafur, T. T. Nguyen-Dang, O. Atabek, A. Keller, V. Serov, P. Johnsson, M. Swoboda, T. Remetter, A. L'Huillier, S. Zherebtsov, G. Sansone, E. Benedetti, F. Ferrari, M. Nisoli, F. Lépine, M. F. Kling, and M. J. J. Vrakking. *Molecular dissociative ionization and wave-packet dynamics studied using two-color XUV and IR pump-probe spectroscopy*. Physical Review Letters, 103(12):16–19, 2009.

[11] F. Calegari, D. Ayuso, A. Trabattoni, L. Belshaw, S. De Camillis, S. Anumula, F. Frassetto, L. Poletto, A. Palacios, P. Decleva, J. B. Greenwood, F. Martín, and M. Nisoli. *Ultrafast electron dynamics in phenylalanine initiated by attosecond pulses*. Science, 346(6207):336–339, 2014.

[12] M. Drescher, M. Hentschel, R. Kienberger, M. Uiberacker, V. Yakovlev, A. Scrinzi, T. Westerwalbesloh, U. Kleineberg, U. Heinzmann, and F. Krausz. *Time-resolved atomic inner-shell spectroscopy*. Nature, 419(6909):803–807, 2002.

[13] E. Goulielmakis, M. Uiberacker, R. Kienberger, A. Baltuska, V. Yakovlev, A. Scrinzi, T. Westerwalbesloh, U. Kleineberg, U. Heinzmann, M. Drescher, and F. Krausz. *Direct Measurement of Light Waves*. Science, 305(5688):1267–1269, 2004.

[14] A. L. Cavalieri, N. Müller, T. Uphues, V. S. Yakovlev, A. Baltuška, B. Horvath, B. Schmidt, L. Blümel, R. Holzwarth, S. Hendel, M. Drescher, U. Kleineberg, P. M. Echenique, R. Kienberger, F. Krausz, and U. Heinzmann. *Attosecond spectroscopy in condensed matter*. Nature, 449(7165):1029–1032, 2007.

[15] M. Schultze, M. Fiess, N. Karpowicz, J. Gagnon, M. Korbman, M. Hofstetter, S. Neppl, A. L. Cavalieri, Y. Komninos, T. Mercouris, C. A. Nicolaides, R. Pazourek, S. Nagele, J. Feist, J. Burgdörfer, A. M. Azzeer, R. Ernstorfer, R. Kienberger, U. Kleineberg, E. Goulielmakis, F. Krausz, and V. S. Yakovlev. *Delay in photoemission*. Science (New York, N.Y.), 328(5986):1658–1662, 2010.

[16] M. Gisselbrecht, K. Klünder, J. M. Dahlström, T. Fordell, M. Swoboda, D. Guénot, P. Johnsson, J. Caillat, J. Mauritsson, A. Maquet, R. Taïeb, and A. L'Huillier. *Exploring single-photon ionization on the attosecond time scale*. Journal of Physics: Conference Series, 388(PART 3):1–4, 2012.

[17] J. M. Dahlström, A. L'Huillier, and A. Maquet. *Introduction to attosecond delays in photoionization*. Journal of Physics B: Atomic, Molecular and Optical Physics, 45(18):183001, 2012.

[18] E. P. Månsson, D. Guénot, C. L. Arnold, D. Kroon, S. Kasper, J. M. Dahlström, E. Lindroth, A. S. Kheifets, A. L'huillier, S. L. Sorensen, and M. Gisselbrecht. *Double ionization probed on the attosecond timescale*. Nature Physics, 10(3):207–211, 2014.

[19] M. Isinger, R. J. Squibb, D. Busto, S. Zhong, A. Harth, D. Kroon, S. Nandi, C. L. Arnold, M. Miranda, J. M. Dahlström, E. Lindroth, R. Feifel, M. Gisselbrecht, and A. L'Huillier. *Photoionization in the time and frequency domain*. Science, 358(6365):893–896, 2017.

[20] Y. H. Jiang, A. Rudenko, E. Plésiat, L. Foucar, M. Kurka, K. U. Kühnel, T. Ergler, J. F. Pérez-Torres, F. Martín, O. Herrwerth, M. Lezius, M. F. Kling, J. Titze, T. Jahnke, R. Dörner, J. L. Sanz-Vicario, M. Schöffler, J. Van Tilborg, A. Belkacem, K. Ueda, T. J. M. Zouros, S. Düsterer, R. Treusch, C. D. Schröter, R. Moshammer, and J. Ullrich. *Tracing direct and sequential two-photon double ionization of D2 in femtosecond extreme-ultraviolet laser pulses*. Physical Review A, 81(2):021401, 2010.

[21] Y. H. Jiang, A. Rudenko, J. F. Pérez-Torres, O. Herrwerth, L. Foucar, M. Kurka, K. U. Kühnel, M. Toppin, E. Plésiat, F. Morales, F. Martín, M. Lezius, M. F. Kling, T. Jahnke, R. Dörner, J. L. Sanz-Vicario, J. Van Tilborg, A. Belkacem, M. Schulz, K. Ueda, T. J. M. Zouros, S. Düsterer, R. Treusch, C. D. Schröter, R. Moshammer, and J. Ullrich. *Investigating two-photon double ionization of D2 by XUV-pump-XUV-probe experiments*. Physical Review A - Atomic, Molecular, and Optical Physics, 81(5):1–4, 2010.

[22] M. Magrakvelidze, O. Herrwerth, Y. H. Jiang, A. Rudenko, M. Kurka, L. Foucar, K. U. Kühnel, M. Kübel, N. G. Johnson, C. D. Schröter, S. Düsterer, R. Treusch, M. Lezius, I. Ben-Itzhak, R. Moshammer, J. Ullrich, M. F. Kling, and U. Thumm. *Tracing nuclear-wave-packet dynamics in singly and doubly charged states of N2 and O2 with XUV-pump-XUV-probe experiments*. Physical Review A - Atomic, Molecular, and Optical Physics, 86(1):1–11, 2012.

[23] J. Feldhaus, M. Krikunova, M. Meyer, T. Möller, R. Moshammer, A. Rudenko, T. Tschentscher, and J. Ullrich. *AMO science at the FLASH and European XFEL free-electron laser facilities*. Journal of Physics B: Atomic, Molecular and Optical Physics, 46(16), 2013.

[24] C. Bostedt, H. N. Chapman, J. T. Costello, J. R. Crespo López-Urrutia, S. Düsterer, S. W. Epp, J. Feldhaus, A. Föhlisch, M. Meyer, T. Möller, R. Moshammer, M. Richter, K. Sokolowski-Tinten, A. Sorokin, K. Tiedtke, J. Ullrich, and W. Wurth. *Experiments at FLASH*. Nuclear Instruments and Methods in Physics Research, Section A: Accelerators, Spectrometers, Detectors and Associated Equipment, 601(1-2):108–122, 2009.

[25] W. Helml, A. R. Maier, W. Schweinberger, I. Grguraš, P. Radcliffe, G. Doumy, C. Roedig, J. Gagnon, M. Messerschmidt, S. Schorb, C. Bostedt, F. Grüner, L. F. Dimauro, D. Cubaynes, J. D. Bozek, T. Tschentscher, J. T. Costello, M. Meyer, R. Coffee, S. Düsterer, A. L. Cavalieri, and R. Kienberger. *Measuring the temporal structure of few-femtosecond free-electron laser X-ray pulses directly in the time domain*. Nature Photonics, 8(12):950–957, 2014.

[26] P. Rudawski, C. M. Heyl, F. Brizuela, J. Schwenke, A. Persson, E. Mansten, R. Rakowski, L. Rading, F. Campi, B. Kim, P. Johnsson, and A. L'Huillier. *A high-flux high-order harmonic source*. Review of Scientific Instruments, 84(7), 2013.

[27] E. Takahashi, Y. Nabekawa, and K. Midorikawa. *Generation of 10-uJ coherent extreme-ultraviolet light by use of high-order harmonics*. Optics Letters, 27:1920, 2002.

[28] E. Takahashi, Y. Nabekawa, M. Nurhuda, and K. Midorikawa. *Generation of high-energy high-order harmonics by use of a long interaction medium*. Journal of the Optical Society of America B, 20(1):158, 2003.

[29] J. F. Hergott, M. Kovacev, H. Merdji, C. Hubert, Y. Mairesse, E. Jean, P. Breger, P. Agostini, B. Carré, and P. Salières. *Extreme-ultraviolet high-order harmonic pulses in the microjoule range*. Physical Review A - Atomic, Molecular, and Optical Physics, 66(2):4, 2002.

[30] N. A. Papadogiannis, L. A. Nikolopoulos, D. Charalambidis, G. D. Tsakiris, P. Tzallas, and K. Witte. *Two-Photon Ionization of He through a Superposition of Higher Harmonics*. Physical Review Letters, 90(13):4, 2003.

[31] K. Midorikawa, Y. Nabekawa, and A. Suda. *XUV multiphoton processes with intense high-order harmonics*. Progress in Quantum Electronics, 32(2):43 – 88, 2008.

[32] B. Manschwetus, L. Rading, F. Campi, S. Maclot, H. Coudert-Alteirac, J. Lahl, H. Wikmark, P. Rudawski, C. M. Heyl, B. Farkas, T. Mohamed, A. L'Huillier, and P. Johnsson. *Two-photon double ionization of neon using an intense attosecond pulse train*. Physical Review A, 93(6):1–5, 2016.

[33] P. Tzallas, D. Charalambidis, N. A. Papadogiannis, K. Witte, and G. D. Tsakiris. *Direct observation of attosecond light bunching*. Nature, 426(6964):267–271, 2003.

[34] T. Shimizu, T. Okino, K. Furusawa, H. Hasegawa, Y. Nabekawa, K. Yamanouchi, and K. Midorikawa. *Observation and analysis of an interferometric autocorrelation trace of an attosecond pulse train*. Physical Review A - Atomic, Molecular, and Optical Physics, 75(3), 2007.

[35] T. Okino, Y. Furukawa, Y. Nabekawa, S. Miyabe, A. A. Eilanlou, E. J. Takahashi, K. Yamanouchi, and K. Midorikawa. *Direct observation of an attosecond electron wave packet in a nitrogen molecule*. Science Advances, 1(8):1–8, 2015.

[36] P. A. Carpeggiani, P. Tzallas, A. Palacios, D. Gray, F. Martín, and D. Charalambidis. *Disclosing intrinsic molecular dynamics on the 1-fs scale through extreme-ultraviolet pump-probe measurements*. Physical Review A - Atomic, Molecular, and Optical Physics, 89(2):24–26, 2014.

[37] Y. Nabekawa, Y. Furukawa, T. Okino, A. Amani Eilanlou, E. J. Takahashi, K. Yamanouchi, and K. Midorikawa. *Sub-10-fs control of dissociation pathways in the hydrogen molecular ion with a few-pulse attosecond pulse train*. Nature Communications, 7:1–5, 2016.

[38] M. Drescher, M. Hentschel, R. Kienberger, G. Tempea, C. Spielmann, G. A. Reider, P. B. Corkum, and F. Krausz. *X-ray pulses approaching the attosecond frontier*. Science, 291(5510):1923–1927, 2001.

[39] I. J. Sola, E. Mével, L. Elouga, E. Constant, V. Strelkov, L. Poletto, P. Villoresi, E. Benedetti, J.-P. Caumes, S. Stagira, C. Vozzi, G. Sansone, and M. Nisoli. *Controlling attosecond electron dynamics by phase-stabilized polarization gating*. Nature {P}hys., 2:319, 2006.

[40] G. Sansone, E. Benedetti, F. Calegari, C. Vozzi, L. Avaldi, R. Flammini, L. Poletto, P. Villoresi, C. Altucci, R. Velotta, S. Stagira, S. De Silvestri, and M. Nisoli. *Isolated single-cycle attosecond pulses*. Science, 314(5798):443–446, 2006.

[41] Z. Li, G. Brown, D. H. Ko, F. Kong, L. Arissian, and P. B. Corkum. *Perturbative High Harmonic Wave Front Control*. Physical Review Letters, 118(3):033905, 2017.

[42] G. Sansone, L. Poletto, and M. Nisoli. *High-energy attosecond light sources*. Nature Photonics, 5(11):655–663, 2011.

[43] M. Chini, K. Zhao, and Z. Chang. *The generation, characterization and applications of broadband isolated attosecond pulses*. Nature Photonics, 8(3):178–186, 2014.

[44] A. Couairon and A. Mysyrowicz. *Femtosecond filamentation in transparent media*. Physics Reports, 441(2-4):47–189, 2007.

[45] E. J. Takahashi, P. Lan, O. D. Mücke, Y. Nabekawa, and K. Midorikawa. *Attosecond nonlinear optics using gigawatt-scale isolated attosecond pulses*. Nature Communications, 4:2691, 2013.

[46] M. Nisoli, S. De Silvestri, O. Svelto, R. Szipöcs, K. Ferencz, C. Spielmann, S. Sartania, and F. Krausz. *Compression of high-energy laser pulses below 5 fs*. Optics Letters, 22(8):522, 1997.

[47] C. P. Hauri, W. Kornelis, F. W. Helbing, A. Heinrich, A. Couairon, A. Mysyrowicz, J. Biegert, and U. Keller. *Generation of intense, carrier-envelope phase-locked few-cycle laser pulses through filamentation*. Applied Physics B: Lasers and Optics, 79(6):673–677, 2004.

[48] G. Stibenz, N. Zhavoronkov, and G. Steinmeyer. *Self-compression of millijoule pulses to 7.8 fs duration in a white-light filament*. Conference on Lasers and Electro-Optics and 2006 Quantum Electronics and Laser Science Conference, CLEO/QELS 2006, 31(274):274–276, 2006.

[49] C. M. Heyl, C. L. Arnold, A. Couairon, and A. L'Huillier. *Introduction to macroscopic power scaling principles for high-order harmonic generation*. Journal of Physics B: Atomic, Molecular and Optical Physics, 50(1):013001, 2017.

[50] A. Couairon, E. Brambilla, T. Corti, D. Majus, O. de J. Ramírez-Góngora, and M. Kolesik. *Practitioner's guide to laser pulse propagation models and simulation*. The European Physical Journal Special Topics, 199(1):5–76, 2011.

[51] A. Suda, M. Hatayama, K. Nagasaka, and K. Midorikawa. *Generation of sub-10-fs, 5-mJ-optical pulses using a hollow fiber with a pressure gradient*. Applied Physics Letters, 86(11):1–3, 2005.

[52] a. Couairon, M. Franco, A. Mysyrowicz, J. Biegert, and U. Keller. *Pulse self-compression to the single-cycle limit by filamentation in a gas with a pressure gradient*. Optics Letters, 30(19):2657, 2005.

[53] S. Skupin, G. Stibenz, L. Bergé, F. Lederer, T. Sokollik, M. Schnürer, N. Zhavoronkov, and G. Steinmeyer. *Self-compression by femtosecond pulse filamentation: Experiments versus numerical simulations*. Physical Review E - Statistical, Nonlinear, and Soft Matter Physics, 74(5):1–9, 2006.

[54] S. Bohman, A. Suda, M. Kaku, M. Nurhuda, T. Kanai, S. Yamaguchi, and K. Midorikawa. *Generation of 5 fs, 0.5 TW pulses focusable to relativistic intensities at 1 kHz.* Optics express, 16(14):10684–10689, 2008.

[55] O. Varela, A. Zaïr, J. San Román, B. Alonso, I. J. Sola, C. Prieto, and L. Roso. *Above-millijoule super-continuum generation using polarisation dependent filamentation in atoms and molecules.* Optics express, 17(5):3630–3639, 2009.

[56] O. Varela, B. Alonso, I. J. Sola, J. S. Román, A. Zaïr, C. Méndez, and L. Roso. *Self-compression controlled by the chirp of the input pulse*. Optics Letters, 35(21):3649, 2010.

[57] C. L. Arnold, B. Zhou, S. Akturk, S. Chen, A. Couairon, and A. Mysyrowicz. *Pulse compression with planar hollow waveguides: A pathway towards relativistic intensity with table-top lasers*. New Journal of Physics, 12, 2010.

[58] C. F. Dutin, A. Dubrouil, S. Petit, and E. Mével. *Post-compression of high-energy femtosecond pulses using gas ionization*. Optics Letters, 35(2):253–255, 2010.

[59] A. V. Mitrofanov, A. A. Voronin, D. A. Sidorov-Biryukov, A. Pugzlys, E. A. Stepanov, G. Andriukaitis, T. Flöry, S. Ališauskas, A. B. Fedotov, A. Baltuška, and A. M. Zheltikov. *Mid-infrared laser filaments in the atmosphere*. Scientific Reports, 5:2–7, 2015.

[60] G. Point, E. Thouin, A. Mysyrowicz, and A. Houard. *Energy deposition from focused terawatt laser pulses in air undergoing multifilamentation*. Opt. Express, 24(6):6271–6282, 2016.

[61] H. S. Chakraborty, M. B. Gaarde, and A. Couairon. *Single attosecond pulses from high harmonics driven by self-compressed filaments.* Optics letters, 31(24):3662–4, 2006.

[62] M. B. Gaarde and A. Couairon. *Intensity Spikes in Laser Filamentation: Diagnostics and Application*. Physical Review Letters, 103(4):1–4, 2009.

[63] D. S. Steingrube, E. Schulz, T. Binhammer, T. Vockerodt, U. Morgner, and M. Kovacev. *Generation of high-order harmonics with ultra-short pulses from filamentation.* Optics express, 17(18):16177–16182, 2009.

[64] D. S. Steingrube, E. Schulz, T. Binhammer, M. B. Gaarde, A. Couairon, U. Morgner, and M. Kovačev. *High-order harmonic generation directly from a filament*. New Journal of Physics, 13, 2011.

[65] M. Miranda, C. L. Arnold, T. Fordell, F. Silva, B. Alonso, R. Weigand, A. L'Huillier, and H. Crespo. *Characterization of broadband few-cycle laser pulses with the d-scan technique*. Optics Express, 20(17):18732, 2012.

[66] K. C. Kulander and B. W. Shore. *Calculations of multiple-harmonic conversion of 1064-nm radiation in Xe*. Physical Review Letters, 62(5):524–526, 1989.

[67] J. L. Krause, K. J. Schafer, and K. C. Kulander. *Calculation of photoemission from atoms subject to intense laser fields*. Physical Review A, 45(7):4998–5010, 1992.

[68] K. J. Schafer, B. Yang, L. F. Dimauro, and K. C. Kulander. *Above threshold ionization beyond the high harmonic cutoff*. Physical Review Letters, 70(11):1599–1602, 1993.

[69] P. B. Corkum. *Plasma perspective on strong field multiphoton ionization*. Physical Review Letters, 71(13):1994–1997, 1993.

[70] M. Lewenstein, P. Balcou, M. Y. Ivanov, A. L'Huillier, and P. B. Corkum. *Theory of high-harmonic generation by low-frequency laser fields*. Physical Review A, 49(3):2117–2132, 1994.

[71] Y. Mairesse, A. De Bohan, L. J. Frasinski, H. Merdji, L. C. Dinu, P. Monchicourt, P. Breger, M. Kovačev, R. Taïeb, B. Carré, H. G. Muller, P. Agostini, and P. Salières. *Attosecond Synchronization of High-Harmonic Soft X-rays*. Science, 302(5650):1540–1543, 2003.

[72] K. Varjú, Y. Mairesse, B. Carré, M. B. Gaarde, P. Johnsson, S. Kazamias, R. López-Martens, J. Mauritsson, K. J. Schafer, P. Balcou, A. L'Huillier, and P. Salières. *Frequency chirp of harmonic and attosecond pulses*. Journal of Modern Optics, 52(2-3):379–394, 2005.

[73] M. Murakami, J. Mauritsson, and M. B. Gaarde. *Frequency-chirp rates of harmonics driven by a few-cycle pulse*. Physical Review A - Atomic, Molecular, and Optical Physics, 72(2):23413, 2005.

[74] C. Guo, A. Harth, S. Carlström, Y. C. Cheng, S. Mikaelsson, E. Marsell, C. Heyl, M. Miranda, M. Gisselbrecht, M. B. Gaarde, K. J. Schafer, A. Mikkelsen, J. Mauritsson, C. L. Arnold, and A. L'Huillier. *Phase control of attosecond pulses in a train*. Journal of Physics B: Atomic, Molecular and Optical Physics, 51(3), 2018.

[75] C. Guo. *A High Repetition Rate Attosecond Light Source Based on Optical Parametric Amplification*. PhD Thesis, 2018.

[76] C. Heyl. *Scaling and Gating Attosecond Pulse Generation*. PhD Thesis, 2014.

[77] N. Tsatrafyllis, B. Bergues, H. Schröder, L. Veisz, E. Skantzakis, D. Gray, B. Bodi, S. Kuhn, G. D. Tsakiris, D. Charalambidis, and P. Tzallas. *The ion microscope as a tool for quantitative measurements in the extreme ultraviolet*. Scientific Reports, 6(August 2015):21556, 2016.

[78] V. E. Nefedova, M. Albrecht, M. Kozlová, and J. Nejdl. *Development of a high-flux XUV source based on high-order harmonic generation*. Journal of Electron Spectroscopy and Related Phenomena, 220:9–13, 2017.

[79] S. Kühn, M. Dumergue, S. Kahaly, S. Mondal, M. Füle, T. Csizmadia, B. Farkas, B. Major, Z. Várallyay, F. Calegari, M. Devetta, F. Frassetto, E. Månsson, L. Poletto, S. Stagira, C. Vozzi, M. Nisoli, P. Rudawski, S. Maclot, F. Campi, H. Wikmark, C. L. Arnold, C. M. Heyl, P. Johnsson, A. L'Huillier, R. Lopez-Martens, S. Haessler, M. Bocoum, F. Boehle, A. Vernier, G. Iaquaniello, E. Skantzakis, N. Papadakis, C. Kalpouzos, P. Tzallas, F. Lépine, D. Charalambidis, K. Varjú, K. Osvay, and G. Sansone. *The ELI-ALPS facility: The next generation of attosecond sources*. Journal of Physics B: Atomic, Molecular and Optical Physics, 50(13):132002, 2017.

[80] C. M. Heyl, J. Güdde, A. Lhuillier, and U. Höfer. *High-order harmonic generation with J laser pulses at high repetition rates*. Journal of Physics B: Atomic, Molecular and Optical Physics, 45(7):74020–9, 2012.

[81] J. Rothhardt, M. Krebs, S. Hädrich, S. Demmler, J. Limpert, and A. Tünnermann. *Absorption-limited and phase-matched high harmonic generation in the tight focusing regime*. New Journal of Physics, 16, 2014.

[82] U. Even. *"The Even-Lavie valve as a source for high intensity supersonic beam"*. EPJ Techniques and Instrumentation, 2(1):17, 2015.

[83] J. Ullrich, R. Moshammer, A. N. Perumal, and R. Moshammer. *Reports on Progress in Physics Related content Recoil-ion and electron momentum spectroscopy : Recoil-ion and electron momentum spectroscopy :*. Rep. Prog. Phys, 66(9):1463, 2003.

[84] W. C. Wiley and I. H. Mclaren. *TimeofFlight Mass Spectrometer with Improved Resolution*. Rev. Sci. Instrum, 1150, 1955.

[85] A. Knapp, A. Kheifets, I. Bray, T. Weber, A. L. Landers, S. Schössler, T. Jahnke, J. Nickles, S. Kammer, O. Jagutzki, L. P. H. Schmidt, T. Osipov, J. Rösch, J. Rösch, M. H. Prior, H. Schmidt-Böcking, C. L. Cocke, and R. Dörner. *Mechanisms of photo double ionization of helium by 530 eV photons*. Physical Review Letters, 89(3):330041–330044, 2002.

[86] D. Akoury, K. Kreidi, T. Jahnke, T. Weber, A. Staudte, M. Schöffler, N. Neumann, J. Titze, L. P. H. Schmidt, A. Czasch, O. Jagutzki, R. A. Costa Fraga, R. E. Grisenti, R. Díez Muiño, N. A. Cherepkov, S. K. Semenov, P. Ranitovic, C. L. Cocke, T. Osipov, H. Adaniya, J. C. Thompson, M. H. Prior, A. Belkacem, A. L. Landers, H. Schmidt-Böcking, and R. Dörner. *The simplest double slit: Interference and entanglement in double photoionization of H2*. Science, 318(5852):949–952, 2007.

[87] A. A. Sorokin, M. Wellhöfer, S. V. Bobashev, K. Tiedtke, and M. Richter. *X-ray-laser interaction with matter and the role of multiphoton ionization: Free-electron-laser studies on neon and helium*. Physical Review A - Atomic, Molecular, and Optical Physics, 75(5):1–4, 2007.

[88] J. Feist, S. Nagele, R. Pazourek, E. Persson, B. I. Schneider, L. A. Collins, and J. Burgdörfer. *Probing electron correlation via attosecond XUV pulses in the two-photon double ionization of helium*. Physical Review Letters, 103(6):63002, 2009.

[89] V. Lakshminarayanan and A. Fleck. *Zernike polynomials: A guide*. Journal of Modern Optics, 58(7):545–561, 2011.

[90] D. G. Lee, J. J. Park, J. H. Sung, and C. H. Nam. *Wave-front phase measurements of high-order harmonic beams by use of point-diffraction interferometry*. Optics Letters, 28(6):480, 2003.

[91] E. Frumker, G. G. Paulus, H. Niikura, D. M. Villeneuve, and P. B. Corkum. *Frequency-resolved high-harmonic wavefront characterization*. Opt. Lett., 34(19):3026–3028, 2009.

[92] D. R. Austin, T. Witting, C. A. Arrell, F. Frank, A. S. Wyatt, J. P. Marangos, J. W. Tisch, and I. A. Walmsley. *Lateral shearing interferometry of high-harmonic wavefronts*. Optics Letters, 36(10):1746, 2011.

[93] Y. Liu, M. Seaberg, D. Zhu, J. Krzywinski, F. Seiboth, C. Hardin, D. Cocco, A. Aquila, B. Nagler, H. J. Lee, S. Boutet, Y. Feng, Y. Ding, G. Marcus, and A. Sakdinawat. *High-accuracy wavefront sensing for x-ray free electron lasers*. Optica, 5(8):967, 2018.

[94] S. Le Pape, P. Zeitoun, M. Idir, P. Dhez, J. J. Rocca, and M. François. *Electromagnetic-Field Distribution Measurements in the Soft X-Ray Range: Full Characterization of a Soft X-Ray Laser Beam*. Phys. Rev. Lett., 88:183901, 2002.

[95] P. Mercère, P. Zeitoun, M. Idir, S. Le Pape, D. Douillet, X. Levecq, G. Dovillaire, S. Bucourt, K. A. Goldberg, P. P. Naulleau, and S. Rekawa. *Hartmann wave-front measurement at 134 nm with λ_EUV/120 accuracy*. Optics Letters, 28(17):1534, 2003.

[96] W. Southwell. *Wave-front estimation from wave-front slope measurements*. Journal of the Optical Society of America, 70(8):998, 1980.

[97] D. Attwood. *Wave Propagation and Refractive Index At Euv and Soft X-Ray Wavelengths*. In *Soft X-rays and Extreme Ultraviolet Radiation*, number 2, pages 55–97. Cambridge University Press, 1999.

[98] A.-S. Morlens, R. López-Martens, O. Boyko, P. Zeitoun, P. Balcou, K. Varjú, E. Gustafsson, T. Remetter, A. L'Huillier, S. Kazamias, J. Gautier, F. Delmotte, and M.-F. Ravet. *Design and characterization of extreme-ultraviolet broadband mirrors for attosecond science*. Optics Letters, 31(10):1558, 2006.

[99] Y. Ménesguen, S. De Rossi, E. Meltchakov, and F. Delmotte. *Aperiodic multilayer mirrors for efficient broadband reflection in the extreme ultraviolet*. Applied Physics A: Materials Science and Processing, 98(2):305–309, 2010.

[100] L. Poletto, F. Frassetto, F. Calegari, A. Trabattoni, and M. Nisoli. *Micro-focusing of XUV attosecond pulses by grazing-incidence toroidal mirrors*. 2013 Conference on Lasers and Electro-Optics Europe and International Quantum Electronics Conference, CLEO/Europe-IQEC 2013, 21(11):13040–13051, 2013.

[101] J. H. Underwood. *Imaging properties and aberrations of spherical optics and nonspherical optics*. In *Experimental Methods in the Physical Sciences*, volume 31. Academic Press, 1998.

[102] C. Bourassin-Bouchet, M. M. Mang, F. Delmotte, P. Chavel, and S. de Rossi. *How to focus an attosecond pulse*. Optics Express, 21(2):2506, 2013.

[103] A. Suda, H. Mashiko, and K. Midorikawa. *Focusing intense high-order harmonics to a micron spot size*. Springer Series in Chemical Physics, 85:183–198, 2007.

[104] P. Kirkpatrick and A. V. Baez. *Formation of Optical Images by X-Rays*. Journal of the Optical Society of America, 38(9):766, 1948.

[105] O. Hignette, G. Rostaing, P. Cloetens, A. Rommeveaux, W. Ludwig, and A. Freund. *Submicron focusing of hard X-rays with reflecting surfaces at the ESRF*. Techniques, 4499:105–116, 2001.

[106] H. Yumoto, H. Mimura, T. Koyama, S. Matsuyama, K. Tono, T. Togashi, Y. Inubushi, T. Sato, T. Tanaka, T. Kimura, H. Yokoyama, J. Kim, Y. Sano, Y. Hachisu, M. Yabashi, H. Ohashi, H. Ohmori, T. Ishikawa, and K. Yamauchi. *Focusing of X-ray free-electron laser pulses with reflective optics*. Nature Photonics, 7(1):43–47, 2013.

[107] S. Matsuyama, H. Nakamori, T. Goto, T. Kimura, K. P. Khakurel, Y. Kohmura, Y. Sano, M. Yabashi, T. Ishikawa, Y. Nishino, and K. Yamauchi. *Nearly diffraction-limited X-ray focusing with variable-numerical-aperture focusing optical system based on four deformable mirrors*. Scientific Reports, 6(April):4–11, 2016.

[108] F. Frassetto, S. Anumula, F. Calegari, A. Trabattoni, M. Nisoli, and L. Poletto. *Microfocusing beamline for XUV-XUV pump-probe experiments using HH generation*. Proc.SPIE, 9208(iii):92080J, 2014.

[109] H. Wolter. *Spiegelsysteme streifenden Einfalls als abbildende Optiken für Röntgenstrahlen*. Annalen der Physik, 445(1-2):94–114, 1952.

[110] T. J. Gaetz, D. Jerius, R. J. Edgar, L. P. Van Speybroeck, D. A. Schwartz, M. L. Markevitch, S. C. Taylor, and N. S. Schulz. *Orbital verification of the CXO high-resolution mirror assembly alignment and vignetting*. Proc. SPIE, 4012:41–52, 2000.

[111] D. F. Mildner and M. V. Gubarev. *Wolter optics for neutron focusing*. Nuclear Instruments and Methods in Physics Research, Section A: Accelerators, Spectrometers, Detectors and Associated Equipment, 634(1 SUPPL.):7–11, 2011.

[112] B. Khaykovich, M. V. Gubarev, Y. Bagdasarova, B. D. Ramsey, and D. E. Moncton. *From x-ray telescopes to neutron scattering: Using axisymmetric mirrors to focus a neutron*

beam. Nuclear Instruments and Methods in Physics Research, Section A: Accelerators, Spectrometers, Detectors and Associated Equipment, 631(1):98–104, 2011.

[113] G. R. Bennett. *Advanced laser-backlit grazing-incidence x-ray imaging systems for inertial confinement fusion research I Design*. Applied Optics, 40(25):4570, 2001.

[114] R. J. Ellis, J. E. Trebes, D. W. Phillion, J. D. Kilkenny, S. G. Glendinning, J. D. Wiedwald, and R. A. Levesque. *Four-frame gated Wolter x-ray microscope*. Review of Scientific Instruments, 61(10):2759–2761, 1990.

[115] S. Matsuyama, M. Fujii, and K. Yamauchi. *Simulation study of four-mirror alignment of advanced Kirkpatrick-Baez optics*, 2010.

[116] V. N. Mahajan. *Strehl ratio for primary aberrations in terms of their aberration variance*. Journal of the Optical Society of America, 73(6):860, 1983.

[117] M. Fushitani. *Applications of pump-probe spectroscopy*. Annual Reports on the Progress of Chemistry - Section C, 104:272–297, 2008.

[118] T. Okino, K. Yamanouchi, T. Shimizu, R. Ma, Y. Nabekawa, and K. Midorikawa. *Attosecond nonlinear Fourier transformation spectroscopy of CO2 in extreme ultraviolet wavelength region*. The Journal of Chemical Physics, 129(16):161103, 2008.

[119] A. Peralta Conde, J. Kruse, O. Faucher, P. Tzallas, E. P. Benis, and D. Charalambidis. *Realization of time-resolved two-vacuum-ultraviolet-photon ionization*. Physical Review A - Atomic, Molecular, and Optical Physics, 79(6):61405, 2009.

[120] E. Skantzakis, P. Tzallas, J. E. Kruse, C. Kalpouzos, O. Faucher, G. D. Tsakiris, and D. Charalambidis. *Tracking autoionizing-wave-packet dynamics at the 1-fs temporal scale*. Physical Review Letters, 105(4):43902, 2010.

[121] Y. Furukawa, Y. Nabekawa, T. Okino, S. Saugout, K. Yamanouchi, and K. Midorikawa. *Nonlinear Fourier-transform spectroscopy of D2 using high-order harmonic radiation*. Physical Review A, 82(1):013421, 2010.

[122] P. Tzallas, E. Skantzakis, L. A. Nikolopoulos, G. D. Tsakiris, and D. Charalambidis. *Extreme-ultraviolet pump-probe studies of one-femtosecond-scale electron dynamics*. Nature Physics, 7(10):781–784, 2011.

[123] P. Tzallas, E. Skantzakis, and D. Charalambidis. *Direct two-XUV-photon double ionization in xenon*. Journal of Physics B: Atomic, Molecular and Optical Physics, 45(7), 2012.

[124] R. Trebino and D. J. Kane. *Using phase retrieval to measure the intensity and phase of ultrashort pulses: frequency-resolved optical gating*. Journal of the Optical Society of America A, 10(5):1101, 1993.

[125] R. Trebino, K. W. DeLong, D. N. Fittinghoff, J. N. Sweetser, M. A. Krumbügel, B. A. Richman, and D. J. Kane. *Measuring ultrashort laser pulses in the time-frequency domain using frequency-resolved optical gating*. Review of Scientific Instruments, 68(9):3277–3295, 1997.

[126] C. Iaconis and I. A. Walmsley. *Spectral phase interferometry for direct electric-field reconstruction of ultrashort optical pulses*. Optics Letters, 23(10):792–794, 1998.

[127] Y. Kobayashi, T. Sekikawa, Y. Nabekawa, and S. Watanabe. *27-Fs Extreme Ultraviolet Pulse Generation By High-Order Harmonics*. Optics Letters, 23(1):64, 1998.

[128] P. Tzallas, D. Charalambidis, N. A. Papadogiannis, K. Witte, and G. D. Tsakiris. *Second-order autocorrelation measurements of attosecond XUV pulse trains*. Journal of Modern Optics, 52(2-3):321–338, 2005.

[129] Y. Nabekawa, T. Shimizu, T. Okino, K. Furusawa, H. Hasegawa, K. Yamanouchi, and K. Midorikawa. *Conclusive evidence of an attosecond pulse train observed with the mode-resolved autocorrelation technique*. Physical Review Letters, 96(8):3–6, 2006.

[130] T. Sekikawa, T. Katsura, S. Miura, and S. Watanabe. *Measurement of the Intensity-Dependent Atomic Dipole Phase of a High Harmonic by Frequency-Resolved Optical Gating*. Physical Review Letters, 88(19):4, 2002.

[131] P. Heissler, P. Tzallas, J. M. Mikhailova, K. Khrennikov, L. Waldecker, F. Krausz, S. Karsch, D. Charalambidis, and G. D. Tsakiris. *Two-photon above-threshold ionization using extreme-ultraviolet harmonic emission from relativistic laser-plasma interaction*. New Journal of Physics, 14, 2012.

[132] P. M. Paul, E. S. Toma, P. Breger, G. Mullot, F. Augé, P. Balcou, H. G. Muller, and P. Agostini. *Observation of a train of attosecond pulses from high harmonic generation*. Science, 292(5522):1689–1692, 2001.

[133] H. Muller. *Reconstruction of attosecond harmonic beating by interference of two-photon transitions*. Applied Physics B, 74(1):s17–s21, 2002.

[134] J. Itatani, F. Quéré, G. L. Yudin, M. Y. Ivanov, F. Krausz, and P. B. Corkum. *Attosecond Streak Camera*. Physical Review Letters, 88(17):4, 2002.

[135] R. Kienberger, E. Goulielmakis, M. Uiberacker, A. Baltuska, V. Yakovlev, F. Bammer, A. Scrinzi, T. Westerwalbesloh, U. Kleineberg, U. Heinzmann, et al. *Atomic transient recorder*. Nature, 427(6977):817, 2004.

[136] Y. Mairesse. *Frequency resolved optical gating for complete reconstruction of attoscond bursts*. Physical Review A, 71:01140, 2005.

[137] J. Gagnon, E. Goulielmakis, and V. S. Yakovlev. *The accurate FROG characterization of attosecond pulses from streaking measurements*. Applied Physics B: Lasers and Optics, 92(1):25–32, 2008.

[138] J. C. Diels and W. Rudolph. *Ultrashort laser pulse phenomena*, volume 36. Academic Press, 2006.

[139] I. Z. Kozma, P. Baum, U. Schmidhammer, S. Lochbrunner, and E. Riedle. *Compact autocorrelator for the online measurement of tunable 10 femtosecond pulses*. Review of Scientific Instruments, 75(7):2323–2327, 2004.

[140] E. Power, J. Pentland, J. Nees, C. P. Hauri, M. Merano, R. Lopez-martens, and G. Mourou. *Measurement of Ultrabroadband Optical Pulses*. Optics Letters, 31(23):3514–3516, 2006.

[141] J. Mohring, T. Buckup, C. S. Lehmann, and M. Motzkus. *Generation of phase-controlled ultraviolet pulses and characterization by a simple autocorrelator setup*. Journal of the Optical Society of America B-Optical Physics, 26(8):1538–1544, 2009.

[142] E. Goulielmakis, G. Nersisyan, N. A. Papadogiannis, D. Charalambidis, G. D. Tsakiris, and K. Witte. *A dispersionless Michelson interferometer for the characterization of attosecond pulses*. Applied Physics B: Lasers and Optics, 74(3):197–206, 2002.

[143] L. A. A. Nikolopoulos, E. P. Benis, P. Tzallas, D. Charalambidis, K. Witte, and G. D. Tsakiris. *Second order autocorrelation of an XUV attosecond pulse train*. Physical Review Letters, 94(11):1–4, 2005.

[144] Y. Nabekawa, T. Shimizu, Y. Furukawa, E. J. Takahashi, and K. Midorikawa. *Interferometry of attosecond pulse trains in the extreme ultraviolet wavelength region*. Physical Review Letters, 102(21):1–4, 2009.

[145] E. J. Moler, Z. Hussain, R. M. Duarte, and M. R. Howells. *Design and performance of a soft x-ray interferometer for ultra-high resolution fourier transform spectroscopy*. Journal of Electron Spectroscopy and Related Phenomena, 80:309–312, 1996.

[146] F. Sorgenfrei, W. F. Schlotter, T. Beeck, M. Nagasono, S. Gieschen, H. Meyer, A. Föhlisch, M. Beye, and W. Wurth. *The extreme ultraviolet split and femtosecond delay unit at the plane grating monochromator beamline PG2 at FLASH*. Review of Scientific Instruments, 81(4), 2010.

[147] H. Mashiko, A. Suda, and K. Midorikawa. *All-reflective interferometric autocorrelator for the measurement of ultra-short optical pulses*. Applied Physics B: Lasers and Optics, 76(5):525–530, 2003.

[148] O. Faucher, P. Tzallas, E. P. Benis, J. Kruse, A. Peralta Conde, C. Kalpouzos, and D. Charalambidis. *Four-dimensional investigation of the 2nd order volume autocorrelation technique*. Applied Physics B: Lasers and Optics, 97(2):505–510, 2009.

[149] S. Usenko, A. Przystawik, L. Lazzarino, M. Jakob, F. Jacobs, C. Becker, C. Haunhorst, D. Kip, and T. Laarmann. *Split-And-Delay Unit for FEL Interferometry in the XUV Spectral Range*. Applied Sciences, 7(6):544, 2017.

[150] T. Gebert, D. Rompotis, M. Wieland, F. Karimi, A. Azima, and M. Drescher. *Michelson-type all-reflective interferometric autocorrelation in the VUV regime*. New Journal of Physics, 16, 2014.

[151] R. Budriūnas, T. Stanislauskas, J. Adamonis, A. Aleknavičius, G. Veitas, D. Gadonas, S. Balickas, A. Michailovas, and A. Varanavičius. *53 W average power CEP-stabilized OPCPA system delivering 55 TW few cycle pulses at 1 kHz repetition rate*. Optics Express, 25(5):5797, 2017.

Scale-invariant nonlinear optics in gases
Available here

Paper I

Two-photon double ionization of neon using an intense attosecond pulse train
Available here

Paper II

A Versatile Velocity Map Ion-Electron Covariance Imaging Spectrometer for High-Intensity XUV Experiments
Available here

Paper III

Micro-Focusing of Broadband High-Order Harmonic Radiation by a Double Toroidal Mirror
Available here

Paper IV

Single-shot XUV wavefront measurements of high harmonics
manuscript

Paper V

Spatio-temporal coupling of attosecond pulses
manuscript

Paper VI

Design and test of a broadband split-and-delay unit for attosecond XUV-XUV pump-probe experiments
Available here

Paper VII